
# Serviceability behaviour of ultra-high-performance fibre-reinforced concrete composite slabs

By

Sirui Chen

Thesis submitted to The University of Adelaide in fulfilment of the requirements for the degree of Doctor of Philosophy

At

The University of Adelaide

-November 2023-

# Table of Contents

**ABSTRACT**

This thesis presents a comprehensive study of composite slabs comprised of a steel profiled deck and ultra-high-performance fibre-reinforced concrete (UHPFRC). The study begins by examining the local bond properties of composite slabs at the contact surface, investigating the impact of concrete mix designs and profiled deck rib openings on the longitudinal bond behaviour. Subsequently, an experimental study is conducted to analyse the behaviour of simply-supported and continuous composite slabs with varying fibre content, focusing on flexural behaviour, load-slip performance and cracking resistance at both the serviceability and ultimate limit states. These experimental results are then used to validate a new numerical model that allows for changing fibre contents and time-dependent behaviour as well as the partial interaction (PI) behaviour between concrete and steel components (for both internal reinforcements and profiled deck). This numerical model is a displacement-based approach that models the serviceability flexural behaviour of simply-supported composite slabs. Finally, based on the same theory as numerical model, an analytical solution which considers non-linear shrinkage strains is developed to provide a quick and rational solution for predicting the load-deflection behaviour of composite slabs at the serviceability limit state.

In the first chapter, the characteristics of UHPFRC and the significant benefits of its application as part of steel concrete composites are introduced. The current studies that investigate the behaviour of steel concrete composite structures in experimental and numerical studies and approaches used to evaluate the performance of composites are summarised. Learning from these studies, research gaps and significances of these studies covered in this thesis are identified.

The second chapter focuses on the study of local bond properties conducting by a new single-lap test apparatus. This new test apparatus is designed to avoid material pre-failure (such as buckling of profiled deck and concrete crushing) and reduce the friction impact from additional clamping force. Six trial tests are conducted to study the impact of various bonded length and then the shortest one is selected for the following 48 tests to study bond behaviour of steel concrete composites in terms of two different steel decks (dove-tailed and trapezoidal types), varying fibre contents and the presence/absence of coarse aggregate in concrete mixing. This interfacial bond-slip property is important because longitudinal shear transfer dominates the behaviour of composites such as ultimate capacity and flexural stiffness.

The third chapter reports on an experimental investigation aimed at quantifying the benefits of application of UHPFRC to composite slabs with profiled steel decks. Steel concrete composites comprising of steel fibre reinforced concrete (SFRC) and high strength concrete (HSC) have been extensively investigated in the previous studies while the application of UHPFRC as potential substitute because of its high compressive strength and ductility, tensile strain-hardening behaviour and superior post-crack characteristics as one component of composite structures have not been given enough attention. This experimental study focuses on the performance of six simply-supported composite slabs and three continuous composite slabs with fibre content of 0%, 1% and 2%. These tests aims to evaluate the influence of fibre content on the behaviour of composite slabs in terms of deformation, stiffness, crack control and moment redistribution.

Furthermore, a rotational displacement-based numerical model is proposed to evaluate the behaviour of composite slab in serviceability with considering long-term effects. The development of this unified approach is necessary because there are numerous combinations for fibre contents and fibre types in cementitious matrix when designing a composite slab. Therefore, a general and applicable model for predicting behaviour of different composite slab designs is required. This model only requires fundamental material properties obtained from small scale tests instead of full-scale slabs loading test results which provides a financial benefit. With application of PI theory in a tension stiffening analysis to determine relative slip between concrete and steel components (local behaviour) and in a mechanics segmental analysis to determine moment/rotation/strain ($M/\theta/\varepsilon$) properties (global behaviour) for the non-debonded and debonded region, this model predicts crack behaviour, longitudinal slip and flexural performance of profiled slab at the serviceability limit state. This numerical model is validated by comparing with a total of six simply-supported experimental test results with applying their corresponding tested material properties as shown in Chapter 3.

Finally, on the basis of numerical model, in order to allow for realistic nonlinear shrinkage strains and relative slip occurring between concrete and steel decking, a closed-form analytical solution is developed to estimate the load-deflection behaviour of composites slab at the serviceability limit state up until the formation of macro-cracking. In this approach, two loading configurations are considered, a central point load and uniform distributed load (UDL), and their corresponding elemental curvature expressions in segmental analysis are demonstrated separately. To simplify the process, all the material properties are assumed to be linear-elastic while concrete tensile strain-stress relationship is bi-linear. This approach is validated by

comparing with numerical model results. Therefore, this analytical solutions can be used as design guideline for evaluating the load-deflection performance of profiled slabs in serviceability behaviour.

**Declaration**

I certify that this work contains no material which has been accepted for the award of any other degree or diploma in my name, in any university or other tertiary institution and, to the best of my knowledge and belief, contains no material previously published or written by another person, except where due reference has been made in the text. In addition, I certify that no part of this work will, in the future, be used in a submission in my name, for any other degree or diploma in any university or other tertiary institution without the prior approval of the University of Adelaide and where applicable, any partner institution responsible for the joint award of this degree. The author acknowledges that copyright of published works contained within the thesis resides with the copyright holder(s) of those works. I give permission for the digital version of my thesis to be made available on the web, via the University's digital research repository, the Library Search and also through web search engines, unless permission has been granted by the University to restrict access for a period of time. I acknowledge the support I have received for my research through the provision of an Australian Government Research Training Program Scholarship.

Date___14/08/2023_____

**List of Publications/Manuscripts Under Review**

***Journal papers***

Chen, S., Visintin, P. and Oehlers, D. J. (2022) 'Bond between very-high and ultra-high performance fibre reinforced concrete and profiled deck sheeting', Journal of Building Engineering, vol. 52, p. 104426–.

Chen, S., Visintin, P. and Oehlers, D. J. (2023) 'Experimental investigation of the influence of fibre content on the flexural performance of simply supported and continuous steel/UHPC concrete slabs', submitted on *steel composite structures* (under review)

Chen, S., Visintin, P., Sturm, A.B. and Oehlers, D. J. (2023) 'Quantifying the serviceability flexural benefits of using UHPFRC in profiled slabs', submitted on *Structural Concrete* (under review).

**Acknowledgements**

I would like to sincerely express my gratitude to my supervisors, Prof. Phillip Visintin and Emeritus Prof. Deric Oehlers. Their professional guidance helped me successfully complete my PhD studies. Without their patience and encouragement, I might have considered quitting my PhD already. Their passion for academic research also inspired me to bravely tackle various challenges bravely.

I would also like to express my gratitude to Dr. Alexander Bonaparte Sturm. Thanks for his patience and thanks for his constructive suggestions which are invaluable in guiding me through challenging academic problems and he has always been proved right.

I am deeply thankful to lab technicians: Jon Ayoub, Ian Ogier, Michael Teague, Gary Bowman, Brenton Howie and Dale Hodson. Their generous support was crucial to the success of experimental tests.

I wish to acknowledge the Faculty of Engineering, Computer and Mathematical Sciences for their support in granting me a full-fee waive scholarship.

Lastly, my heartfelt acknowledge goes to my parents for their unwavering support both emotionally and financially. I am grateful to them for providing me with this opportunity to study abroad, a decision that has profoundly transformed my entire life. They were the driving force behind my initial decision to pursue a doctoral degree. They never pressured me instead respecting whatever decision I made.

# CHAPTER 1 – Introduction

This thesis outlines a comprehensive study of composite slabs comprised of ultra-high-performance fibre-reinforced concrete (UHPFRC) and a steel profiled deck. It begins by examining the bond behaviour between these components as it is this bond that dominates flexural performance of composites. This is followed by an experimental study, which is then compared with newly proposed simulation results to validate the feasibility of numerical displacement-based method. Finally, the model method is simplified into analytical solutions that can quickly predict the load-deflection behaviour of composite slabs in-service behaviour, enabling the application of analytical approach in real projects designs.

This thesis brings together manuscripts submitted, or published in internationally recognised journals and one chapter that is not in the format of a journal submission which tests the feasibility of creating a closed-form mechanics-based analytical solution. Each chapter's title reflects its main content and follows a specific format: an introduction that explains the main theories and results of each chapter, followed by a fully edited text of each manuscript. While the format of Chapter 5 includes an introduction, literature review, research gaps, methodology, validation and conclusions.

The subsequent section provides background information for this thesis. It introduces the benefits of steel-UHPFRC composites as well as the results and limitations of previous research. On the basis of literature review, four research aims are presented.

## 1.1 Background

Profiled slabs are widely used in multi-floor structures, bridges and infrastructure construction, which consist of concrete and steel profiled deck. The cold-formed profiled sheeting deck exhibit low permeability and can serve as a permanent formwork while also acting as reinforcement to resist tensile force [1-3]. This combination can effectively reduce the self-weight of structures and simplify the construction process, making it an economical construction technique [4].

The flexural performance of steel-concrete composite slabs are significantly influenced by the longitudinal shear bond behaviour, which transmits shear stress between concrete and profiled deck. It has been verified that composite slabs with higher shear bond resistance show better structural performance and construction durability [5]. However, current studies have primarily

focused on changing concrete with varying compressive strengths in composite slab study. While with fibres added to the concrete mix, steel concrete composite structures show more complex characteristics in terms of concrete material properties and composite bond connection behaviour. Therefore, these studies shows limitations in design of steel concrete composite comprising of concrete with fibre.

In order to enhance member performance of profiled slabs, there is interest in introducing a new concrete technology, ultra-high-performance fibre-reinforced concrete (UHPFRC), into steel concrete composite construction. UHPFRC is a novel cementitious material that has gained popularity in recent decades. It possesses high compressive strength and ductility and particularly in terms of tensile properties, shows superior strain-hardening behaviour and ductile post-cracking performance. By increasing flexural strength, toughness and durability [6], UHPFRC enables longer spans, extended service life and reduced maintenance making it a sustainable construction material.

In UHPFRC slabs studies, the benefits of UHPFRC can be summarised as follows: it increases member stiffness, reduces member deflection and reduces crack widths, that mitigating the formation of large cracks [7-9]. Furthermore, UHPFRC improves performance in the hogging region of continuous slabs, it shows significant rotational capacity because of fibre stress transfer between concrete, enabling higher moment redistribution [10].

Time-dependent behaviour of profiled slabs is also worth noting due to the application of impervious steel decks, which prevent water egress while the top of composite slab is exposed to ambient environment leading to the non-uniform strain distribution. This time-dependent effect makes concrete is more prone to cracking which will reduce the service life of structure. Therefore, the non-uniform shrinkage strain should be taken into consideration in real structural design [11, 12].

### 1.2 Literature review

This section summarises the existing investigations including those on composite slabs longitudinal bond behaviour, full-scale profiled slabs tests as well as analytical techniques for composites performance in serviceability limit state.

### *1.2.1 Longitudinal bond property*

The significance of studying bond properties for steel concrete composite structures comprising of profiled deck and reinforced concrete is that the longitudinal shear behaviour of composite slab is heavily dependent on the partial interaction between concrete and internal reinforcement as well as that between reinforced concrete and the profiled sheet, which can make an impact on overall member performance of composites [5, 13]. Therefore, it is necessary to quantify the interface shear behaviour and identify parameters that can affect the bond stress. The current approaches which used to study bond behaviour between concrete and profiled sheet can be categorised into small-component tests and beam-scale tests.

Small-component tests include Daniel's test [14], push-out test [15, 16], push-off test [17-19], pull-out test [20, 21] and slip-block test [22-28] which can measure longitudinal shear stress directly. The procedures of these tests generally involve pulling profiled deck or pushing the concrete component along the longitudinal direction and recording the relationship between relative slip at contact surface and shear resistance. However, these elemental tests have certain drawbacks including pre-delamination at contact surface, concrete crushing, buckling at bottom of profiled deck and the additional lateral force required to maintain rotational equilibrium which can also introduce additional friction which can affect the accuracy of measured results. Furthermore, in pull-out tests with excessively long bonded length, shear stress will be varied and cannot be constant along the bonded section [26].

For beam-scale approaches, the *m-k* method and partial shear connection (PSC) method are commonly used [2, 29-33]. Both methods rely on conducting four-point bending tests while varying the geometry of the composite slab (including steel deck thickness, composites total depth and shear span). These tests allow for the estimation of not only longitudinal shear capacity but also flexural capacity. However, these member-level tests also have limitations in that it is required that at least six full-scale tests results are used to predict shear strength numerically and this can increase tests budget and time cost.

### *1.2.2 Composite slab full-scale test*

#### *1.2.2.1 Simply-supported tests*

In simply-supported slab tests, the application of steel fibre reinforced concrete (SFRC) can reduce slip between the contact surface and increase flexural strength [5]. For hogging regions, fibre can provide sufficient crack control. In general, the presence of fibres enhances

longitudinal bond strength, ultimate capacity and reduces crack width. Besides, one study mentions that replacing a proportion of steel reinforced bars with steel fibres can still achieve the required capacity and also simplify the construction processes. Moreover, as the fibre content increases, the rotational capacity and ultimate load can also increase [27, 34, 35].

#### *1.2.2.2 Continuous slab tests*

In terms of serviceability behaviour, continuous steel profiled slab tests are conducted to investigate the impact of shrinkage. The presence of fibres reduces deflections and crack widths because of its ability to restrain shrinkage [36]. In addition, it can improve the rotation capacity, ductility and increase moment redistribution [37]. Besides, it can enhance the flexural performance of composites even after concrete cracking [38, 39].

#### *1.2.2.3 Other UHPFRC composite structures*

In the above section, the current studies on composite slabs are limited to the utilisation of SFRC and high strength concrete (HSC) with profiled deck, even though UHPFRC is a highly promising substitute for improving the working effectiveness and construction ability of composite structures. Currently, there are studies focusing on the advantages of applying UHPFRC with steel components (such as orthotropic steel decks [40], corrugated steel decks [41], steel plates [42-45] and I-shaped steel beams [46-50]) compared to normal strength concrete counterpart.

The conclusions drawn from these studies are that steel concrete composites with UHPFRC show higher tensile strength result in and increased cracking load, enhanced ultimate load capacity and flexural rigidity and reducing deflections [42, 44-48]. Besides, the inclusion of fibres proves beneficial in restricting the expansion of crack openings. Specifically, the fibre bridging effect can inhibit crack propagation, thereby providing better crack resistance. In the serviceability limit state, the addition of fibres in concrete can reduce concrete shrinkage strain [49]. While at the ultimate limit state, the application of UHPFRC in steel concrete composite structures can lead to significant moment redistribution because of its superior compressive and tensile material properties. Consequently, composite slabs are considered to reduce depth of composites and require fewer reinforcement bars while still meeting the load requirements.

### *1.2.3 Analytical procedures*

Current analytical studies for composite slabs only considering normal strength concrete. These analytical solutions have been validated by comparing with experimental results. One method is to consider both the uncracked and cracked condition to estimate an effective moment of inertia for composite structures [51]. Another approach considers non-uniform shrinkage strain because time-dependent effects are a vital factor on composites long-term flexural performance [52]. Developed from previous mentioned methods which assume full-interaction between contact surfaces, there are studies show a more rigorous approach which consider partial interaction at interfacial surface that means relative slip occurs between concrete and profiled deck with assuming the shear connection stiffness between concrete and profiled deck is linear along the whole process [53, 54].

## 1.3 Research gaps

***Gap 1:***

In previous studies, all the small-scale tests utilised a long bonded length, as a result the average experimental shear stress results may be inaccurate due to a significant slip variation along the bonded section while maintaining a constant slip value along the bonded section will be an ideal condition.

Another limitation is the numerous combinations involving varied fibre contents and different fibre types in concrete mixing. This requires an effective approach to quantify the bond performance. Additionally, it is widely known that the inclusion of coarse aggregate is beneficial in both environmental and economic aspects. However, when cementitious matrix contains coarse aggregates and fibres, it will make an impact on material mechanical properties [55-58] and even longitudinal performance of composite slab, which increases the complexity of bond behaviour study. Therefore, a generic composite slab boned behaviour test apparatus should be proposed to eliminate the aforementioned shortcomings.

***Gap 2:***

Even though there are investigations utilising UHPFRC into steel-concrete composite structures, no research is aimed at studying UHPFRC in cooperation with profiled steel deck while experimental study is the basis for composites structural design. In addition, it is known that adding more fibres in concrete mixing can increase the stiffness and capacity of composite

slab while determination of the most suitable fibre content which can achieve both slab capacity and meets economic requirements needs future investigation. Moreover, continuous slabs which comprised of two or more spans should also studied for learning about moment redistribution for composite structure in-service performance evaluation.

***Gap 3:***

Firstly, there are numerous fibre contents and fibre types can be applied into cementitious matrix leading to various material properties. It is desirable to develop a unified approach that can be applicable and feasible for profiled slabs with different and complex material properties (concrete tensile strain-stress and crack width-stress relationship, profiled deck strain-stress relationship as well as longitudinal bond stress). With considering time-dependent shrinkage strain, serviceability behaviour of composite slab can be predicted, making this approach as a design guideline.

***Gap 4:***

Current analytical solutions are only applicable to composite slabs consisting of normal strength concrete. It is also not uncommon to ignore the contribution of concrete in tension when performing analysis [51]. However, for UHPFRC, the exceptional tensile performance cannot be disregarded in structural design.

Another assumption made in analysis is to assume a fixed flexural rigidity ($EI$) in composite slab analysis which is inaccurate because this fixed stiffness assumes zero axial force applied to composites along the whole slabs, while the realistic condition is that bond forces keep accumulating along the slab between UHPFRC and profiled deck resulting in an increasing axial force should be applied to both concrete and profiled deck in each elemental analysis. Overall, there is no study that consider both time-dependent effect and shear connection between contact surface to design composite slabs using UHPFRC for serviceability behaviours including flexural performance, load-slip and cracking behaviours.

## 1.4 Research aims

***Aim 1***

A new small scale test apparatus (rapid, low-cost) will be proposed to investigate shear transfer mechanisms for UHPFRC with varying fibre contents and coarse aggregate contents cooperating with different types of profiled deck. This test apparatus is developed from previous small scale tests and it addresses the pre-mentioned limitations. This study will begin by examining the bonded length and subsequently study the impact of fibres and coarse aggregate and profiled deck types on longitudinal bond performance.

***Aim 2***

The further investigation is about flexural and crack performance of composite slabs with different fibre contents. An experimental study will be conducted on composites subjected to sagging and hogging moment with 0%, 1 % and 2% fibre content. These studies will focus on how varying fibre dosages make an influence on improvement of flexural performance, slip-bond performance and crack resistance as well as post-peak performance of composites. For continuous slabs, three replicate two-span slabs with different fibre dosages will be used to study moment redistribution which can quantify serviceability of composites slabs.

***Aim 3***

A generic approach will be proposed to simulate the behaviour of composite slabs at the serviceability limit state in order to develop profiled slab design approaches. This approach will incorporate the longitudinal local bond property obtained from aim one, and then evaluate the feasibility of this numerical method by comparing simulated results with experimental results from aim two. This numerical analysis aims to comprehensively study profiled slab under simply-supported conditions. It will be used to determine flexural deflection, load-slip behaviour and crack localisation as well as crack width with considering shrinkage strain for serviceability design.

***Aim 4***

Analytical solutions to quickly estimate composite slabs load-deflection behaviour for structural design will be proposed. It will align the same methodology with aim three incorporating with reasonable assumptions. This analytical solutions will allow for UHPFRC

uncracking and strain-hardening behaviour, the partial interaction behaviour between concrete and steel components (reinforced bars and steel deck sheeting) and non-linear shrinkage strain in order to form a rigorous approach for composite slabs in-service design [52].

## Reference


[1] X. Li, X. Zheng, M. Ashraf, and H. Li, "Experimental study on the longitudinal shear bond behavior of lightweight aggregate concrete – Closed profiled steel sheeting composite slabs," *Construction and Building Materials,* vol. 156, pp. 599-610, 2017, doi: 10.1016/j.conbuildmat.2017.08.108.

[2] M. Pereira and R. Simões, "Contribution of steel sheeting to the vertical shear capacity of composite slabs," *Journal of Constructional Steel Research,* vol. 161, pp. 275-284, 2019.

[3] Y. Zhu, Y. Zhang, H. H. Hussein, and G. Chen, "Numerical modeling for damaged reinforced concrete slab strengthened by ultra-high performance concrete (UHPC) layer," *Engineering Structures,* vol. 209, p. 110031, 2020/04/15/ 2020, doi: https://doi.org/10.1016/j.engstruct.2019.110031.

[4] X. Li, X. Zheng, M. Ashraf, and H. Li, "The longitudinal shear bond behavior of an innovative laminated fiber reinforced composite slab," *Construction and Building Materials,* vol. 215, pp. 508-522, 2019.

[5] K. M. A. Hossain, S. Alam, M. S. Anwar, and K. M. Y. Julkarnine, "High performance composite slabs with profiled steel deck and Engineered Cementitious Composite – Strength and shear bond characteristics," *Construction & building materials,* vol. 125, pp. 227-240, 2016, doi: 10.1016/j.conbuildmat.2016.08.021.

[6] J. Li, Z. Wu, C. Shi, Q. Yuan, and Z. Zhang, "Durability of ultra-high performance concrete – A review," *Construction & building materials,* vol. 255, p. 119296, 2020, doi: 10.1016/j.conbuildmat.2020.119296.

[7] A. Hassan, S. Jones, and G. Mahmud, "Experimental test methods to determine the uniaxial tensile and compressive behaviour of ultra high performance fibre reinforced concrete (UHPFRC)," *Construction and building materials,* vol. 37, pp. 874-882, 2012.

[8] L. Hussein and L. Amleh, "Structural behavior of ultra-high performance fiber reinforced concrete-normal strength concrete or high strength concrete composite members," *Construction and Building Materials,* vol. 93, pp. 1105-1116, 2015.

[9] A. B. Sturm, P. Visintin, and D. J. Oehlers, "Blending fibres to enhance the flexural properties of UHPFRC beams," *Construction and Building Materials,* vol. 244, p. 118328, 2020.

[10] P. Visintin, M. S. Mohamad Ali, T. Xie, and A. B. Sturm, "Experimental investigation of moment redistribution in ultra-high performance fibre reinforced concrete beams,"

*Construction and Building Materials*, vol. 166, pp. 433-444, 2018/03/30/ 2018, doi: https://doi.org/10.1016/j.conbuildmat.2018.01.156.

[11] S. Al-deen and G. Ranzi, "Effects of non-uniform shrinkage on the long-term behaviour of composite steel-concrete slabs," *International journal of steel structures*, vol. 15, no. 2, pp. 415-432, 2015.

[12] R. I. Gilbert, M. A. Bradford, A. Gholamhoseini, and Z. T. Chang, "Effects of shrinkage on the long-term stresses and deformations of composite concrete slabs," *Engineering Structures*, vol. 40, pp. 9-19, 2012, doi: 10.1016/j.engstruct.2012.02.016.

[13] A. B. Sturm and P. Visintin, "Local bond slip behavior of steel reinforcing bars embedded in ultra high performance fibre reinforced concrete," *Structural Concrete*, vol. 20, no. 1, pp. 108-122, 2018, doi: https://doi.org/10.1002/suco.201700149.

[14] B. Daniels and M. Crisinel, "Ccomposite slab behavior and strength analysis .1. calculation procedure," *Journal Of Structural Engineering-Asce*, vol. 119, no. 1, pp. 16-35, 1993, doi: 10.1061/(ASCE)0733-9445(1993)119:1(16).

[15] C. K. Jolly and A. Zubair, "The efficiency of shear-bond interlock between profiled steel sheeting and concrete," *Composite Steel Structures. Advances, Design, And Construction*, pp. 127-136, 1987.

[16] M. Porter and C. Ekberg Jr, "Investigation of cold-formed steel-deck-reinforced concrete floor slabs," 1971.

[17] M. J. Burnet and D. J. Oehlers, "Rib shear connectors in composite profiled slabs," *Journal of Constructional Steel Research*, vol. 57, no. 12, pp. 1267-1287, 2001.

[18] J. W. Stark, "Design of composite floors with profiled steel sheet," 1978.

[19] M. M. Rana, B. Uy, and O. Mirza, "Experimental and numerical study of the bond–slip relationship for post-tensioned composite slabs," *Journal of Constructional Steel Research*, vol. 114, pp. 362-379, 2015.

[20] R. Tremlay, P. Gignac, G. Degrange, and C. A. Rogers, "Variables affecting the shear-bond resistance of composite floor deck systems," 2002.

[21] E. Airumyan, V. Belyaev, and I. Rumyancev, "Efficient embossment for corrugated steel sheeting," in *IABSE Symposium on Mixed Structures Including New Materials*, 1990, pp. 137-142.

[22] P. Mäkeläinen and Y. Sun, "The longitudinal shear behaviour of a new steel sheeting profile for composite floor slabs," *Journal of Constructional Steel Research*, vol. 49, no. 2, pp. 117-128, 1999, doi: 10.1016/S0143-974X(98)00211-9.

[23] J. Holomek, M. Bajera, and M. Vilda, "Test Arrangement of Small-scale Shear Tests of Composite Slabs," *Procedia Engineering*, vol. 161, no. C, pp. 716-721, 2016, doi: 10.1016/j.proeng.2016.08.749.

[24] J. Holomek, M. Bajer, J. Barnat, and P. Schmid, "Design of composite slabs with prepressed embossments using small-scale tests," *Structural Concrete*, vol. 16, no. 1, pp. 137-148, 2015.

[25] M. Patrick and K. Poh, "Controlled test for composite slab design parameters," in *IABSE Symposium, Brussels, Belgium-Mixed Structures, Including New Materials*, 1990, pp. 227-231.

[26] O. Yi, Y. Zhuge, X. Ma, R. J. Gravina, J. E. Mills, and O. Youssf, "Push-off and pull-out bond behaviour of CRC composite slabs–an experimental investigation," *Engineering Structures*, vol. 228, p. 111480, 2021.

[27] M. Petkevičius and J. Valivonis, "Analysis of bending capacity of composite steel-concrete slabs with steel fiber reinforced concrete," 2010.

[28] J. Holomek, M. Bajer, J. Barnat, and M. Vild, "Composite Slabs with Prepressed Embossments – Longitudinal Shear Resistance," Applied Mechanics and Materials, vol. 769, pp. 289-293, 06/01 2015, doi: https://doi.org/10.4028/www.scientific.net/AMM.769.289

[29] R. P. Johnson and D. Anderson, "EN1994 Eurocode 4: Design of composite steel and concrete structures," *Proceedings of the Institution of Civil Engineers - Civil Engineering*, vol. 144, no. 6, pp. 33-38, 2001, doi: 10.1680/cien.2001.144.6.33.

[30] L. An and K. Cederwall, "Composite slabs analyzed by block bending test," 1992.

[31] V. Marimuthu, S. Seetharaman, S. A. Jayachandran, A. Chellappan, T. Bandyopadhyay, and D. Dutta, "Experimental studies on composite deck slabs to determine the shear-bond characteristic (m–k) values of the embossed profiled sheet," *Journal of Constructional Steel Research*, vol. 63, no. 6, pp. 791-803, 2007.

[32] K. Lambe and S. Siddh, "Analysis and design of composite slab by varying different parameters," *IOP Conference Series: Materials Science and Engineering*, vol. 330, p. 012115, 2018/03 2018, doi: 10.1088/1757-899x/330/1/012115.

[33] B. S. Mohammed, "Structural behavior and m– k value of composite slab utilizing concrete containing crumb rubber," *Construction & building materials*, vol. 24, no. 7, pp. 1214-1221, 2010, doi: 10.1016/j.conbuildmat.2009.12.018.

[34] A. Gholamhoseini, A. Khanlou, G. MacRae, S. Hicks, A. Scott, and C. Clifton, "Short-term behaviour of reinforced and steel fibre–reinforced concrete composite slabs with steel decking under negative bending moment," *Advances in Structural Engineering*, vol. 21, no. 9, pp. 1288-1301, 2018.

[35] F. Abas, M. A. Bradford, S. J. Foster, and R. Ian Gilbert, "Shear-Bond Behaviour of Steel-Fibre Reinforced Concrete (SFRC) Composite Slabs with Deep Trapezoidal Decking: Experimental Study," in *Composite Construction in Steel and Concrete VII*, 2016, pp. 561-580.

[36] A. Gholamhoseini, A. Khanlou, G. MacRae, A. Scott, S. Hicks, and R. Leon, "An experimental study on strength and serviceability of reinforced and steel fibre reinforced concrete (SFRC) continuous composite slabs," *Engineering Structures*, vol. 114, pp. 171-180, 2016/05/01/ 2016, doi: https://doi.org/10.1016/j.engstruct.2016.02.010.

[37] F. P. Ackermann and J. Schnell, "Steel Fibre Reinforced Continuous Composite Slabs," in *Composite Construction in Steel and Concrete VI*, 2011, pp. 125-137.

[38] F. Abas, R. Gilbert, S. Foster, and M. Bradford, "Strength and serviceability of continuous composite slabs with deep trapezoidal steel decking and steel fibre reinforced concrete," *Engineering structures*, vol. 49, pp. 866-875, 2013.

[39] A. Gholamhoseini, "Experimental and finite element study of ultimate strength of continuous composite concrete slabs with steel decking," *International Journal of Advanced Structural Engineering*, vol. 10, pp. 85-97, 03/01 2018, doi: 10.1007/s40091-018-0183-3.

[40] Z. He and P. Lin, "Research on fatigue performance and optimal design of steel-UHPC composite slab," in *Structures*, 2022, vol. 43: Elsevier, pp. 682-695.

[41] Z. Cheng, Q. Zhang, Y. Bao, P. Deng, C. Wei, and M. Li, "Flexural behavior of corrugated steel-UHPC composite bridge decks," *Engineering Structures*, vol. 246, p. 113066, 2021/11/01/ 2021, doi: https://doi.org/10.1016/j.engstruct.2021.113066.

[42] J.-L. Xiao, M. Zhou, J.-G. Nie, T.-Y. Yang, and J.-S. Fan, "Flexural behavior of steel-UHPC composite slabs with perfobond rib shear connectors," *Engineering Structures*, vol. 245, p. 112912, 2021.

[43] J.-Y. Guo, J.-Y. Wang, Y.-B. Wang, X.-L. Gao, and C. Bian, "Experimental study on demountable steel ultra-high performance concrete composite slabs under hogging moment," *Archives of Civil and Mechanical Engineering*, vol. 22, no. 3, p. 137, 2022.

[44] J.-Y. Guo, J.-Y. Wang, Y.-B. Wang, X.-L. Gao, and C. Bian, "Experimental study on demountable steel ultra-high performance concrete composite slabs under hogging moment," *Archives of Civil and Mechanical Engineering*, vol. 22, no. 3, pp. 1-24, 2022.

[45] Z. Wang, J. Yan, Y. Lin, F. Fan, and Y. Yang, "Mechanical properties of steel-UHPC-steel slabs under concentrated loads considering composite action," *Engineering Structures*, vol. 222, p. 111095, 2020.

[46] P. Zhang *et al.*, "Experimental study of a novel continuous FRP-UHPC hybrid beam," *Composite Structures*, vol. 261, p. 113329, 2021.

[47] J. Qi, Z. Cheng, J. Wang, and Y. Tang, "Flexural behavior of steel-UHPFRC composite beams under negative moment," in *Structures*, 2020, vol. 24: Elsevier, pp. 640-649.

[48] Y. Zhang, S. Cai, Y. Zhu, L. Fan, and X. Shao, "Flexural responses of steel-UHPC composite beams under hogging moment," *Engineering Structures*, vol. 206, p. 110134, 2020/03/01/ 2020, doi: https://doi.org/10.1016/j.engstruct.2019.110134.

[49] X. Liu, J. Zhang, Z. Cheng, and M. Ye, "Experimental and Numerical Studies on the Negative Flexural Behavior of Steel-UHPC Composite Beams," *Advances in Civil Engineering*, vol. 2021, pp. 1-15, 01/31 2021, doi: 10.1155/2021/8828175.

[50] L. Tong, L. Chen, X. Wang, J. Zhu, X. Shao, and Z. Zhao, "Experiment and finite element analysis of bending behavior of high strength steel-UHPC composite beams," *Engineering Structures,* vol. 266, p. 114594, 2022.

[51] R. S. Costa, A. C. C. Lavall, R. G. L. da Silva, H. F. Viana, F. C. Rodrigues, and E. L. Andrade, "New equations to establish the effective moment of inertia of composite slabs with profiled steel sheeting for deflection calculation," *Journal of Building Engineering,* vol. 37, p. 102135, 2021.

[52] Q. Wang, J. Yang, Y. Zhang, Y. Fang, and Q. Ren, "Analysis and design of long-term responses of simply-supported steel–concrete composite slabs," *Journal of Building Engineering,* vol. 53, p. 104496, 2022.

[53] M. A. Bradford, "Generic modelling of composite steel–concrete slabs subjected to shrinkage, creep and thermal strains including partial interaction," *Engineering structures,* vol. 32, no. 5, pp. 1459-1465, 2010, doi: 10.1016/j.engstruct.2010.01.024.

[54] P. Vainiūnas, J. Valivonis, G. Marčiukaitis, and B. Jonaitis, "Analysis of longitudinal shear behaviour for composite steel and concrete slabs," *Journal of Constructional Steel Research,* vol. 62, no. 12, pp. 1264-1269, 2006.

[55] J. Yu, B. Zhang, W. Chen, and J. He, "Experimental and multi-scale numerical investigation of ultra-high performance fiber reinforced concrete (UHPFRC) with different coarse aggregate content and fiber volume fraction," *Construction and Building Materials,* vol. 260, p. 120444, 2020.

[56] F. Wu, L. Xu, Y. Chi, Y. Zeng, F. Deng, and Q. Chen, "Compressive and flexural properties of ultra-high performance fiber-reinforced cementitious composite: The effect of coarse aggregate," *Composite Structures,* vol. 236, p. 111810, 2020/03/15/ 2020, doi: https://doi.org/10.1016/j.compstruct.2019.111810.

[57] L. Xu, F. Wu, Y. Chi, P. Cheng, Y. Zeng, and Q. Chen, "Effects of coarse aggregate and steel fibre contents on mechanical properties of high performance concrete," *Construction and Building Materials,* vol. 206, pp. 97-110, 2019.

[58] P. P. Li, Y. Y. Y. Cao, M. J. C. Sluijsmans, H. J. H. Brouwers, and Q. Yu, "Synergistic effect of steel fibres and coarse aggregates on impact properties of ultra-high performance fibre reinforced concrete," *Cement and Concrete Composites,* vol. 115, p. 103866, 01/01 2021, doi: 10.1016/j.cemconcomp.2020.103866.

## CHAPTER 2– Member Level Tests

### Introduction

In this chapter, the bond behaviour of composite slabs is studied by using a newly proposed elemental test apparatus. These local bond properties are quantified and will be applied in Chapter 4 - Numerical analysis.

The publication titled “Bond between very-high and ultra-high performance fibre reinforced concrete and profiled deck sheeting” presents an experimental study on the interfacial shear properties between UHPFRC and two different types of decks (dove-tailed and trapezoid). A new apparatus for single-lap shear tests is introduced, which is developed from companion papers with eliminating pre-failure phenomenon and additional constraints. These experimental tests consist of six trial tests to study the reasonable bonded length, followed by 48 tests to quantify the bond behaviour, where this study objectives include concrete strength, fibre and coarse aggregate content as well as the types of profiled steel sheeting. The impacts of fibre and coarse aggregate are studied by utilising eight concrete mixing designs that concrete compressive strength varies from 100 MPa to 126 MPa both with and without fibre.

**Statement of Authorship**

# Statement of Authorship

| | |
|---|---|
| Title of Paper | Bond between very-high and ultra-high performance fibre reinforced concrete and profiled deck sheeting |
| Publication Status | ☑ Published ☐ Accepted for Publication<br>☐ Submitted for Publication ☐ Unpublished and Unsubmitted work written in manuscript style |
| Publication Details | Chen, S., Visintin, P. and Oehlers, D. J. (2022) 'Bond between very-high and ultra-high performance fibre reinforced concrete and profiled deck sheeting', Journal of Building Engineering, vol. 52, p. 104426–. |

## Principal Author

| | | | |
|---|---|---|---|
| Name of Principal Author (Candidate) | Sirui Chen | | |
| Contribution to the Paper | Investigation, data processing, writing - original draft | | |
| Overall percentage (%) | 90% | | |
| Certification: | This paper reports on original research I conducted during the period of my Higher Degree by Research candidature and is not subject to any obligations or contractual agreements with a third party that would constrain its inclusion in this thesis. I am the primary author of this paper. | | |
| Signature | | Date | 14/08/2023 |

## Co-Author Contributions

By signing the Statement of Authorship, each author certifies that:

i. the candidate's stated contribution to the publication is accurate (as detailed above);
ii. permission is granted for the candidate in include the publication in the thesis; and
iii. the sum of all co-author contributions is equal to 100% less the candidate's stated contribution.

| | | | |
|---|---|---|---|
| Name of Co-Author | Phillip Visintin | | |
| Contribution to the Paper | Conceptualization, methodology, supervision, writing -review | | |
| Signature | | Date | 14/08/2023 |

| | | | |
|---|---|---|---|
| Name of Co-Author | Deric John Oehlers | | |
| Contribution to the Paper | Conceptualization, supervision, writing -review | | |
| Signature | | Date | 14/08/2023 |

Please cut and paste additional co-author panels here as required.

**Bond between very-high and ultra-high performance fibre reinforced concrete and profiled deck sheeting**

Chen, S., Visintin, P., Oehlers, D.J.

**Abstract**

The behaviour of steel concrete composite slabs at all load levels is controlled by the shear transfer between the profiled steel deck and concrete slab. To apply new concrete technologies, such as high-strength and fibre-reinforced concretes, to steel concrete composite slabs, it is therefore essential to quantify the interfacial bond-slip properties. In this paper, a testing approach based on single-lap shear tests, commonly applied to quantify interfacial shear properties for external reinforcement, is applied to measure the bond between profiled sheets and concrete. The testing regime consists of 6 trial tests used as the basis for developing the test methodology and 48 tests to quantify the impact of concrete strength (very-high and ultra-high-strength), high volumes of steel micro fibres, and coarse aggregate, on the bond between concrete and dovetailed and trapezoidal profile decks. The results show that the concrete strength and the presence of coarse aggregate have limited impact on the bond properties, however the presence of fibres significantly improves bond strength and toughness for dovetailed profiled decks but has limited influence on trapezoidal decks.

**Keywords**

Composite slab, bond property, UHPFRC, small-scale tests, longitudinal shear

## 1. Introduction

Steel concrete composite floor systems are commonly applied because of their potential to achieve highly efficient cross sections, simplify the construction process and increase the speed of construction [1-6]. Recent advancements in concrete technology have led to the development of very-high and ultra-high performance fibre reinforced concretes (UHPFRC) that are generally characterised by compressive strengths above 100 MPa, high ultimate strains and post-crushing residual strengths, non-negligible post-cracking tensile strength and very-high durability [7-10].

Although high strength is generally not essential in the design of composite slabs, the application of UHPFRC has a number of potential advantages:

(i) The significant post-cracking tensile behaviour of UHPFRC has been shown in experimental research on both steel concrete composite and reinforced concrete beams to significantly improve serviceability behaviour by reducing member deflections and crack widths [11, 12].

(ii) In experimental research on composite slabs with profiled deck, the presence of any volume of fibres has been shown to improve the performance of hogging regions by limiting crack widths. Therefore, if fibres can provide sufficient post cracking tensile strength, there is the potential that fibre reinforcement can replace a proportion of conventional reinforcement in hogging regions, thereby simplifying construction [13, 14].

(iii) The high material ductility under compression enables plastic hinge regions to undergo significant rotation, thereby allowing for substantial moment redistribution. This is advantageous because it enables more economical design and the simplification of detailing requirements for slabs which are continuous over supports [1, 13, 15-18].

(iv) The high material durability of UHPFRC also presents the potential to significantly extend the life-span and reduce the maintenance of structures leading to environmental and financial benefits [8, 19].

Previous research on the application of UHPFRC to steel concrete composites has focused on composite beams, and in particular the application to hogging regions of continuous beams [11, 12, 20]. For example, Qi et al. [11] compared the flexural behaviour of composite beams comprising of normal strength concrete (49 MPa) with those with UHPFRC (125 MPa). The results showed that UHPFRC composite beams had improved performance in terms of reduced cracking, increased stiffness and smaller deflections. Similar findings were observed by Hamoda et al. [12] who tested the hogging region of composite beams constructed with braced I-beams and with either normal-strength (32 MPa) or high-strength (68 MPa) concrete with steel fibres. The results of these tests showed that the addition of fibre increased the load to cause cracking, improved the stiffness of the cracked beam, reduced crack widths and increased the ultimate flexural capacity. Zhang et al. [21] found similar results when testing the hogging region of composite beams with UHPFRC slabs. Their test results showed that when applying 170 MPa UHPFRC in place of 50 MPa concrete, the cracking load increased by more than 300% and that cracking was reduced at all load levels. Liu et al. [22] also conducted testing on UHPFRC hogging regions and found that the presence of fibres can reducing concrete shrinkage strains and inhibit the propagation of the cracks. Yoo and Choo [20] further looked

to exploit the high strength and ductility of UHPFRC through the development of an inverted-T girder. In this study, it was shown that the application of UHPFRC in place of conventional concrete led to simplified detailing requirements and a highly ductile performance. From a design perspective, it was also shown that current approaches do not allow for the design of UHPFRC composites and new design approaches based on experimental data using UHPFRC are necessary.

Although broadly considered when testing steel concrete composite beams, the application of UHPFRC to composite slabs has not yet received attention. To date, research has focused on the application of normal strength concrete with low volumes of steel fibre (below that typically required to cause the strain hardening that characterises UHPFRC) [13, 23, 24]. For example, Abas et al. [23] tested eight two-span continuous composite slabs with fibre contents ranging from 0-40 kg/m3 and compared the results to those of slabs with conventional reinforcement. It was found that the addition of fibres reduced the slip between the profile deck and the concrete and that the peak flexural strength also increased. In the hogging region, it was found that for loads under 50% of the peak, fibres alone were able to provide sufficient crack control, but beyond this load level, the addition of conventional reinforcement was required. When considering the impact of fibres on longitudinal shear capacity, Bradford and Uy [25] found that the presence of fibres led to an enhancement in capacity.

Gholamhoseini et al. [13] later tested 16 composite slabs with varying fibre volume and traditional reinforcement ratios with the aim of investigating the impact of shrinkage on the serviceability performance. In this work, it was found that the addition of fibres reduced deflections and crack-widths and increased the moment capacity when compared to the performance of specimens without fibres. When considering time-dependent behaviour, it was found that the presence of fibres minimised cracking caused by restrained shrinkage. Importantly, while Abas et al. [21] observed that no further improvements in behaviour occurred when fibre dosage rates increased above 40 kg/$m^3$, Gholamhoseini et al. [13] found that concretes with a fibre dosage rate of less than 40 kg/$m^3$ performed almost identically to concretes without fibres in terms of crack control in the hogging region. This difference in findings indicates further work is required at considering varying fibre volumes.

Sarbini et al. [24] tested composite slabs in which a fibre reinforced topping was applied and it was found that the fibre reinforced concrete layer can arrest the growth of cracks which initiated in the conventional concrete layer. It was further found that replacing continuous

welded mesh reinforcement with the fibre reinforced concrete in the topping layer led to a minor increase in shear strength. Ackermann and Schnell [1] tested single and multi-span composite slabs with concretes containing fibres at dosage rates of either 60 or 100 kg/m3, the results of the tests show that the addition of fibres improves the rotation capacity and ductility and increases moment redistribution.

While the literature reviewed above has shown the potential benefits of utilising fibre reinforced concretes and UHPFRC in composite beams and slabs, to date, testing on UHPFRC has largely focused on proof of concept at the beam-scale, and for slabs, testing is limited to normal-strength steel fibre reinforced concretes [10, 26-29]. To allow for improved design, it is now necessary to understand the factors that influence the bond between the composite deck when considering very-high and ultra-high performance concretes. This understanding is essential because it is this bond which provides transmission of shear stresses between the deck and the concrete, thereby ensuring the composite action and controlling behaviour at both the serviceability and ultimate limit states.

To quantify the bond between UHPFRC and profiled decks, two commonly applied profiled decks, namely a dovetailed profile deck which is applied when constructing short spans and a trapezoidal profile which is typically applied over long spans, are considered. The influence of the presence of fibres is considered by testing eight different mix designs of strengths between 100 MPa and 126 MPa both with and without fibres. In addition to investigating the influence of fibre reinforcement, the impact of the inclusion of coarse aggregate is also investigated by testing concretes with coarse aggregate and both with and without fibre reinforcement. The consideration of UHPFRC with coarse aggregate is important as it has significant impact on construction aspects (reduced cost and environmental impact) as well as influencing mechanical properties such as workability, stiffness and shrinkage [30-35]. In the remainder of the paper, existing methods for quantifying the bond between profiled decks and concrete are first reviewed and assessed. A rapid, low-cost test apparatus and procedure for processing test results is then proposed. This test method is then applied to a range of different concretes.

## 2. Review of existing bond test methods

Test methods for quantifying the bond between a profile sheet and the adjacent concrete can be broadly categorised between those that are based on beam scale testing [36, 37] and those that are based on small subcomponents [38-44].

### *2.1 Beam scale tests*

In the beam-scale approach, simply supported slabs are tested and an inverse analysis is used to infer the local bond properties [36]. For example when applying the *m-k* approach, using the results of member level testing, the average mechanical interlock and friction is determined. However, at the member level, the shear transferred between the concrete section and the profile sheet, at any given point along the span, is a function of the member geometry, reinforcement details, material properties, the applied load and degree of cracking. The average results obtained from the m-k method, therefore, do not necessarily represent the true local bond behaviour (a material property) but rather an average that is unique to the test conditions [2, 45].

Another commonly applied inverse analysis approach is the partial shear connection (PSC) method. When applying this method, the moment and compressive normal force on the concrete are predicted under boundary conditions corresponding to full and zero shear connection. The results of experimental tests are then used to predict the shear connection degree ($\eta$) from which the $q/\Delta$ relationship can then be inferred [3, 45-48]. As with the m-k approach, the $q/\Delta$ relationship obtained from the PSC approach is impacted by the assumptions made to predict behaviour under full, partial and null shear connection.

From a practical perspective, the scale of beam tests is also problematic, in that the time and cost required to undertake a reasonably sized test program may limit the breadth of test parameters investigated and the number of replicates tested, thereby reducing model reliability.

### *2.2 Small-scale tests*

As an alternative to beam-scale tests, a range of different small-scale test methodologies have been proposed to directly measure the interface bond between the profile sheet and concrete [38-44, 49]. While generally easier to conduct than beam-scale tests, issues with test setup and interpretation of results still exist.

Small-scale tests can broadly be categorised between those that require the application of lateral restraint to maintain rotational equilibrium and those that do not [39]. The significance of the difference between these major categories is shown in Fig. 1, in which the behaviour of a dovetailed (Fig. 1(a)) and trapezoidal profile (Fig. 1(b)) under load are shown.

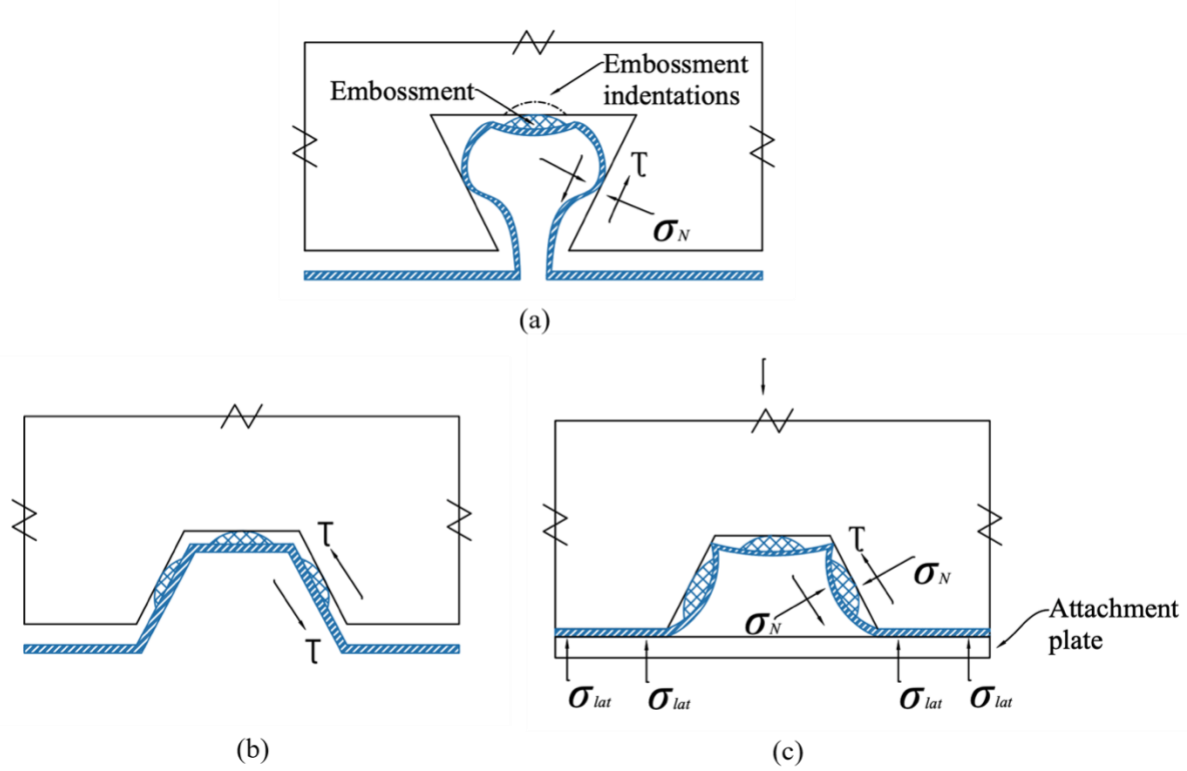


**Fig. 1.** Rib forces of a: a) dovetailed without restraint; b) trapezoidal without restraint; c) trapezoidal with restraint

Consider the re-entrant (dovetail) profile in Fig. 1(a) without any externally applied lateral restraint. Interface slip induces interface interlock as a result of the embossments at the upper flange forcing the rib to compress within the enclosed void created by the re-entrant shape [50], such that the shear flow is a function of the local shear ($\tau$) and normal stress ($\sigma_N$) at the interface. For the trapezoidal profile in Fig. 1(b), also without externally applied lateral restraint, interaction is also dominated by local shear but this is not as great as in the dovetail profile as the rib is not trapped within an enclosed void but tends to slip out as shown. In contrast in Fig. 1(c), the trapezoidal profile is restrained externally through the plate shown which prevents the lateral separation shown in Fig. 1(b) and also imposes the lateral stresses σlat in Fig. 1(c). Prevention of this lateral separation enhances the shear (τ) and normal stresses (σN) and, furthermore, they are further enhanced through σlat. It can be seen that any externally applied restraint to the bottom plate enhances the interface bond.

For tests with lateral restraint applied directly such as those proposed by Daniel et al. [38] in Fig. 2(a), the lateral forces Flat are applied to simulate the self-weight of the concrete and the lateral force is also required to maintain rotational equilibrium [39, 51]. As a result of these lateral forces Flat, an additional confining stress σlat is introduced into the specimens in Fig. 2

which changes the distribution of the normal ($\sigma_N$) and shear ($\tau$) stresses along the interface in Fig.1. Care is required during testing to ensure that the lateral forces in Fig. 2 are maintained at the desired level.

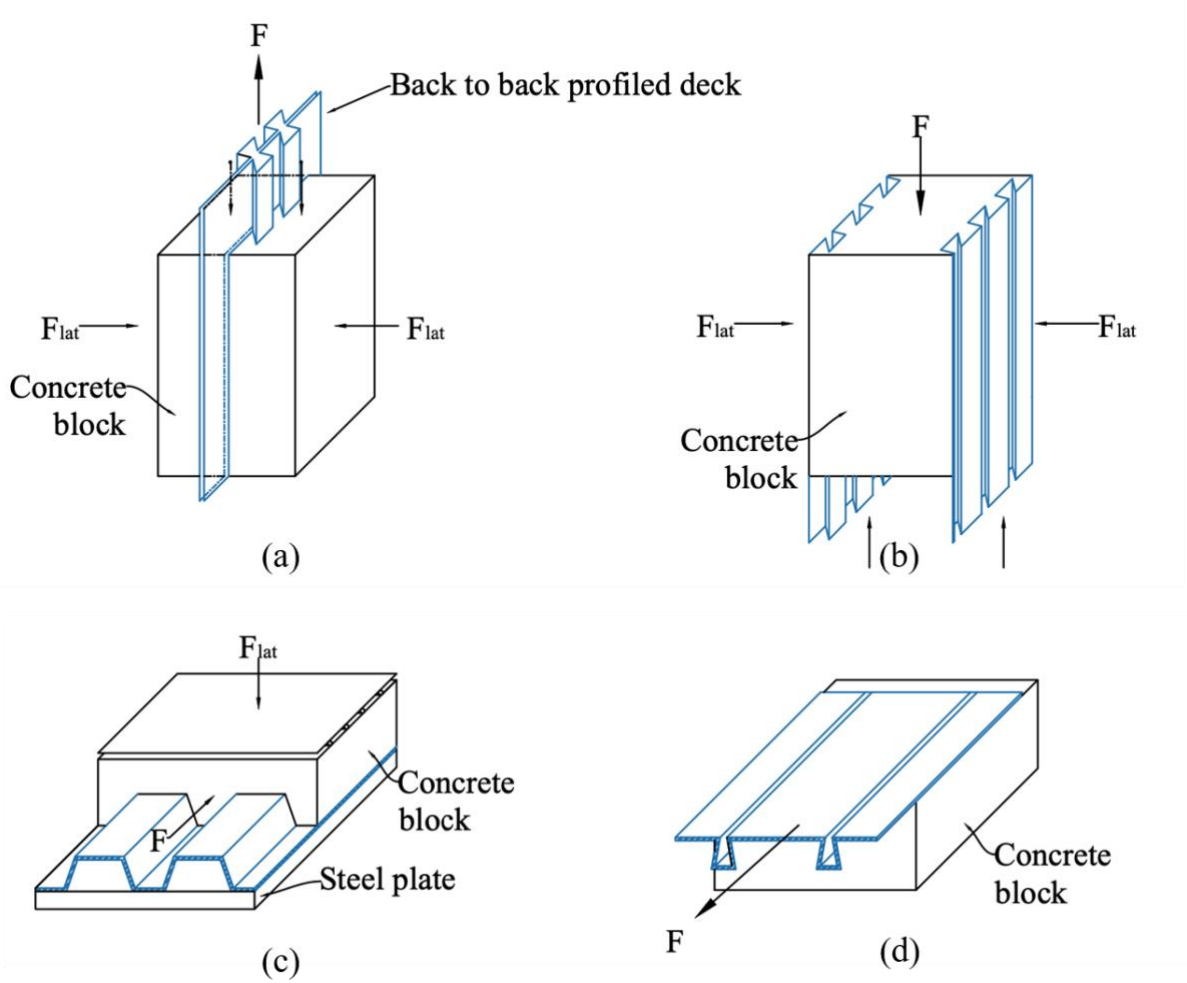


**Fig. 2.** Small-scale test approaches a) Daniel's test [38]; b) push-off test [39]; c) slip block test [54]; d) pull-out test [49]

In addition to the impact of lateral constraint, it is necessary to consider the way in which the test results will be processed in order to obtain the fundamental material properties. For example, in test methodologies which comprise of two separated interface surfaces, such as those in Fig. 2(b) [39], as a result of unavoidable variations in local properties, one surface will always reach its peak strength before the other; hence the peak bond strength is always taken as that of the weaker side [52]. This methodology introduces a bias into the results which requires the application of order statistics to remove, and which has very rarely been done in past studies. The analysis of the results from tests which consider two interfaces is further complicated after the first interface reaches its peak strength and begins to soften. The variation

in local bond properties can then result in redistribution of load at which point a simple averaging of the load-slip behaviour between the two sides of the test will not yield a prediction of the true interface properties [53].

Another type of small-scale member level test is the slip-block test [43, 49, 54-56] in Fig. 2(c), in which a small section of composite slab is fixed to a heavy base and the concrete is pushed off. This approach is beneficial in that it allows for the easy application of a normal force equivalent to the slab loading, but as discussed in [51], the profile is trapped between the concrete and the bottom steel plate and this can modify the rib forces (Fig. 1(c)).

Finally in Fig. 2(d), Yi et al. [49] recently proposed a pull-out test in which a profile sheet is pulled from a concrete block. This testing approach, while similar to what is proposed here has the critical difference in that a 'long' length of profile sheet is attached to the concrete such that it cannot necessarily be assumed interface slip is constant along the bonded length.

When considering the processing of global load/slip observations, such as the average values over the full bonded region of the specimens Fig. 2, to obtain local $q/\Delta$ material properties, such as the variation along the depth, it is also essential to consider if the methodology of inverse analysis captures the mechanism that controls behaviour. That is, when considering 'long' bonded interfaces in which the slip varies significantly over the bonded length, a simple conversion from applied load to shear stress by dividing loads by the bonded area will not directly yield a local material model [57]. This is because the average shear stress along the bonded interface is a lower bound to the maximum local shear stress or shear strength. This is important, because tests such as those in Fig. 2 are commonly applied using a simple averaging technique without considering the variation in slip along the bonded length.

### 2.3 *Single-lap shear test*

To address the limitations to current small scale test approaches identified above, an alternative test method based on single lap shear tests, commonly used to quantify the bond between concrete and reinforcing bars [57, 58] or concrete and fibre reinforced polymer sheets [53, 59], is used here. A similar approach has also recently been applied by [49], but with a long bonded length, and in this case the bonded length may limit the ability to directly quantify the shear flow without further detailed analysis. The approach is shown in Fig. 3 and consists of a concrete block cast onto a full-width profile sheet. For trial testing, the profile sheet was used with the profiled sheet clip connection left on the specimen free-edge. However for the main

tests, the sheet was cut such that the clip joint was placed within the specimen width rather than on the specimen free-edges. This approach for the main tests was taken to ensure the maximum number of ribs are contained within the central portion of the specimen and to minimise any torsion that may arise due to aasymmetry in the bond along the width of the specimen. It is also observed in Fig. 3(c) that the test is conducted without any additional normal forces to the sheet, although this testing approach deviates from what occurs in practice, (i.e. self-weight and live loads are applied to the slab) [54], the test was conducted with no external normal force to ensure a lower bound approach to the interfacial properties was obtained. Further, it can also be seen in Fig. 3(c) that no additional support is provided to the free-edges of the profile sheet, again this was done to ensure a lower-bound measurement of the interfacial properties were obtained.

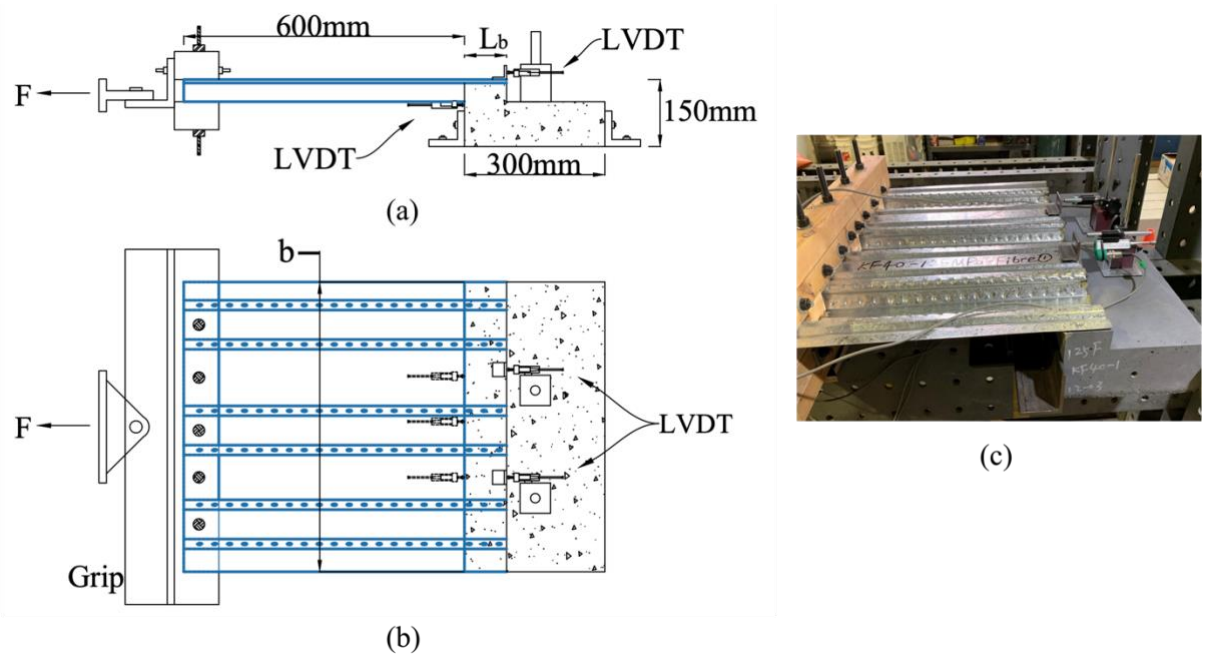


**Fig. 3.** a) Single lap shear test set-up; b) grip of the profile sheet; c) photograph of test set up

The bonded length of the profile sheet $L_b$ in Fig. 3 is chosen such that the bonded length is 'short', that is the slip remains essentially uniform between the loaded and free-end of the bonded region. This approach is taken such that a simple conversion of the applied load to a shear stress or shear flow as in Eq. 1 can be attributed to the loaded end-slip and is confirmed via trial testing described in the next section.

$$\tau = \frac{F}{L_b b}; \qquad q = \frac{F}{L_b} \tag{1}$$

where F is the applied load, b is the width of the bonded region, $\tau$ is the shear stress and q is the shear flow.

For testing, the profile sheet is gripped by a wooden block as in Fig. 3(c) that is cut to the shape of the profile and the section is aligned to ensure that the loading ram applies a concentric load. To further limit the potential for peeling due to misalignment of the ram, the unbonded length is maximised and here is taken as 600 mm as shown in Fig. 3(a). During testing, a hydraulic hand jack is used to pull the sheet and the displacement of the free and loaded-end is measured by 6 LVDTs. To remove the influence of any chemical bond, the specimens are initially loaded until a free end slip of 0.1 mm is reached and then unloaded to zero load before reloading until complete detachment of the sheet.

## 3 Experimental program

### *3.1 Mix design*

To quantify the impact of concrete strength, high fibre volumes and the presence of coarse aggregate on the interface bond, eight cement based concrete mix designs were used to manufacture the specimens shown in Fig. 3. The mix designs are given in Table 1 where the mix components in Columns 2 to 6 are given a proportion of the cement content by weight and the fibre content in Column 7 is given as a percentage of the total volume. The mix identification (ID) is given in Column 1 where for example in mix M-0.21-0F: the letter M refers to a mortar mix that is a mix without coarse aggregate; 0.21 is the water content as a proportion of the cement content; and 0F means 0% of fibres by volume. Similarly for C0.5-0.19-2F: the C refers to a concrete mix that is a mix with coarse aggregate in which the coarse aggregate content is 0.5 as in Column 3 in Table 1; followed by the water content 0.19 from Column 6; and then the fibre content of 2% from Column 7. The concrete mix designs in Table 1 were based on the UHPFRC mix design developed in [60] which were modified to reduce strengths either by the addition of water or the addition of coarse aggregate. Throughout casting for both mixes with and without coarse aggregate not fibre agglomeration was observed.

**Table 1:** Mix content as a proportions of cement

| Mix ID (1) | Silica fume (2) | Coarse aggregate (3) | Sand (4) | HRWRA (5) | Water (6) | Fibre (7) |
|---|---|---|---|---|---|---|
| M-0.21-0F | 0.2661 | 0 | 1 | 0.045 | 0.21 | 0.166 |
| M-0.19-0F | 0.2661 | 0 | 1 | 0.045 | 0.19 | 0.166 |
| C0.7-0.19-0F | 0.2661 | 0.6875 | 0.6875 | 0.045 | 0.19 | 0.166 |
| C0.5-0.19-0F | 0.2661 | 0.5 | 0.5 | 0.045 | 0.19 | 0.166 |
| M-0.21-2F | 0.2661 | 0 | 1 | 0.045 | 0.21 | 0.166 |
| M-0.19-2F | 0.2661 | 0 | 1 | 0.045 | 0.19 | 0.166 |
| C0.7-0.19-2F | 0.2661 | 0.6875 | 0.6875 | 0.045 | 0.19 | 0.166 |
| C0.5-0.19-2F | 0.2661 | 0.5 | 0.5 | 0.045 | 0.19 | 0.166 |

All mixes were produced using sulphate resisting cement conforming to AS 3972 [61], silica fume conforming to AS 3582.3 [62], washed river sand with a fineness modulus of 2.49, coarse aggregate with maximum size of 4.75 mm and a fineness modulus of 5.93, and a high range water reducing agent with added retarder (HRWRA). For the mixes with fibres, steel microfibers with a length of 13 mm, diameter of 0.2 mm and with tensile strength of 2500 MPa were used. Concrete compressive strengths and elastic moduli were obtained by testing 6 cylinders (100 mm diameter, 200 mm height) of each concrete type on the same day as conducting the pull-tests. The elastic modulus of the concrete was determined according to AS1012.17 using the average reading of two 30 mm strain gauges located at mid height.

### *3.2 Profiled sheet*

The cross-sections of the specimens are shown in Fig. 4. To identify the impact of the profile sheet shape, both a dovetailed (designated DT) and a trapezoidal (designated TR) sheet with a thickness of 1 mm were used and which had the dimensions in Fig. 4. The geometric and material properties of these specimens are given in Table 2 where $f_y$ is the yield strength and Er the elastic modulus of the profiles that were determined from dog-bone tests that had a shank of 120 mm and width of 20 mm, and were tested in accordance with AS 1391 [63]. Furthermore

in Table 2, As is the cross-sectional area of the profile in a specimen, *w* the width and *d* the depth of the profile also shown in Fig. 4.

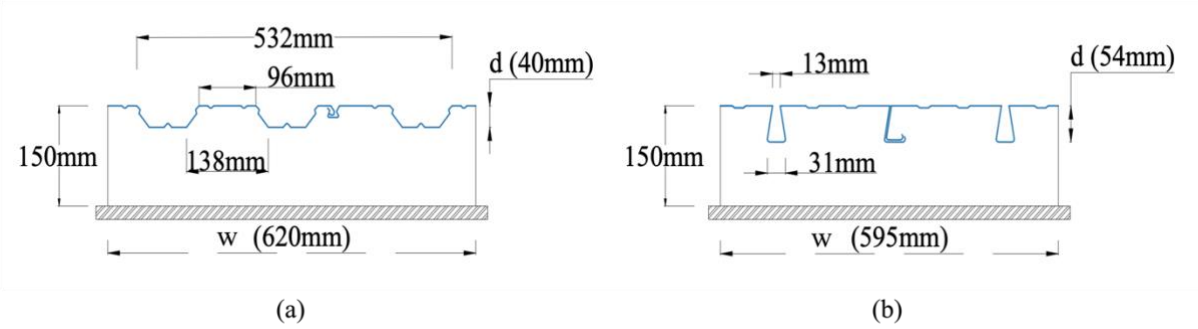


**Fig. 4.** Cross-sectional configuration of specimen a) trapezoidal (TR); b) dovetailed (DT)

**Table 2:** Profile sheet geometric properties

| | $f_y$ (MPa) | | $E_r$ (GPa) | | $A_s$ (mm$^2$) | $w$ (mm) | $d$ (mm) | Embossment spacing (mm) |
|---|---|---|---|---|---|---|---|---|
| Profile ID | Manufacturer | Tested | Manufacturer | Tested | | | | |
| DT | 500 | 654 | 200 | 212 | 990 | 595 | 54 | 28 |
| TR | 500 | 676 | 200 | 220 | 830 | 620 | 40 | 30 |

### *3.3 Single lap shear tests*

To enable quantification of the influence of the concrete strength, the presence of aggregate and the presence of fibres on both the dovetailed and trapezoidal deck, 48 single-lap shear tests were conducted. The parametric variations of these tests is outlined in Table 3 where for each combination of parameters three replicates were tested. To facilitate reference to specific test series, each group of specimens is designated according to deck type (DT or TR) followed by a number corresponding to the concrete strength at the time of testing, and a simplified designation for the concrete mix type which indicates the coarse aggregate content and the fibre content. For example specimens designated DT-117-0-0 were conducted on dovetailed profile sheets with a mortar of 117 MPa, containing no coarse aggregate nor fibres. While specimen TR-107-0.5-2 had a trapezoidal profile sheet, 107 MPa concrete containing coarse aggregate at a mass ratio of 0.5 and 2% fibres by volume. The mix ID is also given in Column 5 and

relates to the contents in Table 1. Also listed in Table 3 are the concrete cylinder strength $f_c$ and moduli $E_c$ at testing.

**Table 3:** Test specimens

| Test ID | Deck type | $f_c$ $(MPa)$ | $E_c$ $(MPa)$ | Mix ID | Concrete type |
|---|---|---|---|---|---|
| DT-117-0-0 | DT | 117 | 35,600 | M-0.21-0F | UHPC |
| DT-126-0-0 | | 126 | 41,400 | M-0.19-0F | |
| DT-100-0.7-0 | | 100 | 39,800 | C0.7-0.19-0F | |
| DT-120-0.5-0 | | 120 | 41,300 | C0.5-0.19-0F | |
| TR-117-0-0 | TR | 117 | 35,600 | M-0.21-0F | |
| TR-126-0-0 | | 126 | 41,400 | M-0.19-0F | |
| TR-100-0.7-0 | | 100 | 39,800 | C0.7-0.19-0F | |
| TR-120-0.5-0 | | 120 | 41,300 | C0.5-0.19-0F | |
| DT-100-0-2 | DT | 100 | 34,800 | M-0.21-2F | UHPFRC |
| DT-126-0-2 | | 126 | 41,100 | M-0.19-2F | |
| DT-107-0.7-2 | | 107 | 40,900 | C0.7-0.19-2F | |
| DT-107-0.5-2 | | 107 | 38,100 | C0.5-0.19-2F | |
| TR-100-0-2 | TR | 100 | 34,800 | M-0.21-2F | |
| TR-126-0-2 | | 126 | 41,100 | M-0.19-2F | |
| TR-107-0.7-2 | | 107 | 40,900 | C0.7-0.19-2F | |
| TR-107-0.5-2 | | 107 | 38,100 | C0.5-0.19-2F | |

### *3.4 Quantification of bonded length through trial testing*

Bonded lengths of 90 mm, 135 mm and 180 mm, which corresponds to at least 3, 4 or 5 embossments over the bonded length respectively, were tested in order to identify the optimal bonded length $L_b$ in Fig. 3 to give a uniform shear flow. Specimens for each bonded length and for each profile, that is dovetail and trapezoidal, were cast using mix M-0.19-0F.

These specimens were tested to compare the loaded-end slip with the free-end slip. The results for each bonded length are shown in Fig. 5, in which q is the shear flow force (F/$L_b$) and $\Delta$ is the end-slip. For the dovetailed sections, the full test range of slips are given in Fig. 5(a). The

first 5 mm are enhanced in Fig. 5(b) where for example 90FE is the free end slip of the 90 mm bonded length and 135LE is the loaded end slip of the 135 mm boned length. The results for the trapezoidal section are shown in Figs. 5(c) and (d). Figs. 5(a) and (b) for the DT sheet do not show a result for the 180 mm bonded length because this specimen was damaged prior to testing.

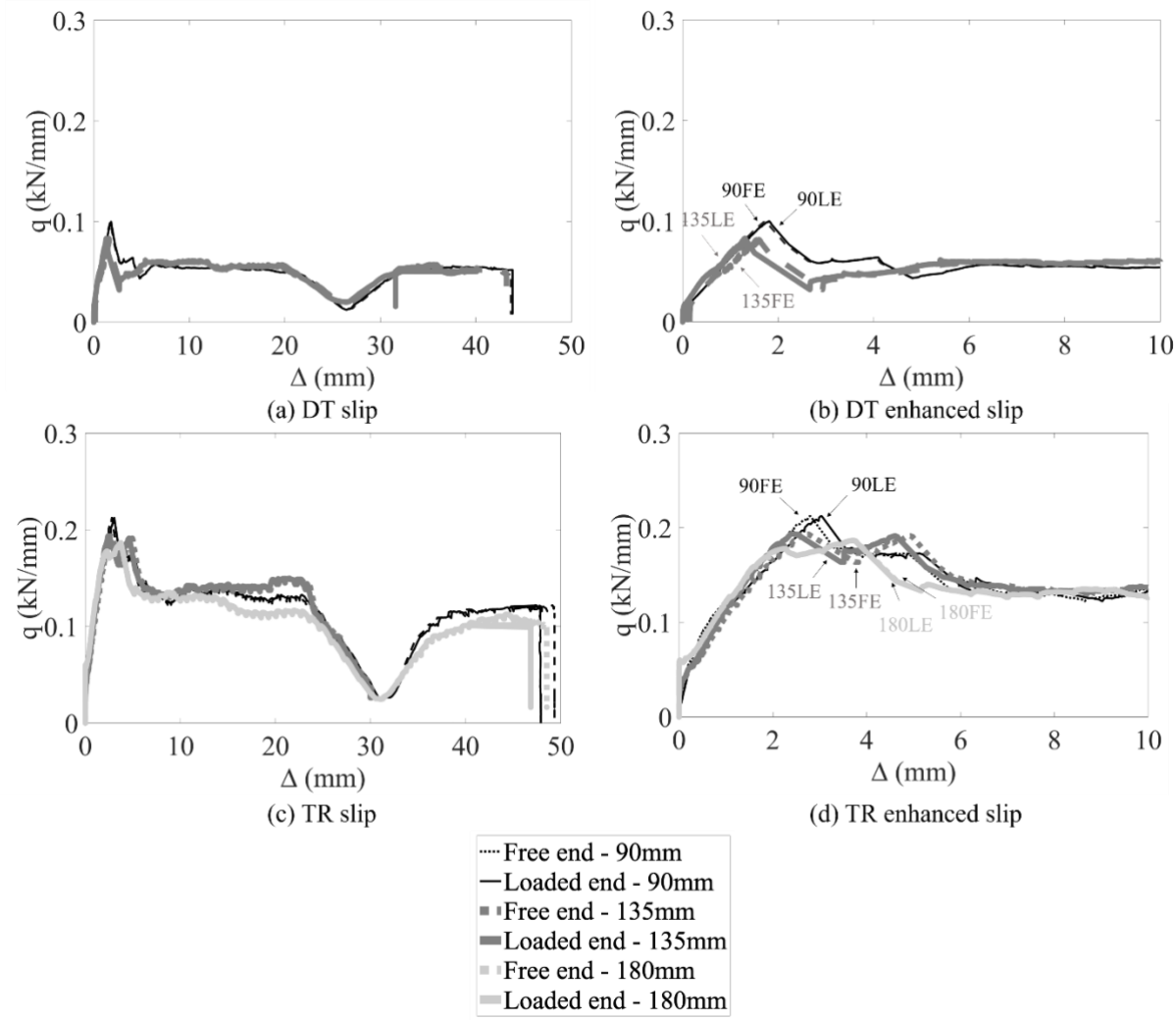


**Fig. 5.** Variation in loaded and free end slips

Comparing the dovetail response in Fig. 5(a) with the trapezoidal response in Fig. 5(c), it can be observed that there is in general a very similar shaped *q/Δ* response. This is characterised by a stiff loading branch followed by a rapid reduction in shear flow post-peak strength and then a relatively uniform residual branch. Further focusing on the first 5 mm of slip, it can be observed that the DT sheet (Fig. 5(b)) has a much less ductile response, with a sudden increase in slip and reduction in shear flow following once the peak shear flow is reached. In comparison, the results obtained from the TR sheet in Fig. 5(d) show that although a sudden

increase in slip occurs, the corresponding reduction in q is small giving a much more ductile response compared to that of the dovetail section.

When considering the variation in behaviour arising from the change in bonded length, all results in Fig. 5 show that the average shear flow calculated using Eq. 1 reduces as the bonded length increases. This behaviour is seen most clearly by comparing the peak shear flow for each deck type in Figs. 5(b) and (d). This variation is significant as it indicates that the bond stress varies along the bonded length. Similarly, by comparing the $q/\Delta$ response calculated using either the free-end or loaded-end slip in Figs. 5(b) and (d), it can be seen that as the bonded length is reduced so too is the difference between the slip at the loaded and free ends. The difference is minimal for the 90 mm bonded length for both profiles which indicates that the variation in shear flow along the bonded length is minimised by minimising the bonded length.

## 4. Single lap shear test results

In this section, the impact of coarse aggregates and fibres will be investigated for each deck type by considering the variation in properties described in Table 3. In the following subsections, the results from each individual test (loaded-end slip $\Delta$ and shear flow $q$ obtained from Eq. 1 normalised by the factor $\sqrt{f_c}$ to allow for variations in concrete strength) are shown as thin lines and the average of the three replicates test is shown as a heavy line so that the scatter of the results can be observed. The results of each individual test along with a photo of the specimen following testing can be found in Supplementary Material A.

### *4.1 Concrete without fibres*

The results of all tests conducted on mixes without fibres are shown in Fig. 6, where Figs. 6(a) and (b) are the results from mixes with no coarse aggregate and strengths 117 MPa and 126 MPa respectively. Whereas Figs. 6(c) and (d) are for mixes with coarse aggregates and strengths 100 MPa and 120 MPa respectively. Within each figure: the results on tests on both dovetailed sheets (DT) and trapezoidal sheets (TR) are also shown; the individual results are shown as thin lines; and the means are shown as thick lines.

Importantly within each series of tests, it can be seen that although there is significant scatter in the magnitudes of the $q/\Delta$ responses (indicated by the variation in the thin lines in each sub-

plot), there is an overall trend in the shape of the $q/\Delta$ relationship as shown by the thick lines that is the average results. For the average of the DT specimens, the $q/\Delta$ response is characterised by an initial stiff loading branch until the average ultimate shear flow $q_{pk}$ of 0.207 kN/mm is reached at an average slip of 0.920 mm. The shear flow then gradually reduces until the test is terminated at $\Delta$ of approximately 50 mm. For the TR profile, the $q/\Delta$ response is characterised by a stiff loading branch leading to an initial peak in the shear flow followed by a rapid decline before a second rising branch with that peaks $q_{pk}$ at an average value of 0.16 kN/mm at an average slip of 10.5 mm.

In both sets of test results, a dip in the shear flow is observed at slips of approximately 28 mm for the DT sheet and 30 mm for the TR sheet and this approximately corresponds to the clear spacing of the embossments on the profile. That is as the profile is pulled, it initially rises out of the concrete key that is formed during casting which provides the vertical separation necessary to generate the interface interlock described in Fig. 1. As the profile is pulled a distance equal to the clear embossment spacing, the embossment falls into an adjacent concrete key and interface interlock is reduced thereby reducing the shear flow. Upon further pulling the profile, the embossment rises from the key and interface interlock is restored and the shear flow increases.

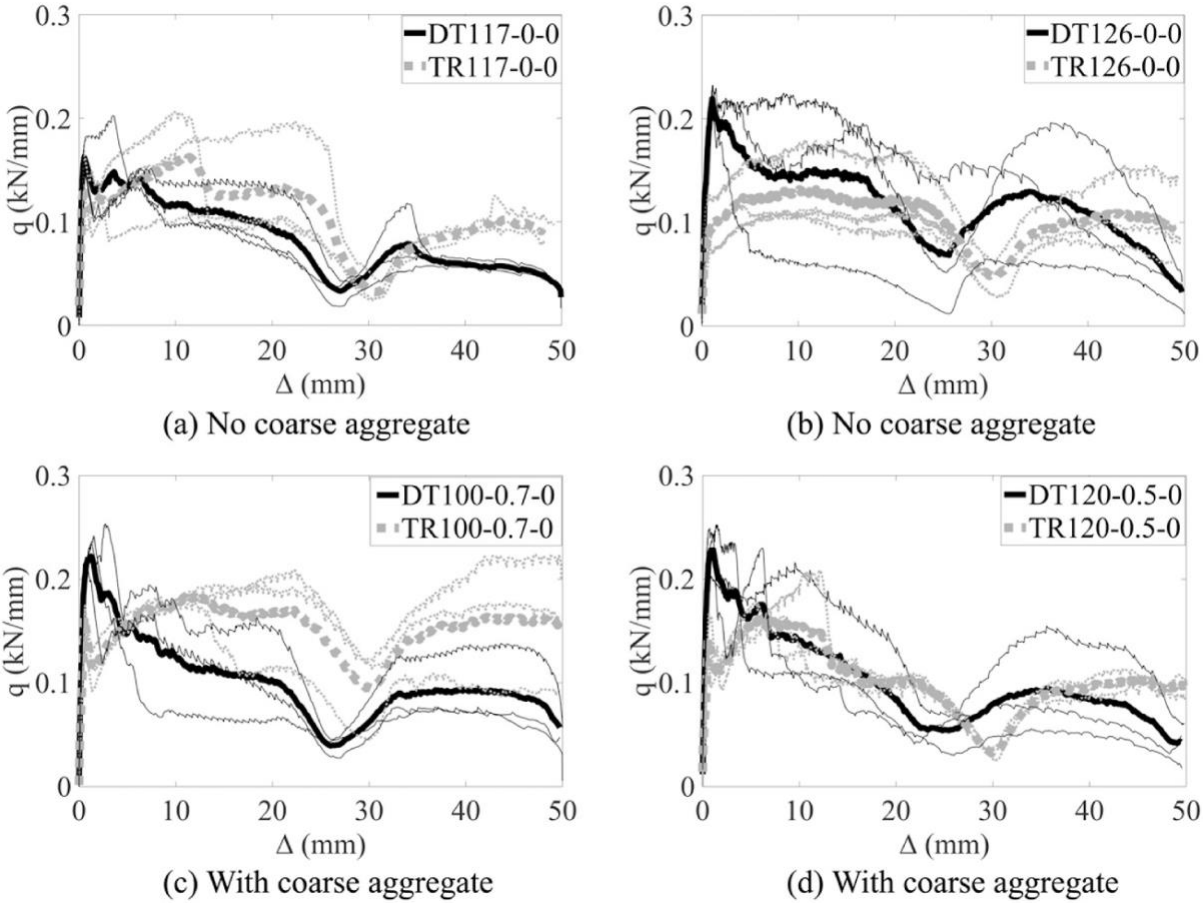


**Fig. 6.** Full-range $q/\Delta$ response for UHPC without fibres

Photographs of typical sections following testing in which the profile sheet has been pulled completely from the concrete are shown in Fig. 7 for specimens without fibres; the designations are ended with the trial test serial number. From these figures it can be seen that two distinct failure modes are observed: the first in Figs. 7(a) and (b) corresponds to when the sheet was pulled from the concrete without any significant underlying damage; and the second in Figs. 7(c) and (d) shows a test in which the underlying concrete was cracked as the profile was pulled. In Supplementary Material A, a photo and the corresponding $q/\Delta$ relationship for each individual test is presented and it is observed that for those specimens in with a fracture occurred the shear flow undergoes a sudden reduction at the point of cracking. The experimental variation observed in Fig. 6 can be partially explained by the difference in this cracking behaviour, that is once a crack occurs slip is no longer only along the interface between the profile sheet and the concrete, but rather there is an additional frictional component as the fractured concrete planes slide against each other, with the total magnitude of the friction proportional to the surface area of the fractured concrete plane.

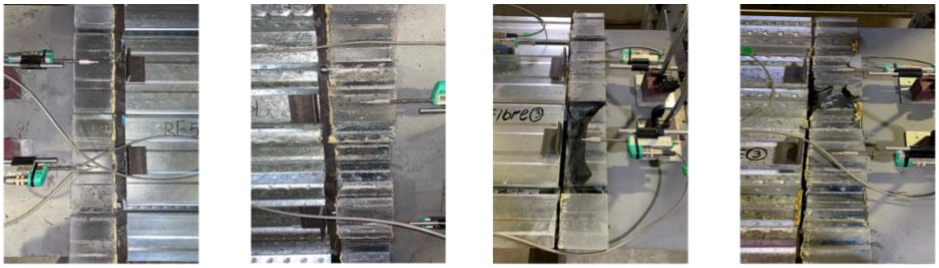

(a) DT126-0-0F- *2* (b) TR126-0-0F- *1* (c) DT117-0-0F- *3* (d) TR117-0-0F- *3*

**Fig. 7.** Typical failures of specimens without fibres a) DT; b)TR where cracking did not occur, and c)DT; d)TR where cracking did occur.

Within each sub-plot in Fig. 6, it can be observed by comparing the average DT and TR responses, that there is a significant difference in the $q/\Delta$ relationship. This can be explained by the different mechanisms shown in Fig. 1. For the dovetailed sheet as the profile is pulled, the presence of the embossments cause a vertical separation of the sheet from the concrete resulting in the rib compressing within the concrete void and interface interlock. This creates additional normal stresses along the interface resulting in increased shear transfer due to confinement. Although this same mechanism also occurs in the TR profile, the trapping of the profile within the void for the DT sheet results in more significant confinement than for the TR sheet. This finding aligns with the study of [39] who considered profiled sheets with different trough inclinations.

In the photos of individual test specimens in Supplementary Material A, it can be observed that when a specimen cracks, a sudden drop in the shear flow occurs. For example considering test series DT126-0-0, in two of the three tests a crack formed during loading and these specimens are observed to have less ductility (quantified as the area under the $q/\Delta$ response) than the test in which cracking did not occur.

For each type of profile sheet tested, the average result of each test series is plotted in Fig. 8 but now with the shear flow normalised by the square root of the compressive strength, which is an approximation of the tensile strength and therefore has units of N/mm$^2$, in order to allow for easier comparison across different concrete strengths. The full $\frac{q}{\sqrt{f_c}}/\Delta$ response of the DT sheet shown in Fig. 8(a) and the first 10 mm of slip in Fig. 8(b). Also provided in Table 4 are

the average ductilities measured as the average area under the $\frac{q_{pk}}{\sqrt{f_c}}/\Delta$ relationship over either the first 10 mm of slip or over the full range of slip (taken here to be 46 mm as this is the minimum slip recorded in all tests). The corresponding results in the same format for the TR sheet are shown in Figs. 8(c) and (d).

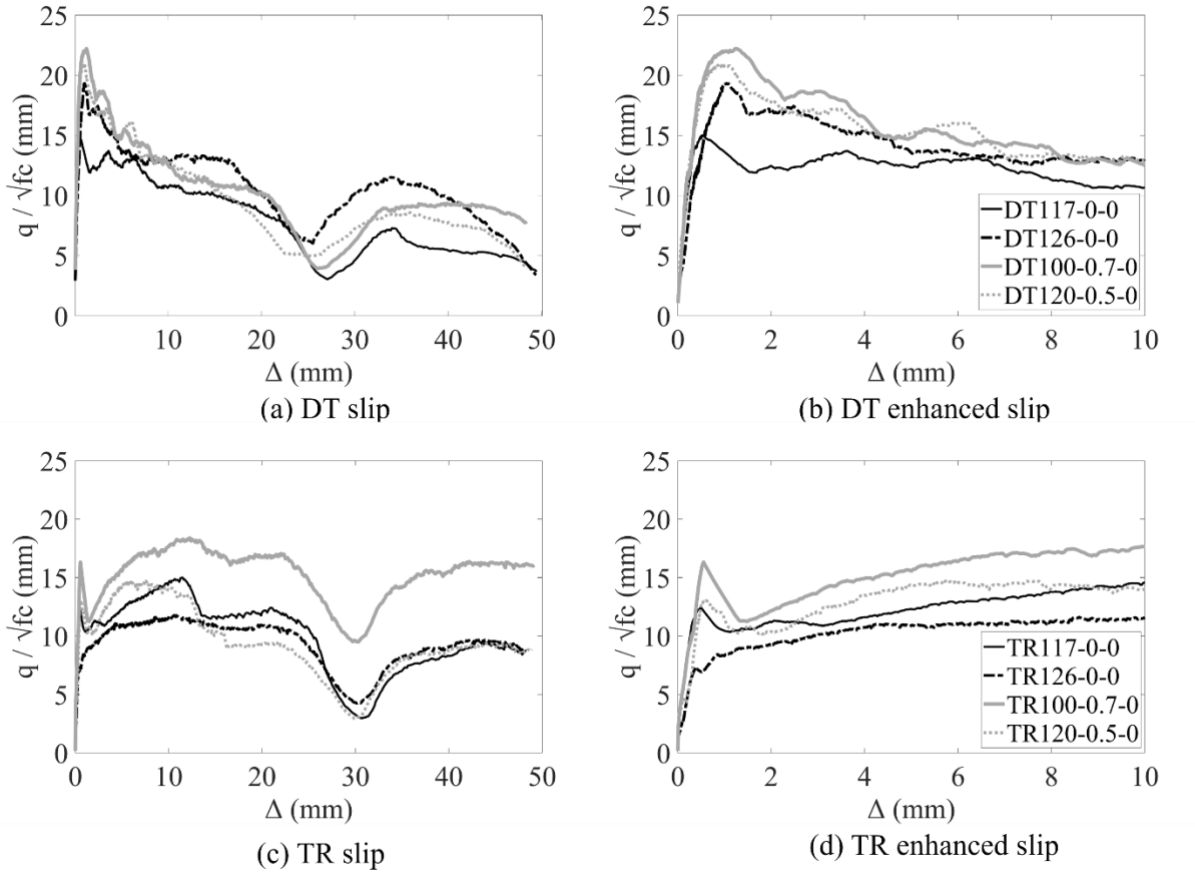


**Fig. 8.** Average $\frac{q}{\sqrt{f_c}}/\Delta$ response for UHPC without fibres

**Table 4:** Summary of key points on the $\frac{q_{pk}}{\sqrt{f_c}}/\Delta$ relationship - UHPC

| Test ID | Average $\Delta_{pk}$ (mm) | Average $\frac{q_{pk}}{\sqrt{f_c}}$ (mm) | Average ductility ($mm^2$) (for 10 mm) | Average ductility ($mm^2$) (46 mm) |
|---|---|---|---|---|
| DT-117-0-0 | 0.521 | 16.2 | 122 | 368 |
| DT-126-0-0 | 1.04 | 21.7 | 143 | 505 |
| DT-100-0.7-0 | 1.26 | 22.21 | 158 | 473 |
| DT-120-0.5-0 | 0.855 | 22.8 | 154 | 440 |
| TR-117-0-0 | 11.4 | 13.5 | 122 | 456 |

| | | | | |
|---|---|---|---|---|
| TR-126-0-0 | 10.6 | 13.2 | 102 | 428 |
| TR-100-0.7-0 | 12.25 | 18.38 | 151 | 698 |
| TR-120-0.5-0 | 5.77 | 16.16 | 129 | 433 |

First consider the DT sheet. In Fig. 8(b) and Table 4, it can be observed that although the concrete strength varies by 26% between all tests (from 100 MPa to 126 MPa) $q_{pk}$ shows little variation; the exception to this is the average result of DT-117-0-0 which has a peak shear flow approximately 27% lower than that of the remaining tests. It is, however, felt that this result can be considered as an outlier because it sits outside of the trend of the remaining results and has a far lower strength than that obtained from the 100 MPa concrete (DT-100-0.7-0). When examining the full range $\frac{q}{\sqrt{f_c}}/\Delta$ relationship in Fig. 8(a), there is little variation between the averages of each test series and there is no observable correlation with concrete compressive strength. That is, although the average $q_{pk}$ for specimens DT-117-0-0 was significantly lower than for the remaining series, the response converges to that of the other test series for slips greater than about 6 mm. This convergence in the $\frac{q}{\sqrt{f_c}}/\Delta$ response is expected because at larger slips the mechanism of shear transfer is expected to be dominated by friction and this should be independent of concrete compressive strength provided the concrete is of sufficient strength to avoid significant damage [13, 41].

Now consider the results for the TR sheet. In Fig. 8(d), it can be observed that although the first peak in shear flow is significantly more affected by the compressive strength than that observed for the DT sheet (see scatter between the first peak in Fig. 8(b) versus Fig. 8(d)), there is again no correlation between the first peak shear flow and the concrete compressive strength. It can also be seen that there is again an outlier (TR-126-0-0), which although having the highest concrete compressive strength, is observed to have the lowest initial peak at $\frac{q}{\sqrt{f_c}} \approx 7.12$ mm. Examining the full range $\frac{q}{\sqrt{f_c}}/\Delta$ response in Fig. 8(c), it can be seen that there is significantly larger scatter in $\frac{q}{\sqrt{f_c}}$ and the corresponding $\Delta$ for the TR sheet with $\frac{q}{\sqrt{f_c}}$ ranging from 13.2 mm to 18.38 mm and the corresponding slips ranging from 5.77 mm to 12.25 mm; there is, however, no clear correlation between these values and the concrete compressive strength.

The impact of coarse aggregate can be identified by comparing the results of mixes with coarse aggregate to those without. In Fig. 8 over the 10 mm range of slips, it can be observed that the normalised shear flow is generally higher for mixes with coarse aggregate but that over the full 50 mm range of testing the response of the mixes with coarse aggregate generally converges on those of the mixes without coarse aggregate. The higher shear flow for mixes with coarse aggregate may be due to additional interlock provided by the aggregate. It would appear that for the mixes tested here, the presence of coarse aggregate does not appear to have any significant negative impact on the $\frac{q}{\sqrt{f_c}}/\Delta$ relationship. Hence its inclusion in UHPC mix designs used for composite slabs may be beneficial in reducing both the cost of the mix design [30-35]; further testing is, however, required to ensure that negative impacts for coarse aggregate inclusion do not occur at the member level.

### *4.2 Concrete with fibres*

The results of tests with fibres are shown in Fig. 9, in which Figs. 9(a) and (b) are for concretes without coarse aggregates, and Figs. 9(c) and (d) are for concretes with coarse aggregates. Again in these plots, the thick lines refer to the average results tests for the dovetailed and trapezoidal sheets.

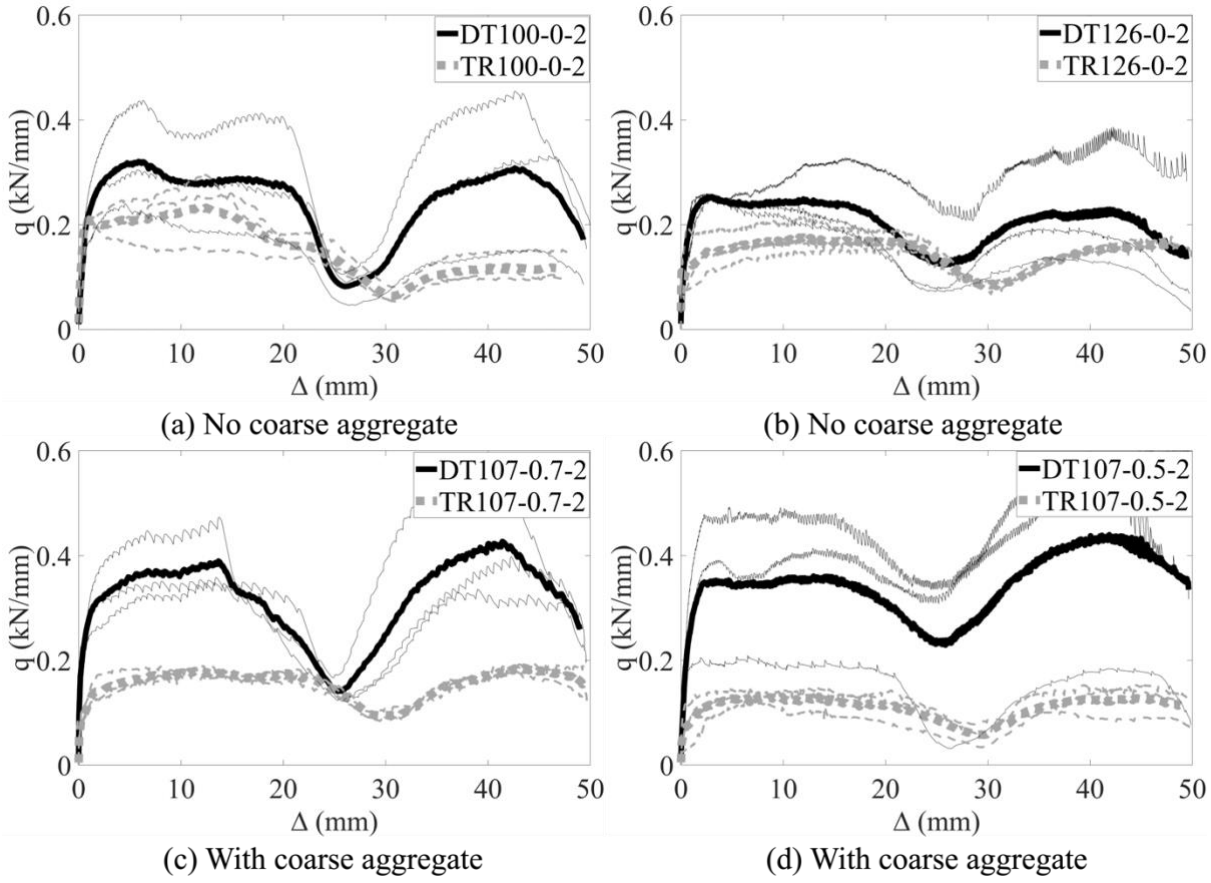


**Fig. 9.** Full-range $q/\Delta$ response for UHPFRC

Examining the results in Fig. 9, regardless of the concrete strength or tested profile type, it can be seen that the general shape of the $q/\Delta$ response is very similar. The response is characterised by an initially stiff rising branch before a long plateau which has a similar magnitude to the $q_{pk}$, which makes the overall $1/\Delta$ relationship highly ductile.

Photographs of typical sections with fibres following testing are show in Fig. 10. It can be seen that again, in a proportion of the tests the concrete fractured, but in this case, the fracture has been restrained by the presence of fibres. Therefore sudden reductions in shear flow that were observed in specimens without fibres are not observed to the same extent in specimens with fibres.

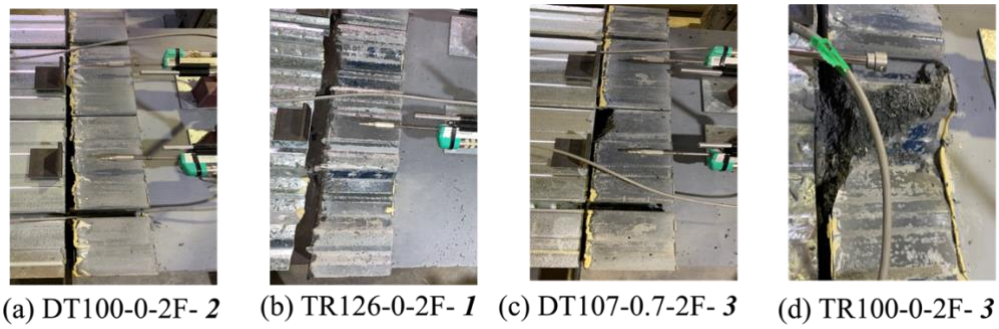

(a) DT100-0-2F- ***2*** (b) TR126-0-2F- ***1*** (c) DT107-0.7-2F- ***3*** (d) TR100-0-2F- ***3***

**Fig. 10.** Typical failures of specimens without fibres (a)DT (b)TR where cracking did not occur, and (c)DT (d)TR where cracking did occur.

To enable a comparison of tests with different concrete strengths, the average $\frac{q}{\sqrt{f_c}}/\Delta$ response of each series of tests using the DT profile is shown in Fig. 11(a), with a focus on the first 10 mm shown in Fig. 11(b). A summary of the peak shear flow and the corresponding slip is presented in Table 5. Interestingly, it can be seen in Figs. 11(a) and (b) and in Table 5 that the highest concrete strength (126 MPa) yields a similar peak to that for the remaining three compressive strengths (ranging from 100 MPa to 107 MPa) such that there is no clear correlation between $\frac{q}{\sqrt{f_c}}$ and compressive strength.

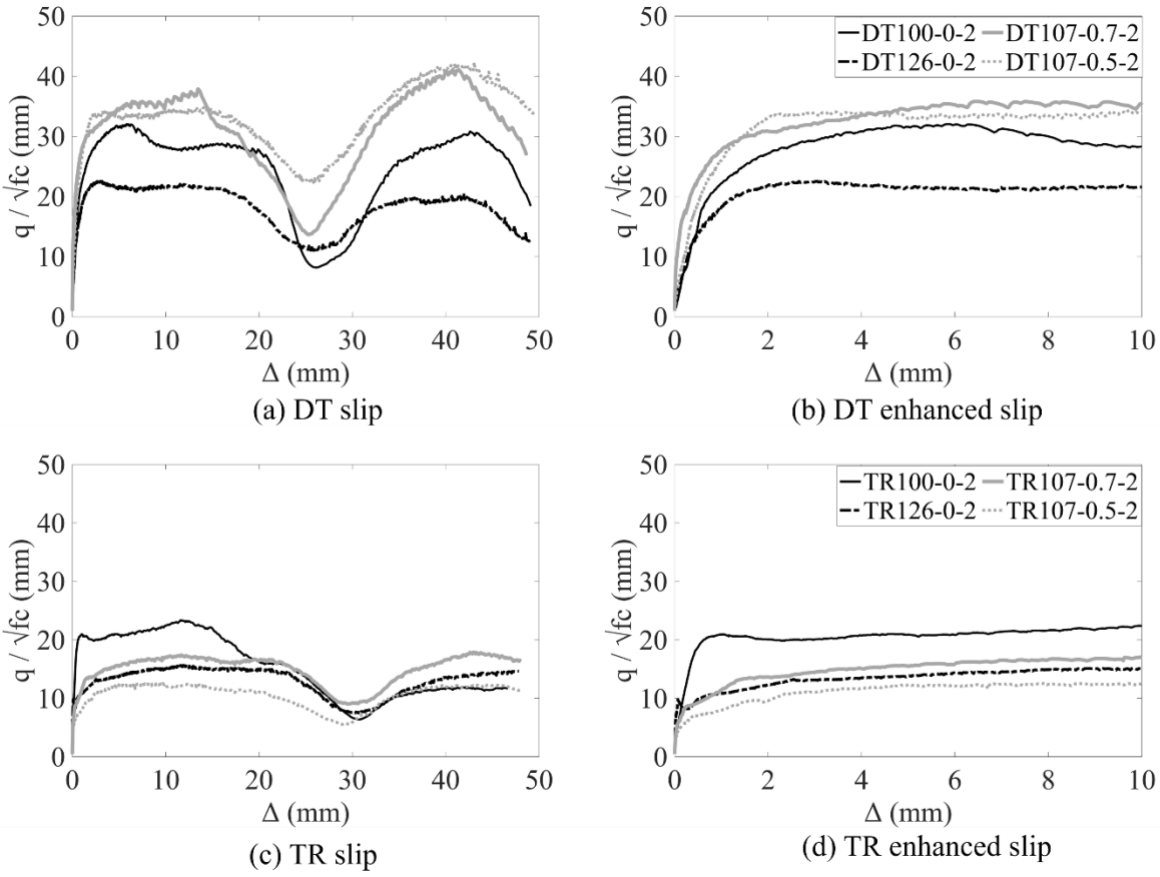


**Fig. 11.** Average $\frac{q}{\sqrt{f_c}}$/Δ response for UHPFRC

Now considering the TR profile in Figs. 11(c) and (d), it can again be observed that there is no clear correlation between $\frac{q}{\sqrt{f_c}}$ and the compressive strength. For example, the highest shear flow is obtained when the concrete strength is minimum and in the remaining tests, although the variation in concrete strength is only 7 MPa the peak normalised shear flow varies by 5.3 ~ 10.3 mm (23% ~ 44%).

**Table 5:** peak shear flow and corresponding slip - UHPFRC

| Test ID | Average $\Delta_{pk}$ (mm) | Average $\frac{q_{pk}}{\sqrt{f_c}}$ (mm) | Average ductility ($mm^2$) (10 mm) | Average ductility ($mm^2$) (46 mm) |
|---|---|---|---|---|
| DT-100-0-2 | 5.85 | 32 | 280 | 1125 |
| DT-126-0-2 | 3.03 | 25.3 | 206 | 844 |
| DT-107-0.7-2 | 13.45 | 39.2 | 326 | 1419 |
| DT-107-0.5-2 | 14.05 | 36 | 316 | 1517 |
| TR-100-0-2 | 11.6 | 23.3 | 205 | 706 |

| | | | | |
|---|---|---|---|---|
| TR-126-0-2 | 11.96 | 17.6 | 134 | 593 |
| TR-107-0.7-2 | 11.65 | 18 | 148 | 683 |
| TR-107-0.5-2 | 9.72 | 13 | 111 | 483 |

Now considering the impact of aggregate on the $q/\Delta$ relationship for concretes with fibres. Firstly considering the results for the DT sheet in Figs. 11(a) and (b), by comparing the results of the two tests with the same compressive strength (107 MPa) and differing volumes of coarse aggregate (DT-107-0.7-2 and DT-107-0.5-2) with the result of the mix with no coarse aggregate (DT-126-0-2) and a 100 MPa compressive strength (DT-100-0-2). This comparison shows that the presence of coarse aggregate generates a small improvement in strength, but that the improvement is not sensitive to the volume of coarse aggregate. The improvement in strength is likely due to increased confinement cause by aggregate interlock in the dovetailed void after cracking, but given the small magnitude in change, further experimental investigation with more variations in aggregate content are required. Most importantly, however, this comparison shows that the presence of aggregate does not negatively disrupt the distribution of fibres and, therefore, the incorporation of aggregates can be used as a method to reduce the cost of UHPFRC for composite slabs using the tested DT profiles.

By comparing the results of the TR-107-0.7-2, TR-107-0.5-2 and TR-100-0-2 tests in Figs. 11(c) and (d), the presence of aggregate in the trapezoidal profile appears to significantly reduce the shear flow, particularly over the first 20 mm of slip. Given the very small variation in individual test results shown in Figs. 9(c) and (d) for concretes containing aggregate, this behaviour cannot be explained by experimental scatter and further research is required to identify the mechanism involved.

### *4.3 Comparison of concrete with and without fibres*

To allow for further comparison of the impact of fibres, the average result of all tests conducted on a single concrete type (identical water to binder ratio, fine aggregate content and coarse aggregate content) are shown in Fig. 12, in which the solid lines refer to concrete without fibres and the broken lines refer to concrete with fibres.

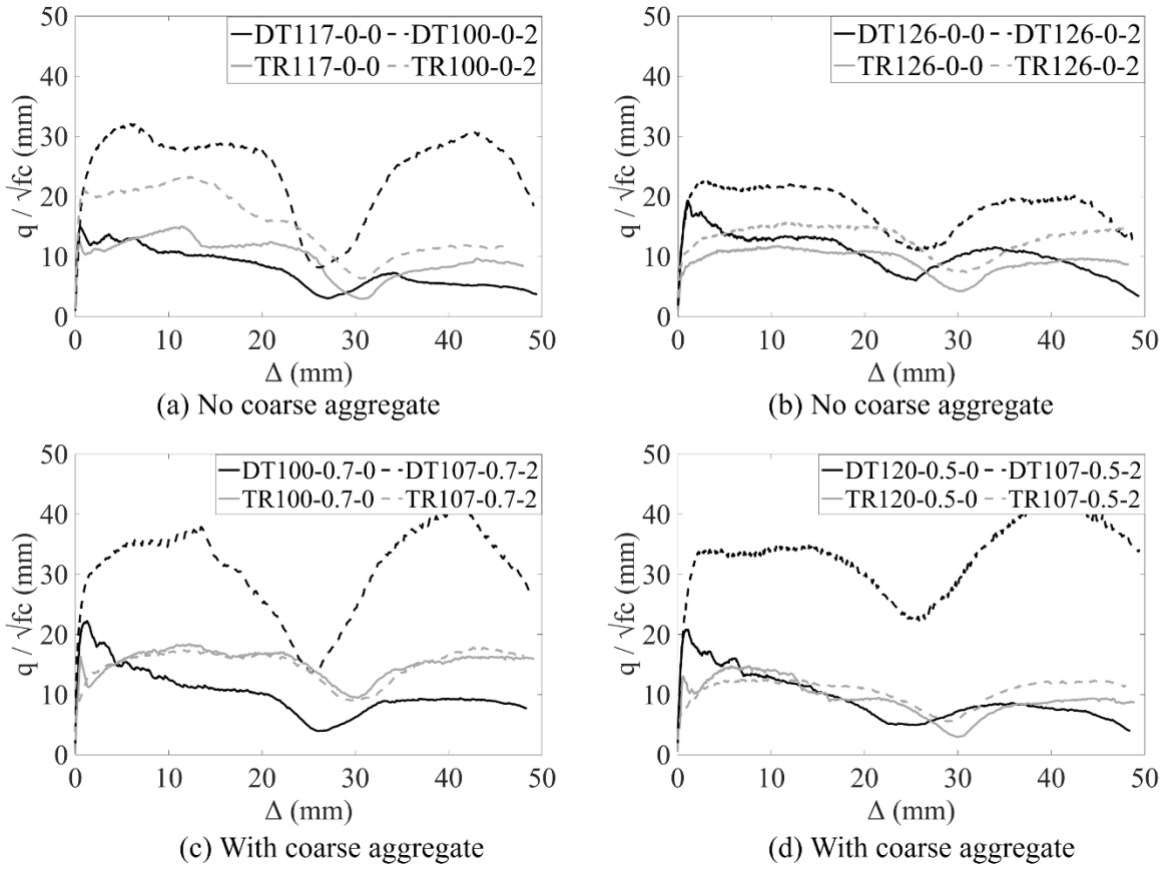


**Fig. 12.** Average $\frac{q}{\sqrt{f_c}}/\Delta$ response for specimens with identical w:b and CA contents but with variation in fibre content

In Figs. 12(a) and (b) for concretes without coarse aggregate, it can be seen that regardless of any reduction in concrete compressive strength that may occur due to the inclusion of fibres, there is a significant increase in the strength and ductility of the $q/\Delta$ relationship as a result of the fibre addition. This change is particularly significant for the DT sheet in which the $\frac{q}{\sqrt{f_c}}$ in Fig. 12(a), is seen to approximately double for the mix with fibres compared to the identical mix design without fibres. With this increase arising despite the concrete compressive strength dropping by 17 MPa. This change in behaviour is likely due to the increased confinement provided by the fibres following cracking of the concrete within the dovetail void. In comparison, while an increase in strength is observed for the tested TR profile it is not as significant as for the tested DT profile.

For the concretes containing coarse aggregate shown in Figs. 12(c) and (d), it can again be observed that the addition of fibres significantly improves the strength and ductility of the $\frac{q}{\sqrt{f_c}}/\Delta$ relationship for the DT profile, but no improvement is observed for the TR sheet and

this is likely because there is no mechanism for the fibres to provide addition confinement that impact the bonded interface.

## 5. Conclusion

The behaviour of steel concrete composite slabs at all load levels is controlled by the shear transfer between the profiled steel deck and concrete slab. To enable the design of composite slabs with UHPFRC, this paper seeks to quantify the effect of fibres, aggregate and concrete strength on the local $q/\Delta$ relationship for dovetailed and trapezoidal decks.

Specifically, it has been shown that the single-lap shear test commonly applied to quantify the bond between fibre reinforced polymers and concrete can be applied to quantify the bond between steel profile sheets and concrete. The results of trial testing have found that minimal difference between free-end and loaded-end slip occurs when the bonded length is reduced to 90 mm (approximately 3 embossments) in which case the average shear stress can be taken as the local shear flow corresponding to a specific slip $\Delta$.

Regarding the quantification of the $q/\Delta$ relationship for UHPC and UHPFRC:

(i) For the very-high and ultra-high strength concretes tested, the influence of concrete strength on the bond between the concrete and the tested profile deck is negligible.

(ii) The presence of fibres significantly improves the strength and ductility of the $q/\Delta$ response for the dovetailed sheets tested in this study. This improvement can be explained by increased confinement provided by the fibres.

(iii) For the trapezoidal sheet tested in this study, the presence of fibres does not significantly impact the interface strength but the ductility improves.

(iv) The addition of coarse aggregate does not significantly impact the $q/\Delta$ relationship for either deck type, and is observed to be beneficial in for mixes with no fibres. Consequently from the perspective of the interfacial bond properties, the addition of coarse aggregate is beneficial in reducing the cost and environmental impact of the concrete material.

## Authors statement

**Sirui Chen:** Investigation, Data processing, Writing – original draft

**Phillip Visintin:** Conceptualization, Methodology, Supervision, Writing- review

**Deric J. Oehlers:** Conceptualization, Supervision, Methodology, Writing – review

## Declaration of competing interest

The authors declare that they have no known competing financial interests or personal relationships that could have appeared to influence the work reported in this paper.


## Acknowledgements

This material is based upon work supported by the Australian Research Council Discovery Project 190102650. Sirui Chen was supported by an Australian Government Research Training Program Scholarship. The authors also wish to acknowledge the assistance of Mr Jon Ayoub who assisted in completing the lab testing.


## Principal nomenclature

$q$: Longitudinal shear flow

$\Delta$: Longitudinal slip

PSC: Partial shear connection method

$\eta$: Shear connection degree

$\tau$: Shear stress

$\sigma_N$: Normal stress

$\sigma_{lat}$: Additional confining stress

$A_s$: cross-sectional area of tested profiled deck ($mm^2$)

$b$: width of the bonded region (mm)

$d$: depth of tested profiled deck (mm)

$w$: width of tested profiled deck (mm)

F: applied load at end of steel deck

$F_{lat}$: Lateral resistance force

$L_b$: bonded length of profiled slab (mm)

$f_c$: Concrete compressive strength (MPa)

$E_c$: Young's modulus of concrete (MPa)

$q_{pk}$: ultimate shear flow

## References


[1] F.P. Ackermann, J. Schnell, Steel fibre reinforced continuous composite slabs, in: Composite Construction in Steel and Concrete VI, (2011) 125–137.

[2] X. Li, X. Zheng, M. Ashraf, H. Li, Experimental study on the longitudinal shear bond behavior of lightweight aggregate concrete – closed profiled steel sheeting composite slabs, Construct. Build. Mater. 156 (2017) 599–610.

[3] V. Marimuthu, S. Seetharaman, S. Arul Jayachandran, A. Chellappan, T. K. Bandyopadhyay, D. Dutta, Experimental studies on composite deck slabs to determine the shear-bond characteristic (*m–k*) values of the embossed profiled sheet, J. Constr. Steel Res. 63 (6) (2007) 791–803.

[4] K. Lambe, S. Siddh, Analysis and design of composite slab by varying different parameters, in: IOP Conference Series: Materials Science and Engineering, (330) (2018) 12115.

[5] O. Yi, J.E. Mills, Y. Zhuge, X. Ma, R.J. Gravina, O. Youssf, Performance of crumb rubber concrete composite-deck slabs in 4-point-bending, J. Build. Eng. (2021) 102695.

[6] R. S. Costa, A.C.C. Lavall, R.G.L. da Silva, H.F. Viana, F.C. Rodrigues, E.L. Andrade, New equations to establish the effective moment of inertia of composite slabs with profiled steel sheeting for deflection calculation, J. Build. Eng. (37) (2021) 102135.

[7] C. Shi, Z. Wu, J. Xiao, D. Wang, Z. Huang, Z. Fang, A review on ultra high performance concrete: Part I. Raw materials and mixture design, Construct. Build. Mater. (101) (2015) 741–751.

[8] J. R. Liew, Design Guide for Concrete Filled Tubular Members with High Strength Materials to Eurocode 4, Research publishing, (2015).

[9] V. Afroughsabet, L. Biolzi, T. Ozbakkaloglu, High-performance fiber-reinforced concrete: a review, J. Mater. Sci. 51 (14) (2016) 6517–6551.

[10] K.M.A. Hossain, S. Alam, M.S. Anwar, K.M.Y. Julkarnine, High performance composite slabs with profiled steel deck and Engineered Cementitious Composite strength and shear bond characteristics, Construct. Build. Mater. 125 (2016) 227–240.

[11] J. Qi, Z. Cheng, J. Wang, Y. Tang, Flexural behavior of steel-UHPFRC composite beams under negative moment, Structures 24 (2020) 640–649.

[12] A. Hamoda, K.M.A. Hossain, K. Sennah, M. Shoukry, Z. Mahmoud, Behaviour of composite high performance concrete slab on steel I-beams subjected to static hogging moment, Eng. Struct. 140 (2017) 51–65.

[13] A. Gholamhoseini, A. Khanlou, G. MacRae, A. Scott, S. Hicks, R. Leon, An experimental study on strength and serviceability of reinforced and steel fibre reinforced concrete (SFRC) continuous composite slabs, Eng. Struct. 114 (2016) 171–180.

[14] A. Gholamhoseini, A. Khanlou, G. Macrae, S. Hicks, A. Scott, G. Clifton, Short-term behaviour of reinforced and steel fibre–reinforced concrete composite slabs with steel decking under negative bending moment, Adv. Struct. Eng. 21 (2017), 136943321773971.

[15] H.-G. Kwak, Y.-J. Seo, Time-dependent behavior of composite beams with flexible connectors, Comput. Methods Appl. Mech. Eng. 191 (34) (2002) 3751–3772.

[16] J. Stark, J. Brekelmans, Plastic design of continuous composite slabs, J. Constr. Steel Res. 15 (1-2) (1990) 23–47.

[17] A. Gholamhoseini, Experimental and finite element study of ultimate strength of continuous composite concrete slabs with steel decking, Int. J. Adv. Struct. Eng. 10 (1) (2018) 85–97.

[18] P. Visintin, M.S. Mohamad Ali, T. Xie, A.B. Sturm, Experimental investigation of moment redistribution in ultra-high performance fibre reinforced concrete beams, Construct. Build. Mater. 166 (2018) 433–444.

[19] L. Huang, J. Xie, L. Li, B. Xu, P. Huang, Z. Lu, Compressive behaviour and modelling of CFRP confined ultra-high performance concrete under cyclic loads, Construct. Build. Mater. 310 (2021) 124949.

[20] S.-W. Yoo, J.F. Choo, Evaluation of the flexural behavior of composite beam with inverted-T steel girder and steel fiber reinforced ultra high performance concrete slab, Eng. Struct. (118) (2016) 1–15.

[21] Y. Zhang, S. Cai, Y. Zhu, L. Fan, X. Shao, Flexural responses of steel-UHPC composite beams under hogging moment, Eng. Struct. (206) (2020) 110134.

[22] X. Liu, J. Zhang, Z. Cheng, M. Ye, Experimental and numerical studies on the negative flexural behavior of steel-UHPC composite beams, Adv. Civ. Eng. (2021) 1–15.

[23] F. Abas, R. Gilbert, S. Foster, M. Bradford, Strength and serviceability of continuous composite slabs with deep trapezoidal steel decking and steel fibre reinforced concrete, Eng. Struct. (49) (2013) 866–875.

[24] N. N. Sarbini, I. S. Ibrahim, A. A. Saim, A.B. Abdul Rahman, N. F. Harun, N. N. Hasbullah, Shear capacity of composite slab reinforced with steel fibre to that offabric reinforcement in concrete topping, Mater. Res. Innovat. 18 (sup6) (2014). S6-236-S6-240.

[25] M. Bradford, B. Uy, Shear-Bond Behaviour of Steel-Fibre Reinforced Concrete (SFRC) Composite Slabs with Deep Trapezoidal Decking: Experimental Study, American Society of Civil Engineers (ASCE), (2016) 561–580.

[26] X. Li, X. Zheng, M. Ashraf, H. Li, The longitudinal shear bond behavior of an innovative laminated fiber reinforced composite slab, Construct. Build. Mater. 215 (2019) 508–522.

[27] D. K. Aarthi, E. Jeyshankaran, N. Aranganathan, Comparative study on longitudinal shear resistance of light weight concrete composite slabs with profiled sheets, Eng. Struct. (200) (2019) 109738.

[28] Y.-C. Kan, L. H. Chen, T. Yen, Mechanical behavior of lightweight concrete steel deck, Construct. Build. Mater. (42) (2013) 78–86.

[29] K. M. A. Sohel, J. Y. R. Liew, A. I. Fares, Shear bond behavior of composite slabs with ultra-lightweight cementitious composite, J. Build. Eng. (44) (2021) 103284.

[30] C. Wang, C. Yang, F. Liu, C. Wan, X. Pu, Preparation of ultra-high performance concrete with common technology and materials, Cement Concr. Compos. 34 (4) (2012) 538–544.

[31] J. Ma, M. Orgass, F. Dehn, D. Schmidt, N. Tue, Comparative investigations on ultra-high performance concrete with and without coarse aggregates, in: International Symposium on Ultra High Performance Concrete, Kassel, Germany, (2004) 205–212.

[32] P. P. Li, Y. Y. Y. Cao, M. J. C. Sluijsmans, H. J. H. Brouwers, Q. Yu, Synergistic effect of steel fibres and coarse aggregates on impact properties of ultra-high performance fibre reinforced concrete, Cement Concr. Compos. 115 (2021) 103866.

[33] L. Xu, F. Wu, Y. Chi, P. Cheng, Y. Zeng, Q. Chen, Effects of coarse aggregate and steel fibre contents on mechanical properties of high performance concrete, Construct. Build. Mater. (206) (2019) 97–110.

[34] F. Wu, L. Xu, Y. Chi, Y. Zeng, F. Deng, Q. Chen, Compressive and flexural properties of ultra-high performance fiber-reinforced cementitious composite: the effect of coarse aggregate, Compos. Struct. (236) (2020) 111810.

[35] J. Yu, B. Zhang, W. Chen, J. He, Experimental and multi-scale numerical investigation of ultra-high performance fiber reinforced concrete (UHPFRC) with different coarse aggregate content and fiber volume fraction, Construct. Build. Mater. (260) (2020) 120444.

[36] R.P. Johnson, D. Anderson, EN1994 Eurocode 4: design of composite steel and concrete structures, Proc. Inst. Civ. Eng. - Civ. Eng. (144) (6) (2001) 33–38.

[37] L. An, K. Cederwall, Composite Slabs Analyzed by Block Bending Test, (1992).

[38] B. Daniels, M. Crisinel, Ccomposite slab behavior and strength analysis .1. calculation procedure, J. Struct. Eng.-ASCE (119) (1) (1993) 16–35.

[39] M. J. Burnet, D.J. Oehlers, Rib shear connectors in composite profiled slabs, J. Constr. Steel Res. 57 (12) (2001) 1267–1287.

[40] C. K. Jolly, A. Zubair, The efficiency of shear-bond interlock between profiled steel sheeting and concrete, Compos. Steel Struct. Adv. Design Construct. (1987) 127–136.

[41] R. Tremlay, P. Gignac, G. Degrange, C.A. Rogers, Variables Affecting the Shear-Bond Resistance of Composite Floor Deck Systems, (2002).

[42] E. Airumyan, V. Belyaev, I. Rumyancev, Efficient embossment for corrugated steel sheeting, in: IABSE Symposium on Mixed Structures Including New Materials, (1990) 137–142.

[43] M. Patrick, K. Poh, Controlled test for composite slab design parameters, in: IABSE Symposium, Brussels, Belgium-Mixed Structures, (1990), 227–231. Including New Materials.

[44] M. Porter, C. Ekberg Jr., Investigation of Cold-Formed Steel-Deck-Reinforced Concrete Floor Slabs, (1971).

[45] H. Cifuentes, F. Medina, Experimental study on shear bond behavior of composite slabs according to Eurocode 4, J. Constr. Steel Res. (82) (2013) 99–110.

[46] M. Crisinel, F. Marimon, A new simplified method for the design of composite slabs, J. Constr. Steel Res. 60 (3-5) (2004) 481–491.

[47] R. Abdullah, A. Kueh, I. Ibrahim, W. Easterling, Characterization of shear bond stress for design of composite slabs using an improved partial shear connection method, J. Civ. Eng. Manag. 21 (2015) 720–732.

[48] R. Johnson, A. Shepherd, Resistance to longitudinal shear of composite slabs with longitudinal reinforcement, J. Constr. Steel Res. 82 (2013) 190–194.

[49] O. Yi, Y. Zhuge, X. Ma, R.J. Gravina, J.E. Mills, O. Youssf, Push-off and pull-out bond behaviour of CRC composite slabs – an experimental investigation, Eng. Struct. 228 (2021) 111480.

[50] D. Waldmann, A. May, V.B. Thapa, Influence of the sheet profile design on the composite action of slabs made of lightweight woodchip concrete, Construct. Build. Mater. 148 (2017) 887–899.

[51] D.J. Oehlers, M.A. Bradford, Composite Steel and Concrete Structural Members : Fundamental Behaviour, first ed., Pergamon, New York, (1995).

[52] J. Holomek, M. Bajer, J. Barnat, P. Schmid, Design of composite slabs with prepressed embossments using small-scale tests, Struct. Concr. 16 (1) (2015) 137–148.

[53] M.M. Rana, B. Uy, O. Mirza, A push test study on the behavior of post-tensioned composite steel-concrete slabs, in: Composite Construction in Steel and Concrete VII. (2016) 779–790.

[54] J. Vaculik, P. Visintin, N.G. Burton, M. Griffith, R. Seracino, State-of-the-art review and future research directions for FRP-to-masonry bond research: test methods and techniques for extraction of bond-slip behaviour, Construct. Build. Mater. 183 (2018) 325–345.

[55] M. Petkevi˘cius, J. Valivonis, Analysis of Bending Capacity of Composite Steel-Concrete Slabs with Steel Fiber Reinforced Concrete, (2010).

[56] J. Holomek, M. Bajer, J. Barnat, M. Vild, Composite slabs with prepressed embossments – longitudinal shear resistance, Appl. Mech. Mater. 769 (2015) 289–293.

[57] M. Haskett, D. Oehlers, M. Ali, Local and global bond characteristics of steel reinforcing bars, Eng. Struct. 30 (2008) 376–383.

[58] S.H. Chu, A. Kwan, A new method for pull out test of reinforcing bars in plain and fibre reinforced concrete, Eng. Struct. 164 (2018) 82–91.

[59] S.A. Hadigheh, R.J. Gravina, S. Setunge, Identification of the interfacial fracture mechanism in the FRP laminated substrates using a modified single lap shear test set-up, Eng. Fract. Mech. 134 (2014).

[60] M.H. Sobuz, P. Visintin, M. Ali, M. Singh, M. Griffith, A. Sheikh, Manufacturing ultra-high performance concrete utilising conventional materials and production methods, Construct. Build. Mater. 111 (2016) 251–261.

[61] Standard Australia, General Purpose and Blended Cements, AS/NZS 3972, Sydney, Australia, (2010).

[62] Standard Australia, Supplementary Cementitious Materials, Part 3: Amorphous Silica, (2016). AS/NZS 3582.3:2016, Sydney, Australia.

[63] Standard Australia, Metallic Materials - Tensile Testing - Method of Test at Room Temperature, (2020). AS 1391:2020, Sydney, Australia.

**Supplementary Material A**

Appendix A: DT-0F (Black solid line -1; Dark grey solid line – 2; Grey broken line – 3)


DT117-0-0F-1

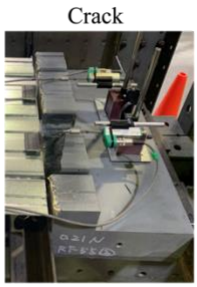


DT117-0-0F-2

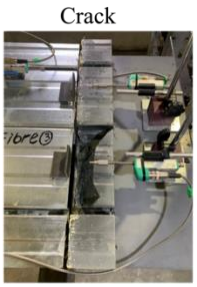


DT117-0-0F-3

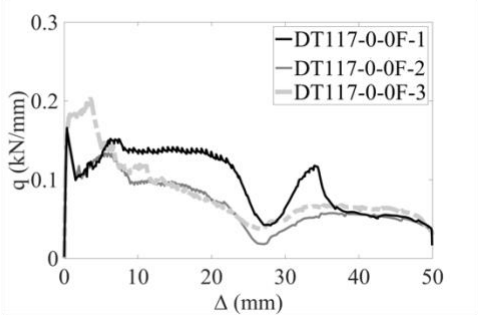


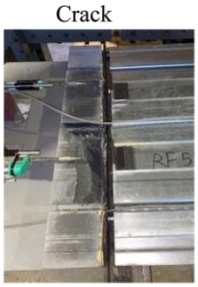


DT126-0-0F-1

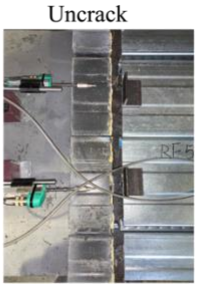


DT126-0-0F-2


DT126-0-0F-3

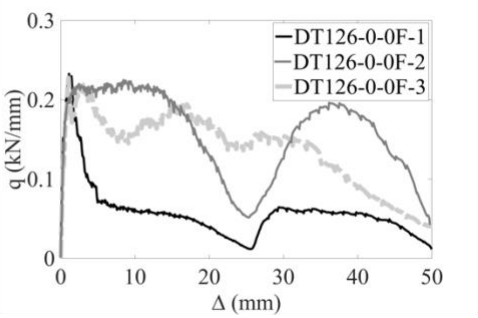


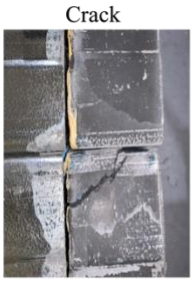


DT100-0.7-0F-1

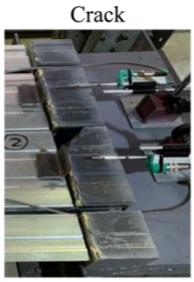


DT100-0.7-0F-2

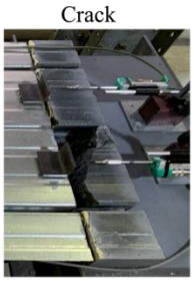


DT100-0.7-0F-3

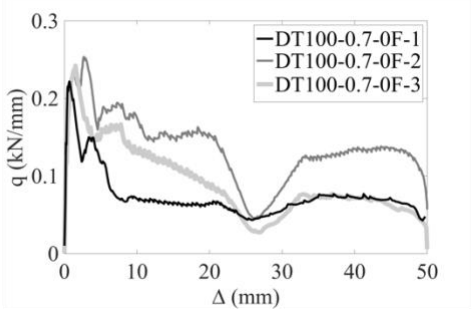



DT120-0.5-0F-1

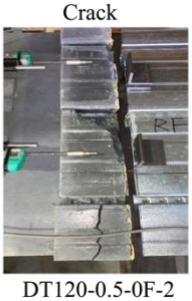


DT120-0.5-0F-2


DT120-0.5-0F-3

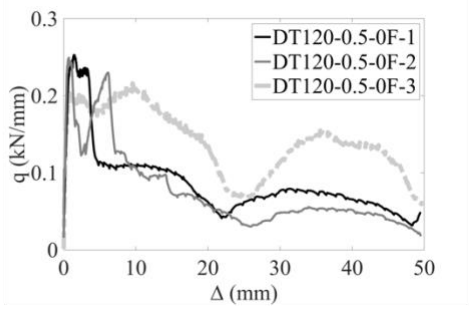

Appendix B: TR-0F

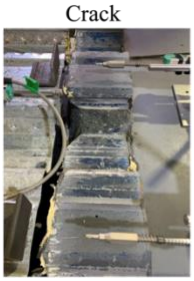

TR117-0-0F-1

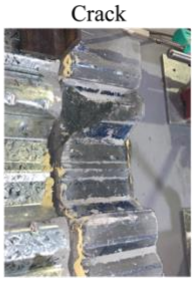

TR117-0-0F-2

TR117-0-0F-3

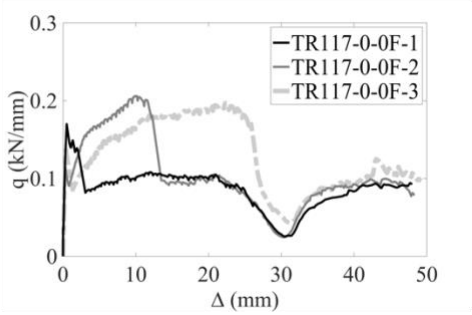


TR126-0-0F-1

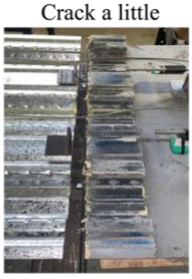

TR126-0-0F-2

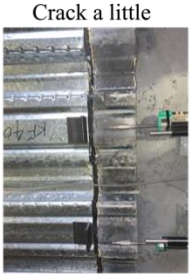

TR126-0-0F-3

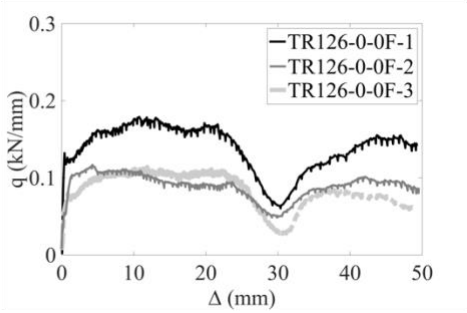


TR100-0.7-0F-1

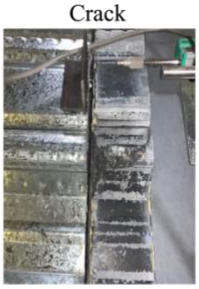

TR100-0.7-0F-2

TR100-0.7-0F-3

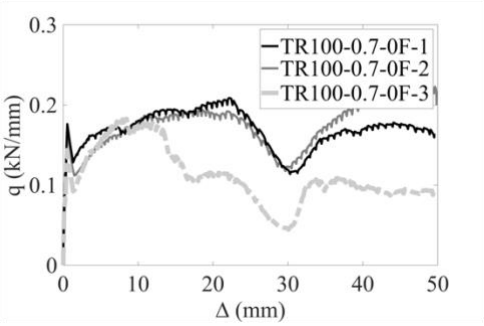


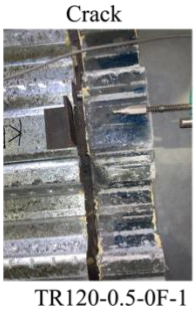

TR120-0.5-0F-1

TR120-0.5-0F-2

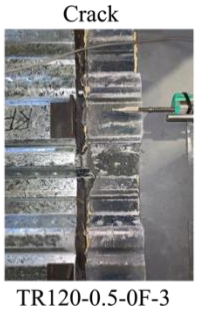

TR120-0.5-0F-3

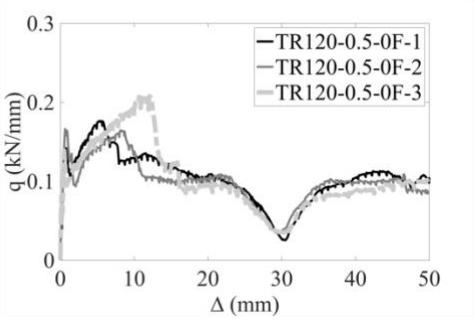

Appendix C: DT-2F

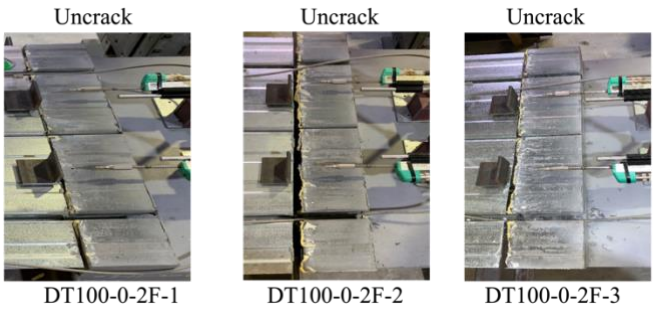


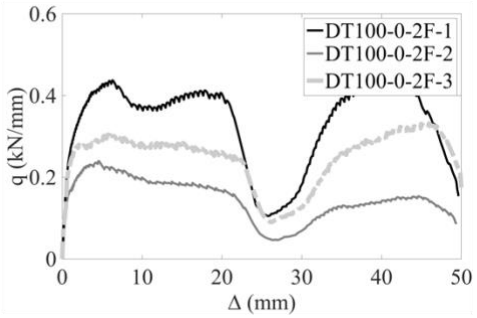


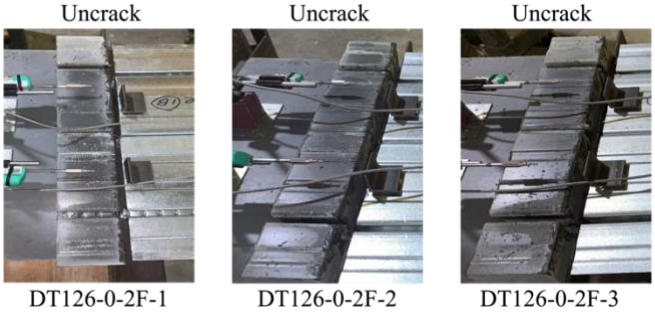


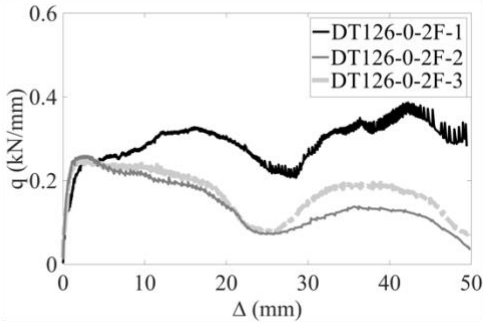


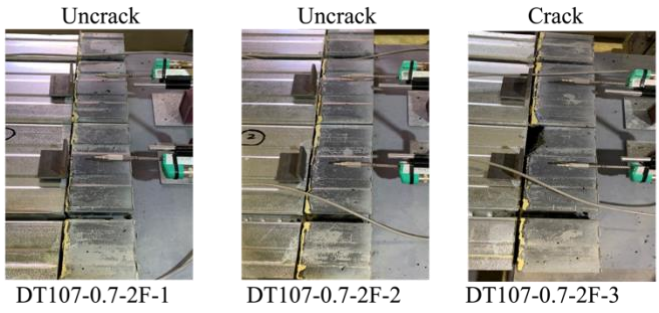


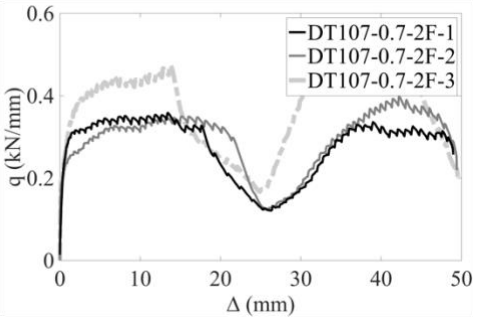


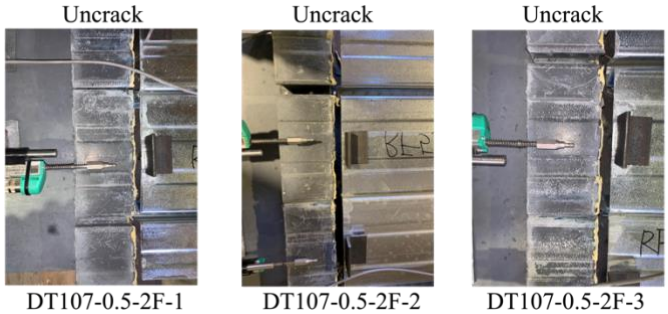


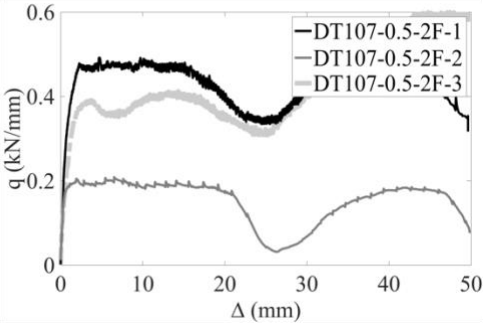

Appendix D: TR-2F

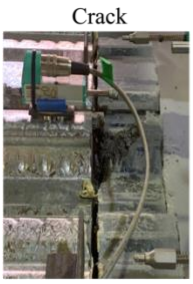


TR100-0-2F-1

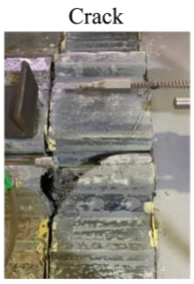


TR100-0-2F-2


TR100-0-2F-3

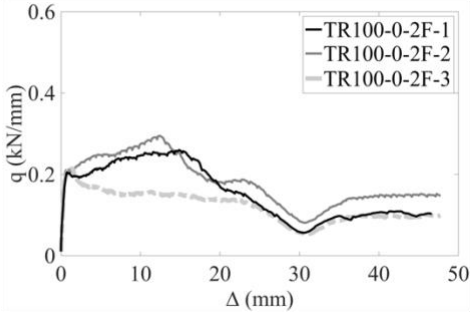


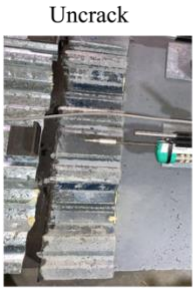


TR126-0-2F-1

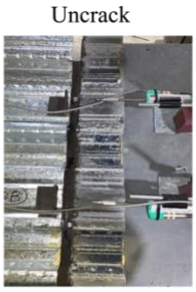


TR126-0-2F-2

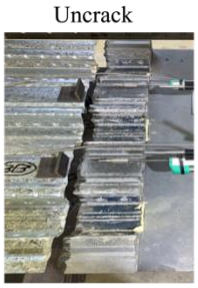


TR126-0-2F-3

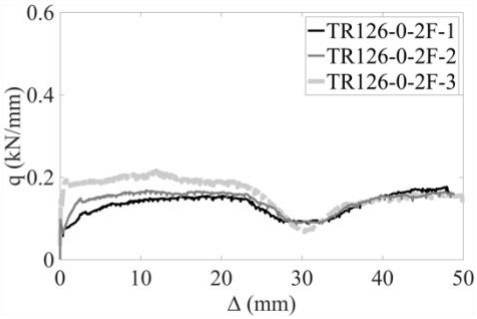


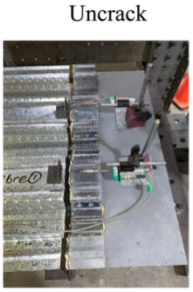


TR107-0.7-2F-1


TR107-0.7-2F-2

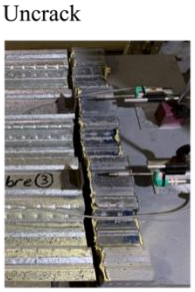


TR107-0.7-2F-3

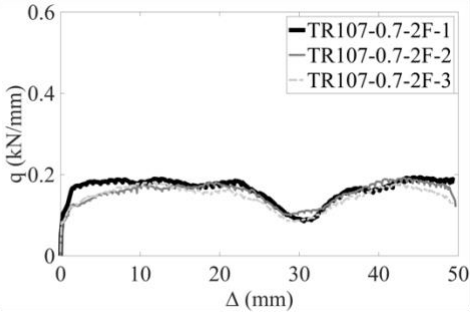


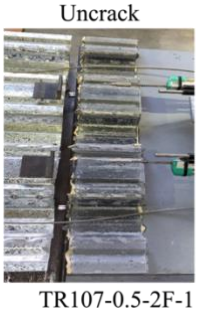


TR107-0.5-2F-1

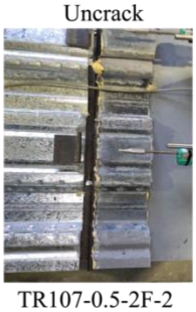


TR107-0.5-2F-2


TR107-0.5-2F-3

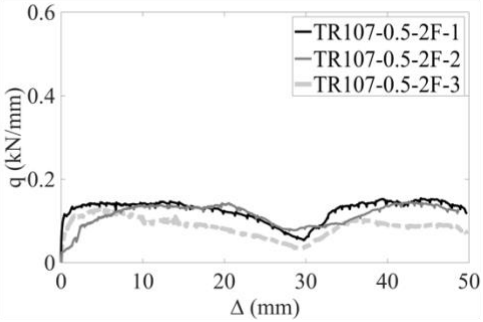

## CHAPTER 3 – Experimental Study

### Introduction

The publication titled “Experimental investigation of the influence of fibre content on the flexural performance of simply supported and continuous steel/UHPC concrete slabs” presents an experimental study to access the effectiveness of applying UHPFRC with varying fibre contents (0%, 1% and 2%) with dove-tailed profiled steel deck. These tests are used to examine the behaviour of simply supported and continuous slabs. This study aims to provide insights into the flexural performance of UHPFRC composite profiled slabs under different loading conditions and varying fibre contents.

In this study, six simply supported beams are subjected to sagging and hogging loading configurations to analyse the impact of fibre contents where the performance of composites is evaluated from load-deflection, load-slip, cracking spacing and cracking width results which are recorded throughout the whole tests.

In addition, three two-span continuous slab tests are used to investigate moment redistribution with the same cross-section designs for sagging and hogging regions as simply supported tests. Both simply supported and continuous slab tests are aimed for quantify behaviour of UHPFRC composite profiled slabs in both serviceability and ultimate limit states.

**Statement of Authorship**

# Statement of Authorship

| | |
|---|---|
| Title of Paper | Experimental investigation of the influence of fibre content on the flexural performance of simply supported and continuous steel/UHPC concrete slabs |
| Publication Status | ☐ Published ☐ Accepted for Publication<br>☑ Submitted for Publication ☐ Unpublished and Unsubmitted work written in manuscript style |
| Publication Details | Chen, S., Visintin, P. and Oehlers, D. J. (2023) 'Experimental investigation of the influence of fibre content on the flexural performance of simply supported and continuous steel/UHPC concrete slabs', submitted on steel composite structures |

## Principal Author

| | | | |
|---|---|---|---|
| Name of Principal Author (Candidate) | | | |
| Contribution to the Paper | Investigation, data processing, experimental texts, writing - original draft | | |
| Overall percentage (%) | 90% | | |
| Certification: | This paper reports on original research I conducted during the period of my Higher Degree by Research candidature and is not subject to any obligations or contractual agreements with a third party that would constrain its inclusion in this thesis. I am the primary author of this paper. | | |
| Signature | | Date | 14/08/2023 |

## Co-Author Contributions

By signing the Statement of Authorship, each author certifies that:

i. the candidate's stated contribution to the publication is accurate (as detailed above);

ii. permission is granted for the candidate in include the publication in the thesis; and

iii. the sum of all co-author contributions is equal to 100% less the candidate's stated contribution.

| | | | |
|---|---|---|---|
| Name of Co-Author | Phillip Visintin | | |
| Contribution to the Paper | Conceptualization, methodology, supervision, writing -review | | |
| Signature | | Date | 14/08/2023 |

| | | | |
|---|---|---|---|
| Name of Co-Author | Deric John Oehlers | | |
| Contribution to the Paper | Conceptualization, supervision, writing -review | | |
| Signature | | Date | 14/08/2023 |

Please cut and paste additional co-author panels here as required.

# Experimental investigation of the influence of fibre content on the flexural performance of simply supported and continuous steel/UHPC concrete slabs

Chen, S.[1], Visintin, P.[2], Oehlers, D.J.[3]

[1]Ph. D. candidate, School of Civil, Environmental and Mining Engineering, Univ. of Adelaide, Adelaide, SA 5005, Australia.

[2]Associate professor, School of Civil, Environmental and Mining Engineering, Univ. of Adelaide, Adelaide, SA 5005, Australia. (Corresponding author). ORCID: http://orcid.org/0000-0002-4544-2043. Email: Phillip.visintin@adelaide.edu.au

[3]Emeritus professor, School of Civil, Environmental and Mining Engineering, Univ. of Adelaide, Adelaide, SA 5005, Australia.

## Abstract

The application of relatively low volumes of fibres in normal strength concrete has been shown to be of significant benefit when applied to composite slabs with profiled sheet decking. This paper reports on an experimental study aimed at quantifying further potential benefits that may arise from applying ultra-high performance fibre reinforced concrete. To assess performance six simply supported beams were tested under hogging and sagging loading configurations along with three two span continuous beams. Fibre contents are varied from 0% to 2% and changes in strength, deformation, crack width and moment redistribution are measured. At the serviceability limit state, it is shown that the addition of high fibre volumes can significantly enhance member stiffness and reduce crack widths in all beams. At the ultimate limit state it is observed that a transition from 0% to 1% fibres significantly increases strength but that there is a maximum fibre volume beyond which no further increases in strength are possible. Conversely, member ductility and moment redistribution are shown to be strongly proportional to fibre volume.

**Keywords**

Composite profile slab; UHPFRC; crack width; flexural strength; moment redistribution

## 1. Introduction

Steel concrete composite construction is commonly applied in situations where high strength, stiffness and ductility is required. In composite structures it is common to construct slabs using a profiled steel deck over which a lightly reinforced concrete slab is placed. This form of construction is popular because the profile deck can be used as both formwork and part of the structural reinforcing of the slab, leading to reduced member depths. The use of profiled steel decking can therefore increase construction speed, reduce self-weight, and improve member performance [1-6].

The potential to further improve the performance of steel-concrete composite slabs through the use of fibre reinforced concrete has attracted recent research attention [7-10], the use of low volumes of fibres in normal strength concrete have been shown to increase member stiffness, reduce member deflection, reduce crack widths, and improve performance in the hogging region, which is prone to the formation of large cracks [11, 12]. Although the use of low volumes of fibres in normal strength concrete has been studied, the application of ultra-high performance fibre reinforced concrete (UHPFRC) has not yet been considered, because the design of composite slabs is generally not dependent on high concrete strengths. UHPFRC does however have several advantages that may be highly beneficial for composite slabs including:

1. The significant post-cracking tensile strength of UHPFRC may lead to significant increases in member flexural rigidities and reductions in crack-widths when subjected to both short-term and sustained loads. It is therefore possible that the application of UHPFRC may further reduce member depth which would lead to significant savings from both an environmental and financial perspective [13-15].
2. The application of UHPFRC in hogging regions may allow for a proportion of conventional steel reinforcement to be replaced by fibre reinforcement while maintaining acceptable member capacity and crack-width [9, 10]. The ability to replace conventional reinforcement with fibre reinforcement may lead to further simplifications in composite construction.

3. The compressive and tensile material ductility of UHPFRC, may lead to significant moment redistribution, allowing for reductions in member depth and reinforcement ratios when considering ultimate limit state design [8, 10, 16-19].

Studies focusing on the application of fibre reinforced concrete or UHPFRC to composite construction, and in particular the performance of composite slabs is limited. For example, Qi et al. conducted an experimental study of the performance of hogging beams constructed from normal strength (49 MPa) concrete and UHPFRC (125 MPa) [15]. The results showed that the application of UHPFRC increased the load to cause cracking by up to 70%, increased post-cracking member stiffness and reduced member crack widths. Similar findings were observed by Lin et al. who also studied beam hogging regions constructed from normal strength concrete (52 MPa) and UHPFRC (135 MPa) [20]. Yoo and Choo performed a study to evaluate the performance of inverted-T girders constructed with UHPFRC and found that application of UHPFRC could significantly increase member ductility, and also limit the slip of shear connectors which was observed to be beneficial at the serviceability limit state [21]. Zhang et al. tested the hogging region of composite beams with UHPFRC slabs, with the results showing that only the application of UHPFRC limited the formation of macro-cracks and this could be beneficial for member durability [22].

When considering normal and high strength concretes, Hamoda et al. tested hogging regions constructed from either normal-strength (32 MPa) and high-strength (68 MPa) concrete with steel fibres and found that the load to cause cracking increased by approximately 50% and the load to cause reinforcement yielding increased by 72% [13]. Lin, Yoda and Taniguchi studied composite beam with normal strength concrete (36MPa) and SFRC (38.7MPa) [23]. The results showed that the addition of fibre reinforcement limited crack propagation and reduced the number of macro-cracks along the span but increased the number of micro-cracks.

When specifically considering composite profile deck slabs, recent research has mainly focused on studying the performance of composite slabs with high-strength concrete [24-27], lightweight-concrete [5, 28-32] or crumb rubber concrete [33-35], with few studies considering fibre reinforced concrete. For example, Abas et al. studied the behaviour of trapezoidal profiled deck continuous composite slabs with fibre contents ranging from 0 to 40 $kg/m^3$ [7]. It was observed that the addition of fibres is beneficial, leading to increased ultimate load capacity, flexural deformation capacity and longitudinal shear capacity. For example, a fibre content of 20 $kg/m^3$ was found to improve the load at which slip of the profile sheet first occurred by 59%

and the peak load by 34% respectively compared to specimens without fibre. It was also suggested that the addition of 30 kg/m$^3$ of fibres was sufficient to provide crack control.

Gholamhoseini et al. drew a similar conclusions by testing slabs with fibre contents of between 20 kg/m$^3$ to 60 kg/m$^3$, and suggested that higher fibre contents did not lead to higher ultimate load capacity [10]. It was further found that with fibre contents of 60 kg/m$^3$, the slabs had narrower cracks then in mesh-reinforced control specimen.

Ackermann and Schnell tested simply supported and continuous slabs with normal strength fibre reinforced concrete to investigate the load-bearing behaviour and rotational capacity in the hogging region [8]. It was found that the inclusion of fibres enabled significant improvements in the rotation capacity and that this could simplify slab detailing by allowing for high levels of moment redistribution.

The above literature review indicates that although there have been studies that investigate the performance of steel UHPFRC concrete beams, to date there is a lack of studies that investigate the behaviour of profile steel deck slabs. This is important, because the findings from previous studies on beams indicate that there is likely to be a significant benefit from the application of UHPFRC in slabs due to increased strength, stiffness, crack control and moment redistribution. To more fully assess the potential for UHPFRC composite slabs, in this paper an experimental study is undertaken to assess the performance of simply supported and continuous members manufactured from ultra-high performance concrete with either 0%, 1% or 2% fibres.

## 2. Experimental Program

To enable a detailed assessment of the behaviour of UHPC composite profile slabs at both the serviceability and ultimate limit state, an experimental campaign covering concrete with and without fibres (0, 1% and 2% fibres by volume), and using a dovetailed profile to construct both simply supported and two-span continuous slabs was developed. In addition to the slab tests, associated material tests were conducted to quantify the material properties required to undertake detailed analyses in future studies.

For each concrete type (0%, 1% and 2% fibres) simply supported beams with typical cross-sections representing the sagging and hogging regions of a continuous member were constructed according to Table 1. Both the sagging and hogging members (Fig. 1) had an overall depth of 100 mm, a width of 590 mm, a total span of 2485 mm and were tested over

the central 2385 mm. These dimensions of the specimens were governed by the dimensions of the dovetailed sheet, which has a total width of 595 mm, a depth of 54 mm, a sheet thickness of 1 mm and a total cross-sectional area of 990 $mm^2$. That is, to construct the simply supported beams the sheet was cut transversely to allow two beams to be manufactured from a single sheet, and longitudinally to allow the clip connection to be located in the centre of the slab.

The sagging beam was reinforced with 2 10 mm ribbed steel bars located 47 mm from the bottom of the slab, this longitudinal reinforcement was supported at the ends by two 10 mm transverse bars which spanned between the dovetails of the profile (Fig. 1(a) and (c)) where red dots indicate location of instrumentation.

The hogging test specimens shown in Fig. 1(b) and (d) were manufactured so that testing could be undertaken with the profile sheet located at the top (compression) face. The beams were reinforced with 5 10 mm reinforcing acting as the tensile reinforcement (0.68 %) with a cover to the centre of the reinforcement of 20 mm. In the compression region, the section was reinforced with 2 10 mm bars in an identical location to those of the sagging cross-section. This approach was taken so that the simply supported hogging test specimen could be taken to represent the hogging region of a continuous beam with continuous tensile reinforcement.

**Table 1**

Designation of tested slab

| Designation | Slab type | Fibre content | Test type | Tensile reinforcement ratio | Profile sheet reinforcement ratio | Compression reinforcement ratio |
|---|---|---|---|---|---|---|
| SS0-S | Simply supported slab | 0% | Sagging test | 0.27% | 1.72% | - |
| SS0-H | | 0% | Hogging test | 0.68% | 1.72% | 0.27% |
| SS1-S | | 1% | Sagging test | 0.27% | 1.72% | - |
| SS1-H | | 1% | Hogging test | 0.68% | 1.72% | 0.27% |

| | | | | | | |
|---|---|---|---|---|---|---|
| SS2-S | | 2% | Sagging test | 0.27% | 1.72% | - |
| SS2-H | | 2% | Hogging test | 0.68% | 1.72% | 0.27% |
| C0 | Continuous slab | 0% | Sagging section | 0.27% | 1.72% | - |
| | | | Hogging section | 0.68% | 1.72% | 0.27% |
| C1 | | 1% | Sagging section | 0.27% | 1.72% | - |
| | | | Hogging section | 0.68% | 1.72% | 0.27% |
| C2 | | 2% | Sagging section | 0.27% | 1.72% | - |
| | | | Hogging section | 0.68% | 1.72% | 0.27% |

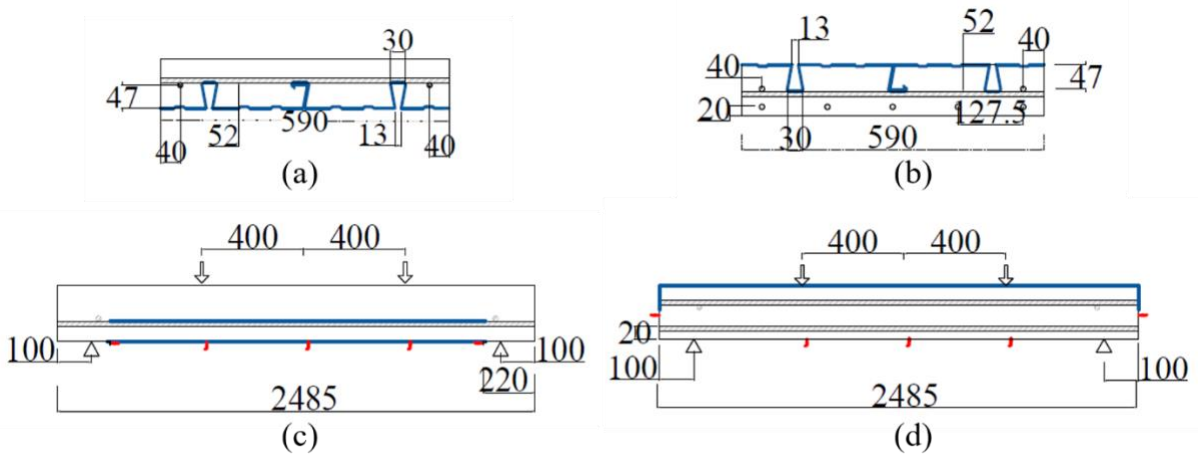


**Fig. 1.** Cross-section of: (a) sagging, (b) hogging and elevation view of: (c) sagging (d) hogging test specimen.

The continuous test specimens shown in Fig. 2, have a total span of 4970 mm and a central support giving two spans (support to support) of 2435 mm. As shown in Fig. 2, the continuous beam is constructed using the hogging cross section shown in Fig. 1(d) over the central 1460

mm and the sagging cross section throughout the remainder of the span and the tensile reinforcement of the sagging cross-section is continuous over both spans.

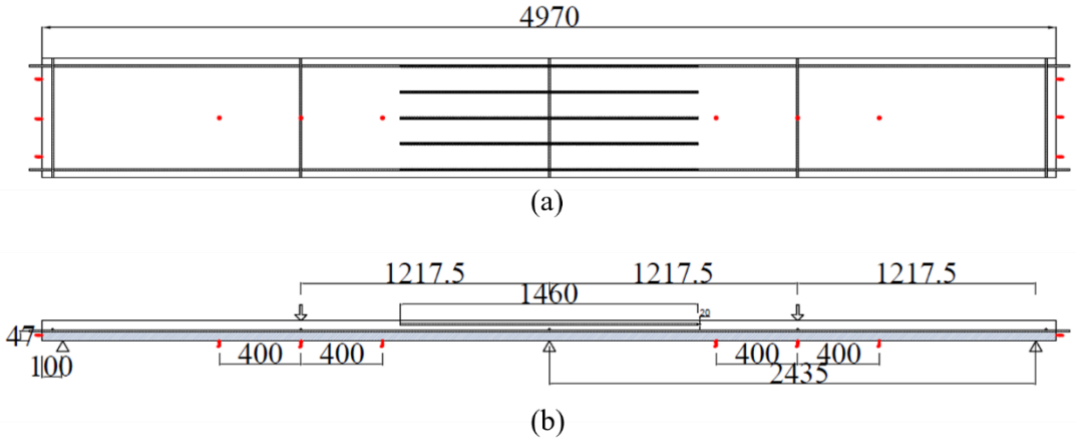


**Fig. 2.** Continuous slab test: (a) plan, (b) elevation view.

### *2.1 Beam test procedure and instrumentation*

The test setup for the sagging, hogging and continuous beam is shown in Fig. 3. The simply supported beams were tested under 4-point bending over a span of 2385 mm and with an 800 mm constant moment region.

During testing of the simply supported members, a load was applied to the central hydraulic ram using a hand operated jack at a rate of approximately 4 mm/min until the ultimate strength was reached after which the load rate was increased to 12 mm/min. During loading of the simply supported members, loading was stopped beginning at 15 kN of applied load to measure the location and width of all cracks in the constant moment region at the level of the tensile reinforcement (47 mm from the tensile face for the sagging beam, and 20 mm from the tensile face for the hogging beam). The crack spacing was measured using a steel ruler and the crack width was measured using a handheld microscope with a magnification of 1:220. Crack width measurements were taken at 15 kN load intervals until approximately the load at which the tensile reinforcement could be expected to yield.

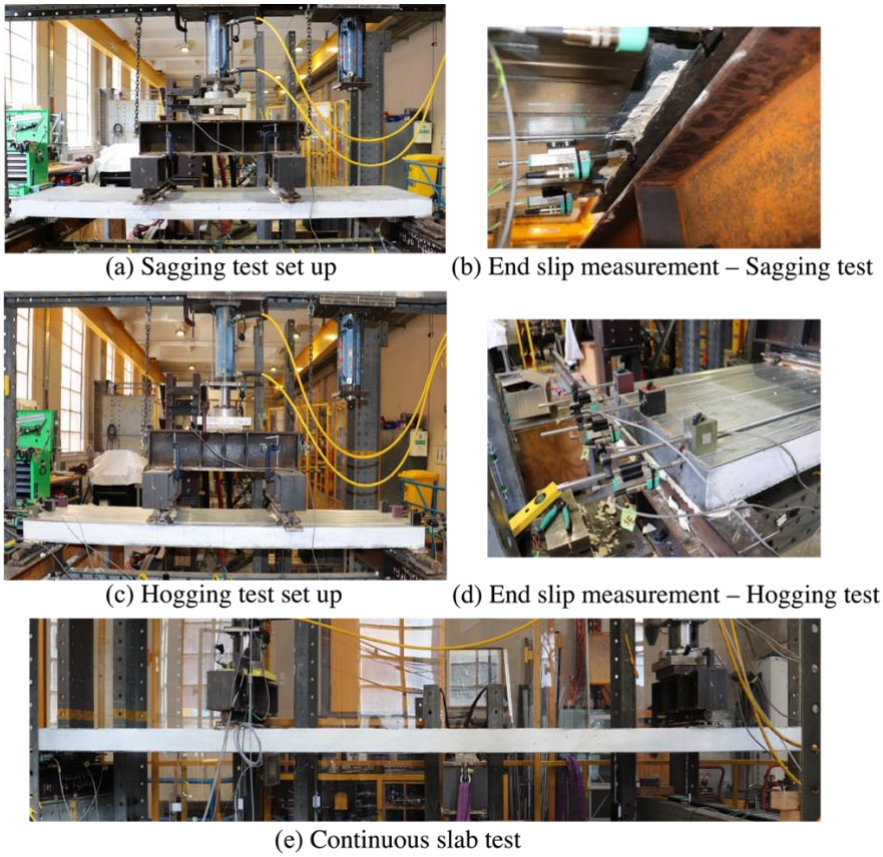


**Fig. 3.** Experimental test loading configuration

Throughout loading, the deflection was measured at the mid-span and beneath each of the loading points by 150 mm LVDTs. The slip of the profile sheet relative to the reinforced concrete cross-section was measured using 3 50 mm LVDTs spaced equally at each end of the slab (Figs. 3(b) and (d)). For the simply supported beams, after casting, the profile sheet was cut 220 mm from the end of the slab to prevent the sheet being trapped by the support and the slip of the sheet was measured 130mm from the end of the slab.

For the continuous slabs, the loads were applied by independent hydraulic rams at the mid-point of each span using two independent hydraulic jacks (Fig. 3(e)). The load was measured using load cells attached to each of the loading rams and beneath the central pin support, such that the loads at the two end supports could be determined from simple statics. The deflection under each loading point was measured using a 150 mm LVDT. Throughout testing, the load was applied at about 4 mm/min through whole process of tests. No crack width measurements were taken for the continuous beam tests.

### *2.2 Material test specimens*

To facilitate the future validation of analytical approaches, a series of material tests were conducted to obtain the material properties of the concrete and the reinforcement. Additional testing performed as part of a larger experimental campaign also allows for quantification of the shear flow slip relationship between the profile sheet and the concrete [36] and the bond between the reinforcement and the concrete [37].

The compressive stress/strain relationship of concrete was tested using cylinders with a diameter of 100 mm and a total length of 200 mm. For testing, the ends of the cylinders were ground smooth and the specimens were loaded under uniaxial compression at a rate of 4 kN/min. During testing, the axial strain was measured using 2 30 mm stain gauges located at the mid-height on opposite sides of the specimen, the platen-to-platen deformation was further measured using 2 24 mm LVDTs. Tests to quantify the compressive stress strain behaviour of the concrete were undertaken on 3 specimens from each fibre volume fraction (i.e. 0%, 1%, and 2% fibres) that were determined from AS 1012.9:2000 [38] and AS 1012.17:1997 [39].

To quantify the tensile behaviour of the concrete, direct tensile tests were undertaken on dogbone shaped specimens with a central test region length of 300 mm and a test cross-section of 120 mm x 120 mm. This design has been extensively utilised in other companion papers which can be referred to for further details [18, 40]. During testing, the specimens were loaded in uniaxial tension at a rate 0.005 mm/min before crack localisation and then applied a rate of 4.5 mm/min until the end of the test. The total deformation over the central test region was measured using 2 4 mm LVDTs located on the front and back face of the specimen. Three replicate tests were conducted for each fibre volume fraction.

Concrete shrinkage strains were measured using 3 prisms with a cross section of 75 mm x 75 mm and a total length of 285 mm according to AS 1012.13:2015 [41]. The zero-time at which the first specimen length reading was taken at the time of demoulding and the average shrinkage strain was calculated at the time of slab testing using three replicate specimens for each concrete type.

The tensile stress/strain relationship of the 10 mm reinforcing bars was determined in accordance with AS/NZS 4671:2019 [42], in which a bar was loaded at a rate of 12 kN/min until failure. During loading, the extension of the reinforcement was measured using an extensometer with a gauge length of 80 mm. Similarly, the stress/strain relationship of the profile sheet was measured in accordance with AS 1391 [43], on a dogbone shaped specimen cut from the profile sheet and having shank dimensions of 120 mm x 20 mm x 1 mm (length x

width x thickness). During testing, the dogbone was loaded at a rate of 12 kN/min and the deformation of the shank was measured using an extensometer with an 80 mm gauge length. The average stress/strain relationships of the reinforcing bar and profile sheet were determined from three test replicates.

### *2.3 Concrete mix design and batching*

The UHPC mix design implemented in this study (Table 2) has been extensively studied at both the material and member level by lots of companion papers [44-49]; the mixes consist of a sulphate resisting cement with a chemical composition in accordance with AS 3972 [50], a silica fume with meeting the requirements of AS 3582.3:2016 [51], a mined sand with a fineness modulus of 2.49 and a high-range water reducing agent with added retarder. For mixes containing fibres, a straight steel micro-fibre with a 0.2 mm diameter, 13 mm length and 2500 MPa tensile strength was added.

**Table 2**

Concrete mixing design (weight ratio to cement)

| | Cement ($kg/m^3$) | Silica fume ($kg/m^3$) | Sand ($kg/m^3$) | Water ($kg/m^3$) | SP ($kg/m^3$) | Fibre ($kg/m^3$) |
|---|---|---|---|---|---|---|
| 0% fibres | 960 | 255.5 | 960 | 182.4 | 43.2 | 0 |
| 1% fibres | 950.4 | 252.9 | 950.4 | 180.6 | 42.8 | 78 |
| 2% fibres | 940.8 | 250.4 | 940.8 | 178.8 | 42.3 | 156 |

The concrete was mixed in a 1200 kg planetary mixer, and due to this capacity restraint, for each concrete mix design, the concrete needed to be batched across 2 different mixes, the first used for the two simply supported beams and the second used the continuous beam. For each batch nine cylinders, three dog bones and three shrinkage specimens were also cast. During mixing the cement, silica fume and sand were first added to the mixer and blended until visibly mixed. The water and water reducing agent were then added and mixing continued for approximately 25 minutes, at which point the mortar was clearly flowable. The fibres were then added and mixing continued for a further 5 minutes.

After mixing the concrete was placed into the forms which were constructed from plywood for the beam tests and from steel for the material tests. After finishing the concrete, the specimens they were covered with wet hessian and plastic and left under ambient lab conditions until

being demoulded at 5 days. After demoulding, all specimens were stored at ambient lab conditions until the day of testing.

## 3. Results

### *3.1 Materials test*

The results of the compression tests are shown in Fig. 4 and supplemental materials (Table A1) summarise the key points (concrete age, compressive strength $f_c$, elastic modulus $E_c$, and strain at peak stress $\varepsilon_0$). In Fig. 4, specimens are designated according to the batch of concrete from which they were cast (SS for simply supported of C for continuous), the fibre volume (0%, 1% or 2%) and then the replicate number.

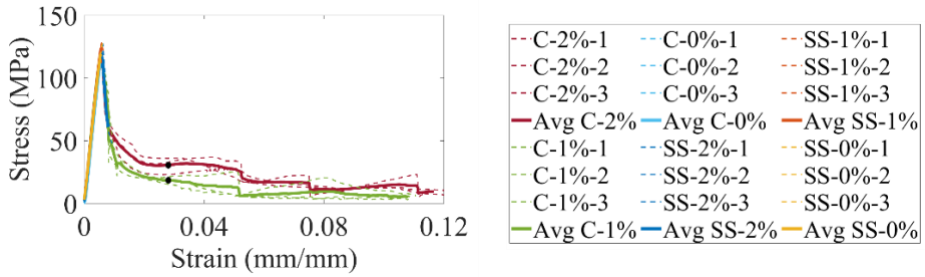


**Fig. 4.** Concrete compressive strain-stress relationship

Examining the compressive stress/strain results in Fig. 4, where the broken lines represent individual test results and the solid lines represent the average obtained for a given fibre volume, it can be seen that regardless of the fibre volume, the compressive strength and elastic modulus of the concrete remains relatively constant. This behaviour is expected because the fibres are not significantly engaged before the concrete fractures with the formation of a sliding wedge [11, 52, 53]. Once the peak load is reached, it can be seen that the concrete without fibres has no residual compressive strength and behaves in an elastic-brittle manner. For the concrete with fibres, a significant residual tensile strength is maintained for strains of up to 0.12, where for 1% fibres the residual stress is 18.2 MPa at a strain of 0.030 and for 2% fibres the residual stress is 31.2 MPa as outlined by black points shown in Fig. 4. Examining the results shown in supplemental material (Table A1), it can also be seen that there is little variability in concrete properties between batches of the same concrete mix design. It should be noted that in Fig. 4, post peak data is not available for SS-1% or SS-2% because of instrumentation failure.

Now considering the results of the direct tensile tests which are shown in Figs. 5. Figures 5(a)-(c) present the results of the 6 tests conducted on concrete with 0%, 1% and 2% fibre volume respectively, and for comparison, Fig. 5(d) shows the average and range of results for each fibre volume. In each part of Fig. 5, results are presented in terms of stress and strain prior to the localisation of the crack, which occurs at a stress and strain of $f_{ct}$, $\varepsilon_{ct}$. For concrete with fibres, an additional point $f_{SH}$, $\varepsilon_{SH}$ is tabulated and this represents the point at which micro-cracking occurred as indicated by the significant decrease in elastic modulus in Figs. 5(b)-(d).

The results show in Fig. 5 and summarised detailed results in supplemental material (Table A2) show that the stress $f_{ct}$ and strain $\varepsilon_{ct}$ at which crack localisation occurs is strongly dependent on the fibre volume fraction, and ranges from 2.07 MPa for concrete with no fibres to 5.91 MPa for concrete with fibres. For concrete without fibres tensile behaviour is elastic brittle. However, for concrete with fibres it can be seen in Figs. 5(b) and (c) that significant strain hardening occurs with peak strain hardening stresses $f_{ct}$ and strains $\varepsilon_{ct}$ reaching up to 4 MPa and 1.55E-04 for concrete with 1% fibres and 5.75MPa and 4.01E-04 for concrete with 2% fibres. Of interest is, however, that out of the 6 dog-bone test specimens for concrete with 1% fibres, only a single specimen showed strain hardening, whereas for concrete with 2% fibres, 5 of the 6 specimens showed strain hardening behaviour.

In Fig. 5(d), when comparing the average stress-strain and stress-crack width behaviour, it can be seen that the presence of fibres significantly improves both the stress and strain prior to the localisation of a single crack and also the stress transferred across a crack at a given crack width. This strong dependency on fibre volume can be simply explained by the larger volume of fibres crossing the crack as the fibre volume increases and hence a lager ability to transfer stress [54].

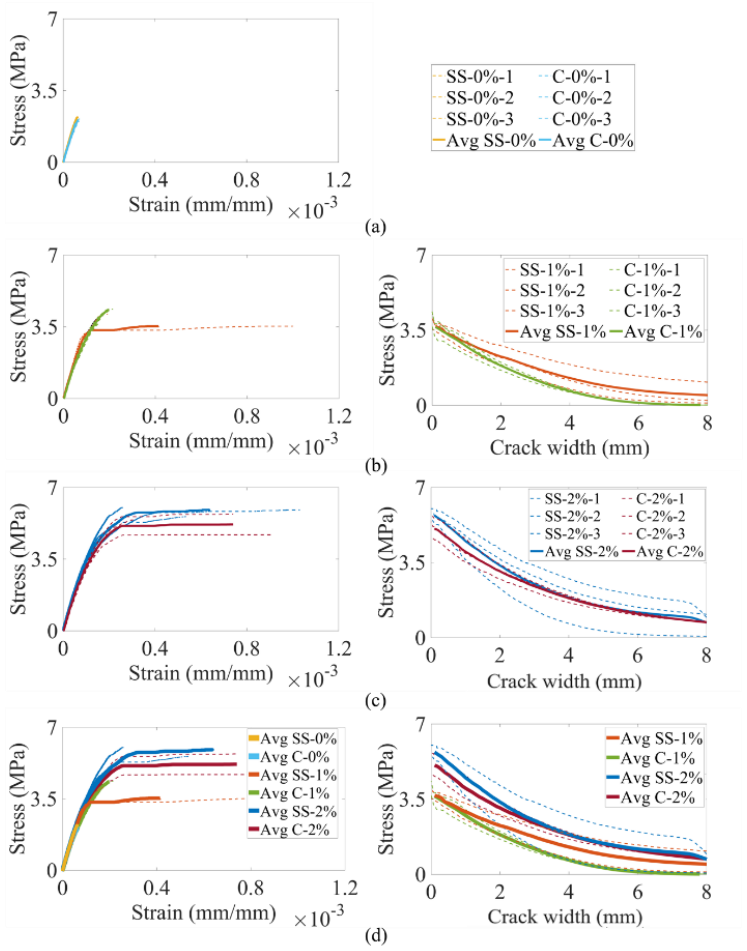


**Fig. 5.** Concrete tensile (left) strain-stress (right) crack opening-stress relationship for: (a) 0% fibre, (b) 1% fibre, (c) 2% fibre and (d) all average results for all types of concrete

In Table 3, the average shrinkage strain obtained from measurements on the three test prisms cast with each batch of concrete is reported along with the age of the concrete at the time of testing.

**Table 3**

Concrete shrinkage strain at the time of slab testing

| Slab specimen ID | Concrete age (days since casting) | $\varepsilon_{sh}$ (με) |
|---|---|---|
| SS0-S | 42 | 3.68E-04 |
| SS0-H | 35 | 3.61E-04 |
| SS1-S | 35 | 1.17E-04 |

| | | |
|---|---|---|
| SS1-H | 37 | 1.68E-04 |
| SS2-S | 35 | 2.67E-04 |
| SS2-H | 36 | 3.00E-04 |
| C0 | 44 | 3.62E-04 |
| C1 | 44 | 1.92E-04 |
| C2 | 42 | 3.39E-04 |

The experimentally measured stress/strain relationship of the 10 mm reinforcing bar and the profile deck is shown in Fig. 6, where the broken lines are the individual test results, and the solid lines are the average results. The average elastic modulus ($E_r$), yield strength ($f_y$), peak strength ($f_{pk}$) and corresponding strain ($\varepsilon_{pk}$) and rupture strength ($f_{rup}$) and strain ($\varepsilon_{rup}$) for both the reinforcing bar and profile sheet are tabulated in Table 4.

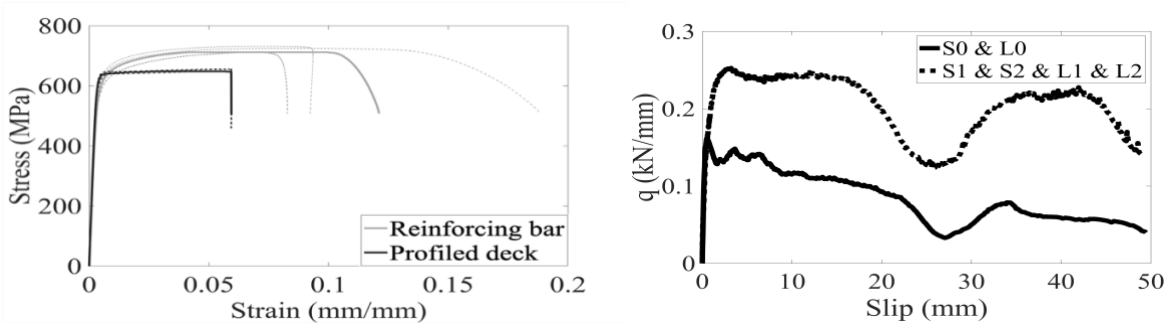


(a) (b)

**Fig. 6.** (a) Steel component tensile strain-stress relationship (b) Local bond property between UHPFRC and profiled deck

**Table 4**

Steel material properties

| | $f_y$ (MPa) | $E_r$ (GPa) | $f_{pk}$ (MPa) | $\varepsilon_{pk}$ | $f_{rup}$ (MPa) | $\varepsilon_{rup}$ |
|---|---|---|---|---|---|---|
| Reinforcing bar | 602 | 196 | 712 | 1.03E-01 | 508.44 | 1.21E-01 |
| Dove-tailed profiled deck | 633 | 212 | 654 | 5.68E-02 | 505.33 | 5.94E-02 |

Although not tested here, the shear flow slip ($q/\delta$) which governs interaction between the profile sheet and the concrete was measured using the same profile sheet and mix design with

either 0% or 2% fibres by one experimental paper [36]. The corresponding $q/\delta$ relationship is reproduced from that experimental paper [36] in Fig. 6(b), where the shear flow is given normalised by $\sqrt{f_c}$. Similarly, although not tested here, the bond stress/slip ($\tau/\delta$) relationship between reinforcement and the same concrete mix design has been investigated in other companion paper [37] and bond stress slip relationships are available.

### *3.2 Sagging Beams*

#### 3.2.1 Failure modes and load deflection relationship

The load/deflection relationship for the sagging slabs is shown in Fig. 7(a) and a photograph of each of the slabs following testing is shown in Fig. 8. For all slabs it can be seen that the beam initially loads with a stiff loading branch which corresponds to the uncracked section properties and that this stiffness is not impacted by the presence of fibres. This is to be expected, because as shown in Figs. 4 and 5, the elastic modulus of the concrete is not impacted by the presence of fibres. It can however be seen in Fig. 7(a), that the presence of fibres has a significant impact on the extent of the initial (uncracked) linear elastic branch; this is approximately indicated by the change in slope of the load/deflection relationship, that is the load to cause cracking changes from approximately 7.36 kN for the slabs with no fibres, to approximately 14.04 kN and 20.44 kN for the slabs with 1% and 2% fibres, respectively (see $P_{cr}$, $\Delta_{cr}$ in Table 5). The reason for this increase can be explained by the significant increase in both stress and strain at the localisation of cracks ($f_{ct}$ and $\varepsilon_{ct}$) in supplemental materials (Table A2).

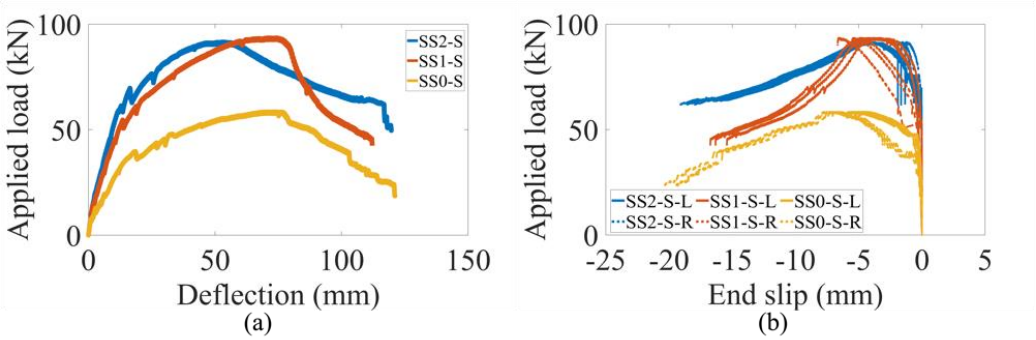


**Fig. 7.** (a) Applied load and deflection relationship for sagging test (b) Applied load and end slip relationship for sagging test

**Table 5**

Cracking load and ultimate load capacity in sagging test

| Specimen ID | $P_{cr}$ (kN) | $\Delta_{cr}$ (mm) | $P_{pk}$ (kN) | $\Delta_{pk}$ (mm) |
|---|---|---|---|---|
| SS0-S | 7.36 | 0.96 | 58.48 | 73.77 |
| SS1-S | 14.04 | 1.64 | 93.50 | 74.26 |
| SS2-S | 20.44 | 2.44 | 91.57 | 53.22 |

Following the localisation of a crack, the load deflection relationship continues to harden, but at a decreasing rate, until the peak load $P_{pk}$ is reached at a mid-span deformation of $\Delta_{pk}$ in Table 5. For concrete without fibres the peak load occurs at approximately 58.48 kN. However, for concrete with fibres, the peak load is reached at between 93.50 kN and 91.57 kN for concrete with either 1% or 2% fibres respectively. Significantly, it can be seen that the addition of 1% fibres has led to an approximately 40% increase in strength, but that the addition of fibres from 1% to 2% leads to a slight reduction in strength and mid-span deflection at the peak. The significant increase in strength when fibres are added can simply be explained by the increase in the total tensile force that can be carried by the cross section. For sections without fibres, this consists of the contributions of the uncracked concrete, tensile reinforcement, and profile sheet. For the sections with fibres, this consists of the uncracked concrete, the additional cracked concrete, tensile reinforcement and profile sheet.

As shown in Fig. 8, to accommodate the significant deformations at the location of the plastic hinge the tensile crack extends nearly the entire depth of the section and approximately meets the depth of the softening wedge. There is therefore little opportunity to increase the compressive force, that is the combined tensile forces generated by the profile sheet, tensile reinforcement and fibres effectively make the section over-reinforced. Hence the reason that the concrete with 2% fibres does not lead to a significantly higher strength than the concrete with only 1% fibres can be explained by the limiting of the total tensile force that can be developed by the total concrete compressive force that can be developed. That is, for both the sections with 1% and 2% fibres, the total moment capacity of the section is limited by concrete crushing, and if additional force could be developed in the compression region, such as through the addition of compression reinforcement, the strength of the section with 2% fibres would have been greater than that of the section with 1% fibres. Similar reasoning can be applied to

explain the reduction in deflection at peak load for the member with 2% fibres compared to the section with 1% fibres. That is, as the fibre content is increased, the total tensile force develops more rapidly in the section with a higher fibre concrete and this leads to a lower member deflection at the onset of concrete crushing.

It can also be seen in Fig. 7(a), that the addition of fibres significantly increases member ductility. Importantly, unlike compressive strength which was not significantly impacted by increasing the fibre volume from 1% to 2%, in Fig. 7(a) that the ductility is significantly increased with higher fibre volumes. This behaviour can be explained by the increased residual branch of the compressive stress strain relationship in Fig. 4, which occurs because the increased fibre volume restrains sliding along fractured sliding plane [47].

In Fig. 7(b), it can be seen that the load end-slip relationships have a similar overall shape but with higher loads developed with the addition of fibres. This behaviour is expected, because as shown in Fig. 6(b), the $q/\delta$ relationships show a ductile response regardless of the presence of fibres, but a higher load can be developed if fibres are added because the fibres increase confinement provided along the sheet concrete interface as it is trapped within the dovetail void [36].


**Fig. 8.** Sagging test slab failure

### 3.2.2 Crack spacing and crack widths

In Table 6, the average crack spacing is reported for cracks within the constant moment region, along with the average, minimum and maximum crack widths at each load. In Table 6, a dash indicates that at the given load level no cracks have formed and a tilde means the crack widths had stopped being measured at this given load level as it was deemed to be outside of the serviceability region.

Firstly, considering the location of cracks, if the crack spacing is considered to be fully developed at the final load step at which crack widths were recorded, the average crack spacing within the constant moment region reduces from 91 mm for the slab with no fibres to 77 mm for the slab with 1% fibres and 62 mm for the slab with 2% fibres. This reduction in crack spacing is expected and occurs because the stress at the crack face increases with increasing fibre volumes. That is, as described through partial-interaction theory [55-57], cracks will form at a distance beyond an existing crack face when the stress developed in the concrete reaches the tensile cracking stress, hence if the stress at an existing crack face is higher because of an increased presence of fibres, less stresses are required to be transferred from the reinforcing bar to the concrete to cause a crack to form thereby reducing crack spacing [56].

**Table 6**

Crack spacing and width summary for sagging test

| Load (kN) | 0% | | | | 1% | | | | 2% | | | |
|---|---|---|---|---|---|---|---|---|---|---|---|---|
| | Width (mm) | | | Spacing (mm) | Width (mm) | | | Spacing (mm) | Width (mm) | | | Spacing (mm) |
| | Avg | Min | Max | | Avg | Min | Max | | Avg | Min | Max | |
| 15 | 0.045 | 0.038 | 0.052 | 249 | 0.011 | 0.011 | 0.011 | - | - | - | - | - |
| 30 | 0.141 | 0.055 | 0.250 | 157 | 0.037 | 0.037 | 0.037 | - | - | - | - | - |
| 45 | 0.174 | 0.031 | 0.514 | 91 | 0.028 | 0.015 | 0.063 | 192 | 0.014 | 0.014 | 0.014 | - |
| 60 | ~ | ~ | ~ | ~ | 0.032 | 0.010 | 0.136 | 77 | 0.018 | 0.014 | 0.031 | 165 |
| 75 | ~ | ~ | ~ | ~ | ~ | ~ | ~ | ~ | 0.025 | 0.009 | 0.057 | 62 |

The crack width results tabulated in Table 6 are plotted in Fig. 9. In Fig. 9, the ‘cross’ shaped markers indicate the individual crack width measurements, and the round markers indicate the average crack width. It can be seen that under any given load level the crack width is significantly reduced by the presence of fibres and the crack width continues to reduce as the fibre content increases. Again, this behaviour can be explained through the application of partial-interaction theory. The crack width is given as the integral of the difference in strain between the reinforcement and concrete between adjacent cracks. Hence, as the volume of fibres increases, for any given magnitude of load that must be transferred across a crack, a larger proportion of the load will be carried by the fibres and a lower proportion will be carried by the reinforcement, that is the difference in strain between the reinforcement and the concrete

will be reduced. Further, because the crack spacing reduces with increases in fibre volume, the total difference in strain is integrated over a smaller crack spacing and therefore the overall slip is reduced [58].

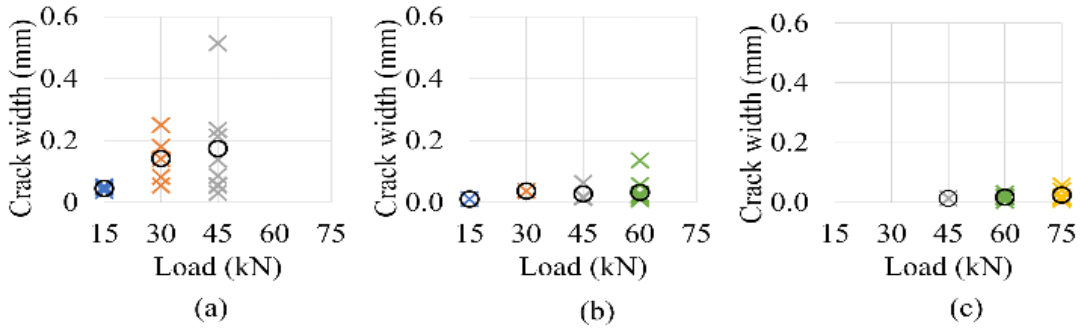


**Fig. 9.** Crack width record for sagging test: (a) SS0-S, (b) SS1-S and (c) SS2-S

### 3.3 Hogging Beams

#### *3.3.1 Failure modes and load deflection relationship*

The load/mid-span deflection relationships of the hogging beams are shown in Fig. 10(a) and the corresponding load/end slip relationships in Fig. 10(b). The results of the hogging beams are similar to those of the sagging beams in that the presence of fibres leads to an increase in the load to cause cracking (Table 7), but unlike the sagging beams, the stiffness of the beams with 2% fibres is significantly higher than the beams with 1% fibres. The increase in stiffness can again be explained by the additional force that is carried across the cracked tension region as the fibres content increases. The reason that the difference in stiffness between the beams with 1% and 2% fibres is bigger in the hogging cross sections is that the profile sheet does not contribute to the total tensile force in the hogging region and so the total tensile force that is developed at any given deformation is more strongly influenced by the contribution of the fibres.

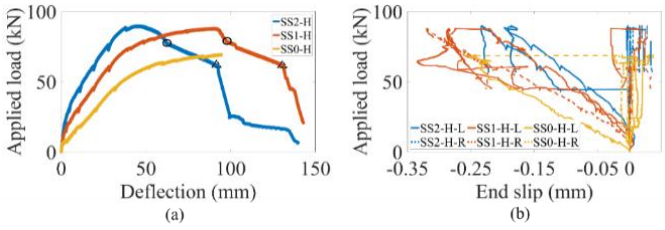

**Fig. 10.** (a) Applied load and deflection relationship for hogging test (b) Applied load and end slip relationship for hogging test

**Table 7**

Cracking load and ultimate load capacity in hogging test

| Specimen ID | $P_{cr}$ (kN) | $\Delta_{cr}$ (mm) | $P_{pk}$ (kN) | $\Delta_{pk}$ (mm) |
|---|---|---|---|---|
| SS0-H | 7.18 | 1.31 | 72.86 | 94.49 |
| SS1-H | 12.04 | 1.43 | 87.87 | 90.93 |
| SS2-H | 19.16 | 1.77 | 89.77 | 44.77 |

In Fig. 10(a) and Table 7, it is again seen that the ultimate strength is significantly increased by the presence of fibres (i.e. increasing from 0% to 1% fibres), but not impacted significantly by increasing the fibre content from 1% to 2%. The reason for this behaviour is very similar to that explained for the sagging region, that is, the capacity of the member is limited by the ability to generate any additional compressive forces because the large magnitude of forces resisted by the fibres, reinforcement and profile sheet effectively make the section over-reinforced. It was not possible to generate significant additional forces in the profile sheet, because although it was the thickest profile available, extensive buckling occurred, with extensive bucking indicated by the circle markers in Fig. 10(a). After the profile sheet buckles, the load continues to drop due to a reduction in the overall compressive force capacity (arising from both a reduction in the concrete force due to softening and a reduction in the profile sheet force due to buckling), until a sudden reduction in load occurs when the tensile reinforcement begins to rupture at the location of the triangular marker. Note that the full load deflection relationship for the beam with 0% fibres could not be obtained because the LVDT ran-out at 100 mm deformation.

In Fig. 10(b), it can be seen that there is no strong trend in the load/end-slip relationships because these results are heavily influenced by the localised buckling that happened along the member span and because the profile sheet was trapped beneath the loading pins shown in Fig. 11.

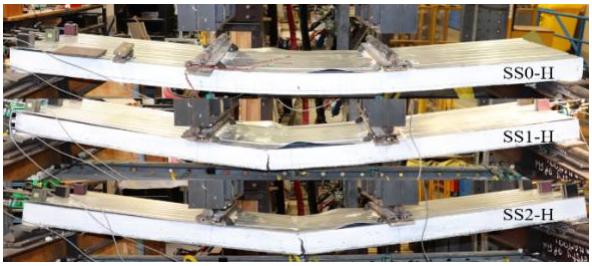


**Fig. 11.** Hogging test slab failure

### *3.3.2 Crack spacing and crack widths*

The location of each crack measured from the left hand side of the constant moment region and the corresponding crack width at each load interval is summarised in Table 8 for the beams with 0%, 1% and 2% fibre volume, respectively.

It can be seen, that in general, and as described for the sagging beams, that as the fibre content increases, the crack spacing and crack width both reduce. With the fully developed crack spacing reducing from 46 mm for 0% fibres to 31 mm for 1% fibre volume and 37 mm for 2% fibre volume. Interestingly, for the hogging beams, the differentiation in crack spacing between 1% and 2% fibres is not as significant as it was for the sagging beams, and this may be because of the reduced spacing of the longitudinal tensile reinforcement (510 mm for the sagging beams compared to 127.5 mm for the hogging beams) and this reduced spacing may have disrupted the local distribution of fibres.

Examining the distributions of crack widths shown in Fig. 12, it is again seen that, as expected, the crack width reduces as the fibre content increases, but the magnitude of reduction is not as significant as was seen for the sagging cross sections. Again, this may be due to less well dispersed fibres as a result of the close bar spacing and small cover.

**Table 8**

Crack spacing and width summary for hogging test

| Load (kN) | 0% | | | | 1% | | | | 2% | | | |
|---|---|---|---|---|---|---|---|---|---|---|---|---|
| | Width (mm) | | | Spacing (mm) | Width (mm) | | | Spacing (mm) | Width (mm) | | | Spacing (mm) |
| | Avg | Min | Max | | Avg | Min | Max | | Avg | Min | Max | |
| 15 | 0.092 | 0.070 | 0.111 | 113 | 0.016 | 0.010 | 0.025 | 160 | - | - | - | - |
| 30 | 0.113 | 0.024 | 0.176 | 62 | 0.027 | 0.010 | 0.097 | 52 | 0.010 | 0.006 | 0.014 | 89 |
| 45 | 0.132 | 0.024 | 0.251 | 46 | 0.041 | 0.015 | 0.140 | 35 | 0.018 | 0.008 | 0.063 | 57 |
| 60 | ~ | ~ | ~ | ~ | 0.051 | 0.009 | 0.214 | 31 | 0.029 | 0.008 | 0.158 | 39 |
| 75 | ~ | ~ | ~ | ~ | ~ | ~ | ~ | ~ | 0.038 | 0.005 | 0.291 | 37 |

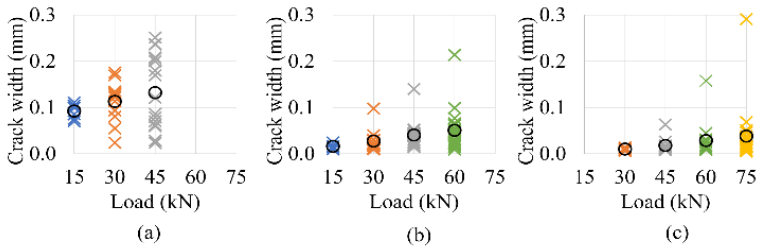


**Fig. 12.** Crack width record for hogging test: (a) SS0-H, (b) SS1-H and (c) SS2-H

### 3.4 Continuous Beams

#### *3.4.1 Failure modes and load deflection relationship*

In Fig. 13(a), the load-deflection relationships measured at mid-point of each span are shown, where the solid line and dash line are used to differentiate between each span. As expected, the general shape largely mirrors that obtained from the simply supported beams, in that the introduction of fibres significantly increases the load to cause cracking, the cracked stiffness and the ultimate strength, but that the increase in fibres from 1% to 2% leads to a less significant change in stiffness and very little change in strength. Interestingly, when comparing the ductility of all of the continuous beam load/deflection relationships with those obtained from the simply supported beams, it can be seen that the continuous beams are significantly more ductile (softening occurs at a slower rate), and that there is less difference in the ductility of the

beams with 1% and 2% fibres. This outcome can be explained by the redistribution of moments and will be investigated further in the following subsection. Figure 14, shows a photograph of each beam at the end of loading, from which it can be observed that each beam failed with the formation of three plastic hinges, and for the beam with no fibres, as shown in Figs. 14(b) and (c), ultimate failure was by longitudinal splitting of the concrete which caused a complete loss of load.

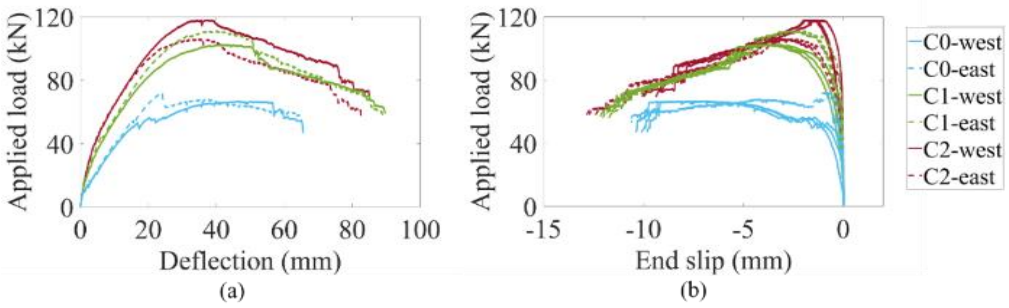


**Fig. 13.** Applied load and (a) deflection and (b) end slip relationship for continuous slab test

In Fig. 13(b) the load/end-slip relationships for the profile sheet show a relatively consistent slip across the width of the profile and a general shape that is very similar to that observed for the sagging simply supported beam. From the failure photos shown in Figs. 14(b) and (c), it can be observed that there is a splitting behaviour that occurred for the slab without fibres which corresponds to catastrophic failure at the end of the test.

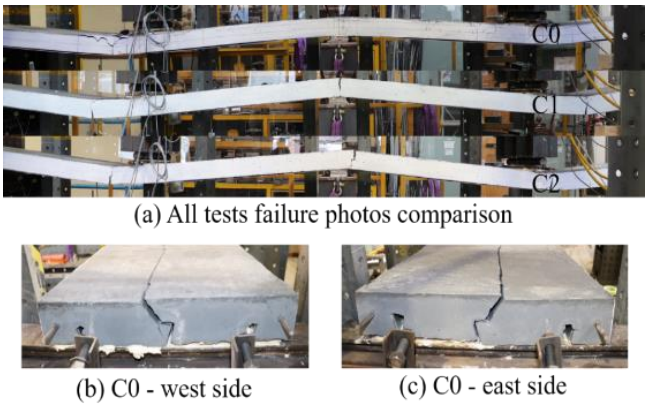


**Fig. 14.** Failure photos for continuous slab

### *3.4.2 Moment redistribution*

Figure 15 shows the degree of moment redistribution at the central support labelled ‘H’ and at the loading point of each span labelled ‘East’ and ‘West’, and where the experimental percentage moment redistribution is

$$K_{MR} = \frac{M_{el} - M_{exp}}{M_{el}} \quad (1)$$

where in Eq. 1, $M_{el}$ is the moment at either the hogging support *H* or at the beam mid-spans *East* and *West*, and $M_{exp}$ is the experimental moment calculated at each of these key points based on the applied load and the experimentally measured load at the hogging support.

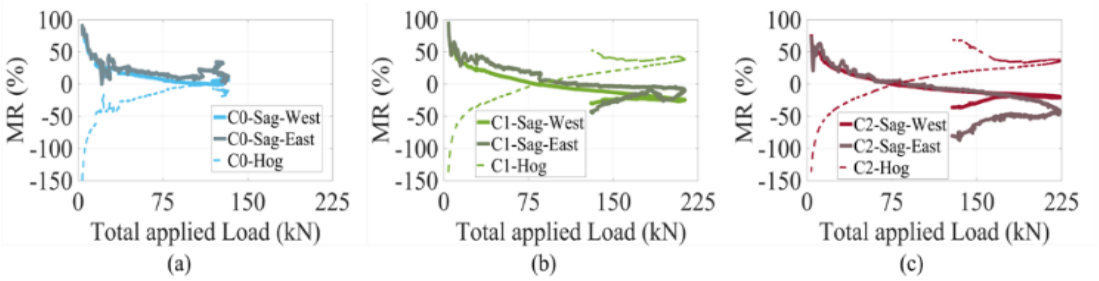


**Fig. 15.** Moment redistribution percentage for each individual tests (a) C0 (b) C1 (c) C2

In Fig. 15, it can be seen that under initial loading when the section is uncracked, the degree of moment redistribution is very high because the relative stiffness in the uncracked hogging and sagging cross sections is high (as a result of the different reinforcement ratios in Table 1). Upon increasing the load, redistribution reduces as the stiffness of the hogging cross sections and sagging cross sections become more similar as a result of cracking. Interestingly, it can be seen in Fig. 16, that at the end of the serviceability limit state (40% of the peak load), that moment redistribution is highest in the beam with no fibres and is essentially zero in the beams with fibres. This is because at this point there is a significant difference between the degree of cracking in the hogging and sagging region of the beam without fibres, but for the beams with fibres, the ability to transfer stress across the cracks limits the difference in stiffness between the hogging and sagging regions.

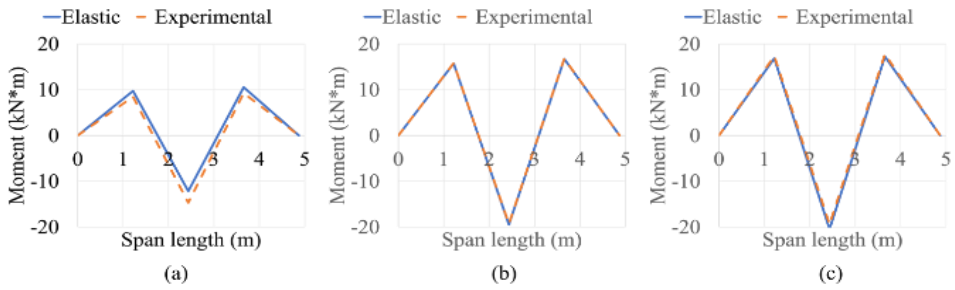


**Fig. 16.** Moment distribution along slab (a) C0 (b) C1 (c) C2 - 40% peak load

When the load is further increased to the peak in Fig. 17, it is seen that moment redistribution is significantly higher in the beams with fibres. This can be explained by the fact that for the

beam with no fibres the entire span has approached the cracked flexural rigidity, but for the beams with fibres, relative stiffness along the span is more strongly dependent on the degree of cracking and hence the stiffness is more variable.

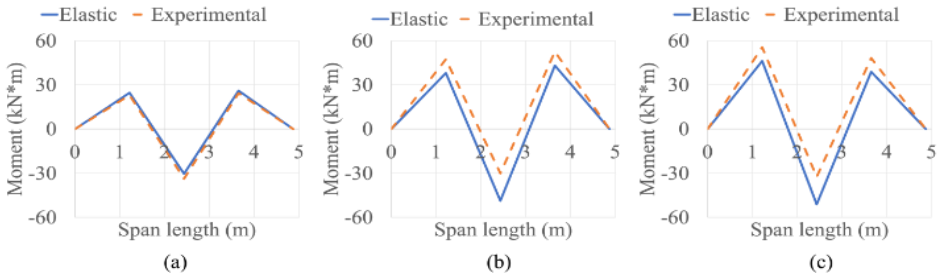


**Fig. 17.** Moment distribution along slab (a) C0 (b) C1 (c) C2 - at maximum loading

In Fig. 18, the degree of moment redistribution is shown at the end of the test where it is again seen that the degree of moment redistribution is higher in the beams with fibres than in the beam with no fibres. This increase in moment redistribution can be explained by the significantly larger ductility of the hogging and sagging cross sections that contained fibres than the cross sections that did not contain fibres, with this increased sectional ductility allowing for larger hinge rotations before failure.

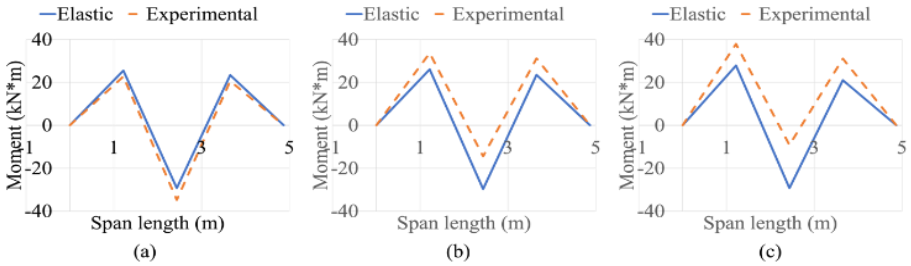


**Fig. 18.** Moment distribution along slab (a) C0 (b) C1 (c) C2 - end of test

## 4. Conclusion

Simply supported and continuous composite profiled slabs comprising of UHPFRC and profiled decks were studied in this paper, in respect of the flexural displacement, longitudinal end slip, crack spacing and widths and moment redistribution, in order to illustrate the effect of fibre content on the behaviour of composite profiled members.

Tests on simply supported slabs subjected to a sagging moment showed that:

1. The presence of fibres significantly increased the load to cause macro-cracking, and that with either 1% or 2% fibres, member stiffness to approximately 40% of the peak load was similar to the uncracked member stiffness.
2. As fibre content increased the number of cracks that formed increased, but the crack width reduced significantly. The crack width was strongly dependent on fibre volume, with the maximum crack widths being up to 58.1% smaller when applying 2% fibres over 1% fibres.
3. The addition of 1% or 2% fibres led to an increase in flexural strength of 20.6% and 23.2% over beams with 0% fibres, respectively. Little change in flexural strength was observed by increasing the fibre content from 1% to 2%, however it was felt that this was due to the random distribution of fibres.
4. Although strength did not improve when increasing fibre content from 1% to 2% ductility was significantly improved.

Tests on simply supported hogging regions showed similar results but found that the increases in the initial stiffness were less pronounced than for sagging regions, and were more dependent on fibre volume. This outcome can be explained by the lower total tensile forces that are generated in the hogging cross section and the larger proportion of the total tensile force being carried by the fibres.

Tests on two-span continuous beams showed similar trends to the simply supported sagging beams in terms of improvements in stiffness and strength. When considering moment redistribution, it was shown that moment redistribution at the serviceability limit state is smaller for beams with fibres than for beams without fibres. This outcome is because the difference in the cracked and uncracked stiffness of the beams reduces with the presence of fibres. At the ultimate limit state, the level of moment redistribution increased with increasing fibre volume, and this is because, as shown in the simply supported beam tests, the ductility of the hinge regions is improved by the addition of fibres. With this outcome arising from the restraint of concrete softening wedges and the generation of higher residual compressive stresses.

## Declaration of Competing Interest

The authors declare that they have no known competing financial interests or personal relationships that could have appeared to influence the work reported in this paper.

## Acknowledgements

This material is based upon work supported by the Australian Research Council Discovery Project 190102650. Sirui Chen was supported by an Australian Government Research Training Program Scholarship. The authors also wish to acknowledge the assistance of Mr Jon Ayoub in completing the lab testing.

## Supplemental materials

Table A1 and Table A2 are available online in the ScienceDirect Library (Structures | Journal | ScienceDirect.com by Elsevier)

## References

[1] Emami F, Kabir M Z. Performance of composite metal deck slabs under impact loading. Structures 2019;19:476-489. https://doi.org/10.1016/j.istruc.2019.02.015.

[2] Chen S, Shi X, Qiu Z. Shear bond failure in composite slabs-a detailed experimental study. Steel Compos Struct 2011;11(3):233-250. DOI: 10.12989/scs.2011.11.3.233

[3] Crisinel M, Marimon F. A new simplified method for the design of composite slabs. J Construct Steel Res 2004;60(3-5):481-491. https://doi.org/10.1016/S0143-974X(03)00125-1.

[4] Ganesh G M, Upadhyay A, Kaushik S K. Simplified Design of Composite Slabs Using Slip Block Test. J Adv Concr Technol 2005;3(3):403-412. DOI: 10.3151/jact.3.403.

[5] Kan Y C, Chen L H, Yen T. Mechanical behavior of lightweight concrete steel deck. Constr Build Mater 2013;42:78-86. https://doi.org/10.1016/j.conbuildmat.2013.01.007.

[6] Simon J, Visuvasam J, Babu S. Study on shear embossments in steel-concrete composite slab. IOP Conference Series: Materials Science and Engineering 2017;263(3):032022. DOI: 10.1088/1757-899X/263/3/032022.

[7] Abas F, Gilbert R, Foster S, and Bradford M. Strength and serviceability of continuous composite slabs with deep trapezoidal steel decking and steel fibre reinforced concrete. Eng Struct 2013;49:866-875. https://doi.org/10.1016/j.engstruct.2012.12.043.

[8] Ackermann F P, Schnell J. Steel Fibre Reinforced Continuous Composite Slabs. Composite Construction in Steel and Concrete VI 2011:125-137. DOI: 10.1061/41142(396)11.

[9] Gholamhoseini A, Khanlou A, MacRae G, Hicks S, Scott A, Clifton C. Short-term behaviour of reinforced and steel fibre–reinforced concrete composite slabs with steel decking under negative bending moment. Adv Struct Eng 2018;21(9):1288-1301. https://doi.org/10.1177/1369433217739710.

[10] Gholamhoseini A, Khanlou A, MacRae G, Scott A, Hicks S, and Leon R. An experimental study on strength and serviceability of reinforced and steel fibre reinforced concrete (SFRC) continuous composite slabs. Eng Struct 2016;114:171-180. https://doi.org/10.1016/j.engstruct.2016.02.010.

[11] Hassan A, Jones S, Mahmud G. Experimental test methods to determine the uniaxial tensile and compressive behaviour of ultra high performance fibre reinforced concrete (UHPFRC). Constr Build Mater 2012;37:874-882. https://doi.org/10.1016/j.conbuildmat.2012.04.030.

[12] Hussein L, Amleh L. Structural behavior of ultra-high performance fiber reinforced concrete-normal strength concrete or high strength concrete composite members. Constr Build Mater 2015;93:1105-1116. https://doi.org/10.1016/j.conbuildmat.2015.05.030.

[13] Hamoda A, Hossain K, Sennah K, Shoukry M, Mahmoud Z. Behaviour of composite high performance concrete slab on steel I-beams subjected to static hogging moment. Eng Struct 2017;140:51-65. https://doi.org/10.1016/j.engstruct.2017.02.030.

[14] Huang L, Xie J, Li L, Xu B, Huang P, Lu Z. Compressive behaviour and modelling of CFRP-confined ultra-high performance concrete under cyclic loads. Constr Build Mater 2021;310:124949. https://doi.org/10.1016/j.conbuildmat.2021.124949.

[15] Qi J, Cheng Z, Wang J, Tang Y. Flexural behavior of steel-UHPFRC composite beams under negative moment. Structures 2020;24:640-649. https://doi.org/10.1016/j.istruc.2020.01.022.

[16] Gholamhoseini A. Experimental and finite element study of ultimate strength of continuous composite concrete slabs with steel decking. Int J Adv Struct Eng 2018;10:85-97. DOI: 10.1007/s40091-018-0183-3.

[17] Kwak H G, Seo Y J. Time-dependent behavior of composite beams with flexible connectors. Comput Method Appl M 2002;191(34):3751-3772. https://doi.org/10.1016/S0045-7825(02)00293-1.

[18] Visintin P, Sturm A B, Mohamed Ali M, Oehlers D J. Blending macro-and micro-fibres to enhance the serviceability behaviour of UHPFRC. Aus J Civ Eng 2018;16(2):106-121. DOI: 10.1080/14488353.2018.1463608.

[19] Visintin P, Mohamad Ali M S, Xie T, Sturm A B. Experimental investigation of moment redistribution in ultra-high performance fibre reinforced concrete beams. Constr Build Mater 2018;166:433-444. https://doi.org/10.1016/j.conbuildmat.2018.01.156.

[20] Lin J, Lin L, Peng Z, Xu R, Wang G. Cracking Performance in the Hogging-Moment Regions of Natural Curing Steel-UHPC and Steel-UHTCC Continuous Composite Beams. J Bridge Eng 2022;27(2):04021106. doi:10.1061/(ASCE)BE.1943-5592.0001820.

[21] Yoo S W, Choo J F. Evaluation of the flexural behavior of composite beam with inverted-T steel girder and steel fiber reinforced ultra high performance concrete slab. Eng Struct 2016;118:1-15. https://doi.org/10.1016/j.engstruct.2016.03.052.

[22] Zhang Y, Cai S, Zhu Y, Fan L, Shao X. Flexural responses of steel-UHPC composite beams under hogging moment. Eng Struct, 2020;206:110134. https://doi.org/10.1016/j.engstruct.2019.110134.

[23] Lin W, Yoda T, Taniguchi N. Application of SFRC in steel–concrete composite beams subjected to hogging moment. J Construct Steel Res 2014;101:175-183. https://doi.org/10.1016/j.jcsr.2014.05.008.

[24] L. Bai, Y. Li, C. Hou, T. Zhou, and M. Cao, "Longitudinal shear behaviour of composite slabs with profiled steel sheeting and ECC," Eng Struct 2020;205. https://doi.org/10.1016/j.engstruct.2019.110085

[25] Hossain K, Attarde S, Anwar M. Finite element modelling of profiled steel deck composite slab system with engineered cementitious composite under monotonic loading. Eng Struct 2019;186:13-25. https://doi.org/10.1016/j.engstruct.2019.02.008.

[26] Hossain K M A, Alam S, Anwar M S, Julkarnine K M Y. High performance composite slabs with profiled steel deck and Engineered Cementitious Composite – Strength and shear bond characteristics. Constr Build Mater 2016;125:227-240. https://doi.org/10.1016/j.conbuildmat.2016.08.021.

[27] Mohammed B S, Aswin M, Beatty W H, Hafiz M. Longitudinal shear resistance of PVA-ECC composite slabs. Structures 2016;5:247-257. https://doi.org/10.1016/j.istruc.2015.12.003

[28] Aarthi D K, Jeyshankaran E, Aranganathan N. Comparative study on longitudinal shear resistance of light weight concrete composite slabs with profiled sheets. Eng Struct 2019;200:109738. https://doi.org/10.1016/j.engstruct.2019.109738.

[29] Li X, Zheng X, Ashraf M, Li H. Experimental study on the longitudinal shear bond behavior of lightweight aggregate concrete – Closed profiled steel sheeting composite slabs. Constr Build Mater 2017;156:599-610. https://doi.org/10.1016/j.conbuildmat.2017.08.108.

[30] Sohel K M A, Liew J Y R, Fares A I. Shear bond behavior of composite slabs with ultra-lightweight cementitious composite. J Build Eng 2021;44:103284. https://doi.org/10.1016/j.jobe.2021.103284.

[31] Lu L, Ding Y, Guo Y, Hao H, Ding S. Flexural performance and design method of the prefabricated RAC composite slab. Structures 2022;38:572-584. https://doi.org/10.1016/j.istruc.2022.02.022

[32] Zhang H, Zhang H Y, Geng Y, Fang P Q, Wang Y. Design formulae for Long-Term responses of continuous Steel-Recycled aggregate concrete composite slabs. Structures 2022;45:1477-1490. https://doi.org/10.1016/j.istruc.2022.09.092

[33] Holmes N, Dunne K, O'Donnell J. Longitudinal shear resistance of composite slabs containing crumb rubber in concrete toppings. Constr Build Mater 2014;55:365-378. https://doi.org/10.1016/j.conbuildmat.2014.01.046.

[34] Mohammed B S. Structural behavior and m– k value of composite slab utilizing concrete containing crumb rubber. Constr Build Mater 2010;24(7):1214-1221. https://doi.org/10.1016/j.conbuildmat.2009.12.018.

[35] Yi O, Mills J E, Zhuge Y, Ma X, Gravina R J, Youssf O. Performance of Crumb Rubber Concrete Composite-deck Slabs in 4-point-bending. J Build Eng 2021;40:102695. https://doi.org/10.1016/j.jobe.2021.102695.

[36] Chen S, Visintin P, Oehlers D J. Bond between very-high and ultra-high performance fibre reinforced concrete and profiled deck sheeting. J Build Eng 2022;52:104426. https://doi.org/10.1016/j.jobe.2022.104426.

[37] Sturm A B, Visintin P. Local bond slip behavior of steel reinforcing bars embedded in ultra high performance fibre reinforced concrete. Struct Concr 2019;20(1):108-122. https://doi.org/10.1002/suco.201700149.

[38] Standard Australia. Methods of testing concrete. AS 1012.9:2000, Sydney, Australia, 2000.

[39] Standard Australia. Methods of testing concrete. AS 1012.17-1997, Sydney, Australia, 1997.

[40] Singh M, Sheikh A H, Ali M S M, Visintin P, Griffith M. Experimental and numerical study of the flexural behaviour of ultra-high performance fibre reinforced concrete beams. Constr Build Mater 2017;138:12-25. https://doi.org/10.1016/j.conbuildmat.2017.02.002.

[41] Standard Australia. Methods of testing concrete. AS 1012.13:2015, Sydney, Australia, 2015.

[42] Standard Australia. Steel for the reinforcement of concrete. AS/NZS 4671:2019, Sydney, Australia, 2019.

[43] Standard Australia. Metallic materials - Tensile testing - Method of test at room temperature. AS 1391:2020, Sydney, Australia, 2020.

[44] Fang C, Ali M, Xie T, Visintin P, Sheikh A H. The influence of steel fibre properties on the shrinkage of ultra-high performance fibre reinforced concrete. Constr Build Mater 2020;242:117993. https://doi.org/10.1016/j.conbuildmat.2019.117993.

[45] Sobuz M H, Visintin P, Ali M, Singh M, Griffith M, Sheikh A. Manufacturing ultra-high performance concrete utilising conventional materials and production methods. Constr Build Mater 2016;111:251-261. https://doi.org/10.1016/j.conbuildmat.2016.02.102.

[46] Sturm A B, Visintin P, Seracino R, Lucier G, Oehlers D J. Flexural performance of pretensioned ultra-high performance fibre reinforced concrete beams with CFRP tendons. Compos Struct 2020;243:112223. https://doi.org/10.1016/j.compstruct.2020.112223.

[47] Sturm A B, Visintin P, Oehlers D J. Closed-form expressions for predicting moment redistribution in reinforced concrete beams with application to conventional concrete and ultrahigh performance fiber reinforced concrete. Struct Concr 2020;21(4):1577-1596. https://doi.org/10.1002/suco.201900498.

[48] Sun M, Visintin P, Bennett T. The effect of specimen size on autogenous and total shrinkage of ultra-high performance concrete (UHPC). Constr Build Mater 2022;327:126952. https://doi.org/10.1016/j.conbuildmat.2022.126952.

[49] Sturm A B, Visintin P, Oehlers D J. Blending fibres to enhance the flexural properties of UHPFRC beams. Constr Build Mater 2020;244:118328. https://doi.org/10.1016/j.conbuildmat.2020.118328.

[50] Standard Australia. General purpose and blended cements. AS/NZS 3972, Sydney, Australia, 2010.

[51] Standard Australia. Supplementary cementitious materials, Part 3: Amorphous silica. AS/NZS 3582.3:2016, Sydney, Australia, 2016.

[52] Larsen I L, Thorstensen R T. The influence of steel fibres on compressive and tensile strength of ultra high performance concrete: A review. Constr Build Mater 2020;256: 119459. https://doi.org/10.1016/j.conbuildmat.2020.119459.

[53] Le Hoang A, Fehling E. Influence of steel fiber content and aspect ratio on the uniaxial tensile and compressive behavior of ultra high performance concrete. Constr Build Mater 2017;153:790-806. https://doi.org/10.1016/j.conbuildmat.2017.07.130.

[54] Wille K, El-Tawil S, Naaman A E. Properties of strain hardening ultra high performance fiber reinforced concrete (UHP-FRC) under direct tensile loading. Cem Concr Compos 2014;48:53-66. https://doi.org/10.1016/j.cemconcomp.2013.12.015.

[55] Gupta A K, Maestrini S R. Tension-stiffness model for reinforced concrete bars. J Struct Eng 1990;116(3):769-790. https://doi.org/10.1061/(ASCE)0733-9445(1990)116:3(769).

[56] Sturm A B, Visintin P, Oehlers D J, Seracino R. Time-dependent tension-stiffening mechanics of fiber-reinforced and ultra-high-performance fiber-reinforced concrete. J Struct Eng 2018;144(8):04018122. https://doi.org/10.1061/(ASCE)ST.1943-541X.0002107.

[57] Wu Z, Yoshikawa H, Tanabe T. Tension stiffness model for cracked reinforced concrete. J Struct Eng 1991;117(3):715-732. https://doi.org/10.1061/(ASCE)0733-9445(1991)117:3(715).

[58] Visintin P, Oehlers D J. Fundamental mechanics that govern the flexural behaviour of reinforced concrete beams with fibre-reinforced concrete. Adv Struct Eng 2018;21(7):1088-1102. https://doi.org/10.1177/1369433217739705.

## CHAPTER 4 – Numerical Analysis

### Introduction

The publication titled “Quantifying the serviceability flexural benefit of using UHPFRC in profiled slabs” brings out a comprehensive study that applies a rotational partial-interaction numerical analysis to determine the flexural performance of simply supported profiled slabs incorporating UHPFRC, considering time-dependent effects under sagging or hogging moments in the serviceability limit state.

To validate this numerical method, the load/deflection and load/slip results are compared with the experimental results presented in Chapter 3. Therefore, for both the sagging tests and hogging tests, three individual tests are conducted with different fibre contents (0%, 1% and 2%). In total, six individual test results will be used to validate the feasibility of this numerical method.

To obtain a reasonable range of numerical results, for each test, three different material strengths are applied in simulation analysis where these material strengths are categorised as upper bound (UB), average bound (AVE) and lower bound (LB), which are referred from material tests in Chapter 2.

To study the importance of bond connection between concrete and profiled deck, additional simulated load-deflection results are obtained for individual tests under the sagging moment, assuming that the shear force is zero throughout the entire process. These results are also compared with composites that have bond connection to evaluate the influence of bond connection on the flexural performance of composite slab in serviceability behaviour.

**Statement of Authorship**

# Statement of Authorship

| | |
|---|---|
| Title of Paper | Quantifying the serviceability flexural benefits of using UHPFRC in profiled slabs |
| Publication Status | ☐ Published ☐ Accepted for Publication<br>☑ Submitted for Publication ☐ Unpublished and Unsubmitted work written in manuscript style |
| Publication Details | Chen, S., Visintin, P., Sturm, A.B. and Oehlers, D. J. (2023) 'Quantifying the serviceability flexural benefits of using UHPFRC in profiled slabs', submitted on Structural Concrete |

## Principal Author

| | | | |
|---|---|---|---|
| Name of Principal Author (Candidate) | Sirui Chen | | |
| Contribution to the Paper | Investigation, simulation, results processing, writing - original draft | | |
| Overall percentage (%) | 85% | | |
| Certification: | This paper reports on original research I conducted during the period of my Higher Degree by Research candidature and is not subject to any obligations or contractual agreements with a third party that would constrain its inclusion in this thesis. I am the primary author of this paper. | | |
| Signature | | Date | 14/08/2023 |

## Co-Author Contributions

By signing the Statement of Authorship, each author certifies that:

i. the candidate's stated contribution to the publication is accurate (as detailed above);

ii. permission is granted for the candidate in include the publication in the thesis; and

iii. the sum of all co-author contributions is equal to 100% less the candidate's stated contribution.

| | | | |
|---|---|---|---|
| Name of Co-Author | Phillip Visintin | | |
| Contribution to the Paper | Conceptualization, methodology, supervision, writing - review | | |
| Signature | | Date | 14/08/2023 |

| | | | |
|---|---|---|---|
| Name of Co-Author | Alexander Bonaparte Sturm | | |
| Contribution to the Paper | Conceptualization, methodology, supervision, writing - review | | |
| Signature | | Date | 14/08/2023 |

Please cut and paste additional co-author panels here as required.

# Statement of Authorship

| | | | |
|---|---|---|---|
| Name of Co-Author | Deric John Oehlers | | |
| Contribution to the Paper | Conceptualization, supervision, writing -review | | |
| Signature | | Date | 14/08/2023 |

Please cut and paste additional co-author panels here as required.

**Quantifying the serviceability flexural benefit of using UHPFRC in profiled slabs**

S. Chen, Ph. D.[1]; P. Visintin[2]; A. B. Sturm[3]; and D. J. Oehlers[4]

[1]Ph. D. candidate, School of Civil, Environmental and Mining Engineering, Univ. of Adelaide, Adelaide, SA 5005, Australia.

[2]Professor, School of Civil, Environmental and Mining Engineering, Univ. of Adelaide, Adelaide, SA 5005, Australia. (Corresponding author). ORCID: http://orcid.org/0000-0002-4544-2043. Email: Phillip.visintin@adelaide.edu.au

[3]Assistant professor, Department of Civil Engineering, National Cheng Kung University, 70101, Taiwan

[4]Emeritus professor, School of Civil, Environmental and Mining Engineering, Univ. of Adelaide, Adelaide, SA 5005, Australia.

**Abstract**

Using ultra-high-performance fibre-reinforced concrete (UHPFRC) in profiled slabs, as opposed to normal strength concrete without fibres, has been shown experimentally to significantly increase both the bond between the profiled sheet and the concrete, and the tensile forces across cracked concrete. The consequence of these fibre benefits is to substantially increase the flexural rigidity leading to reduced deflections and also to substantially reduced crack widths leading to improved behaviour under serviceability loads and to improved durability. To quantify these benefits so that they can be used in design, a rational partial-interaction numerical model has been developed that can incorporate the material properties of any type of UHPFRC including time-effects. This modelling should help in the development of simplified design rules for specific fibre types.

**Keywords**

Profiled slabs; ultra-high-performance fibre-reinforced concrete (UHPFRC); partial-interaction mechanics; serviceability

## Introduction

Steel-concrete composite structural forms, including those with composite steel decks, are widely utilised to reduce self-weight, improve member performance and allow for rapid construction (Marimuthu et al. 2007). Similarly, the use of ultra-high-performance fibre-

reinforced concrete (UHPFRC) at the member level is gaining increased attention because of the ability to significantly reduce member deflection, crack width and durability, and to increase member strength and ductility (Visintin et al. 2018; Yu et al. 2020; Akhnoukh and Buckhalter 2021).

When considering steel concrete composite structures constructed using UHPFRC, the vast majority of research has considered composite beams. For example, experimental work by Qi et al. (2020) Wang et al. (2020), Xiao et al. (2021) and Zhang et al. (2021) has shown that the application of UHPFRC to steel concrete composite beams leads to reduced deflections and crack widths and increased member stiffness, strength and ductility. Surprisingly, there are few papers that study profiled deck slabs constructed using UHPFRC. To date, experimental work has been limited to that by Chen et al. (2022a) who quantified the bond between UHPFRC and various profiled decks and found the bond to be highly dependent of the presence of fibres. Work by the same group (Chen et. al 2022b) experimentally investigated the impact of varying fibre volumes when using UHPFRC for continuous, and simply supported slabs. This work showed similar general outcomes to that found for composite beams, that is, as the volume of fibres increased member deflection and crack width reduced and member strength and ductility increased. The outcomes of this work using UHPFRC also aligns with general outcomes observed for normal strength fibre reinforced concrete, where studies have shown that the presence of even a small volume of fibres can increase the load to cause cracking, longitudinal bond strength, the post cracking stiffness, the flexural strength and member ductility (Petkevičius and Valivonis 2010; Ackermann and Schnell 2011; Abas et al. 2013; Lin et al. 2014; Abas et al. 2016; Gholamhoseini et al. 2016; Gholamhoseini et al. 2018; Hamoda et al. 2017; Nguyen and Lee 2021).

A significant motivation of previous research on fibre reinforced concrete is to investigate the potential to replace a proportion of the traditional continuous reinforcement with fibres as a means of crack control under in-service loading (Abas et al. 2013; Gholamhoseini et al. 2016). While the above literature review demonstrates this has been shown experimentally under instantaneous loading for a range of different concrete strengths and fibre volumes, there is presently limited design guidance on how to implement this concrete in practice. It is therefore the purpose of this paper to develop a generic analysis technique that can be used as the basis of design for serviceability. The intention is to simulate the generic partial interaction-

mechanisms that are observed in practice and to allow for the unavoidable impacts of concrete time effects such that this model can be used in the future to develop simplified approaches.

In the remainder of the paper, the bond-slip characteristics of the reinforcement with the adjacent concrete is first considered as this controls the partial-interaction mechanics. It is then shown how the behaviour of profiled slabs is governed by numerous distinct partial-interaction mechanisms. These are first described qualitatively after which numerical solutions are developed. The model is then validated by comparison with test results on UHPFRC and the effects of crack spacing and widths studied to show the importance and contribution of fibres.

## Bond-slip material properties

The bond between the profiled sheet and the adjacent concrete is often measured in pull tests as illustrated in Fig. 1 (Chen et al. 2022a; Hadigheh et al. 2015), where the width of the profiled sheet is $w_{slab}$ (illustrated into the page), the cross-sectional area is $A_{pr}$ and the bonded length is $L_{emb}$. The bonded length $L_{emb}$ is chosen to be small enough such that the bond across the interface can be assumed to be of a constant value (Chen et al. 2022a). If the axial force $P_{emb}$ applied to the sheet causes a slip $S_{emb}$ as shown, then the shear flow strength $q_{pr}$ is equal to $P_{emb}/L_{emb}$. This is the longitudinal shear force over a unit longitudinal length for the width of profile sheet $w_{slab}$ for a specific slip $S_{emb}$.

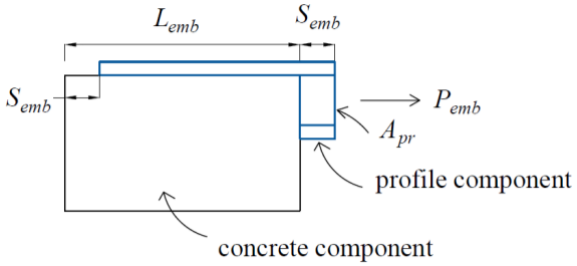


**Fig. 1.** Elevation of profile sheet bond strength test

Tests have shown that the variation of $q_{pr}$ with slip $S_{emb}$ (Chen et al. 2022a) can be idealised as in Fig. 2 where $S$ is the interface slip. There is an initial chemical and mechanical bond O-A which has a peak strength $q_{max}$ at an interface slip $\delta_1$ which occurs at a very small slip, and once broken has zero strength A-B. After the initial chemical and mechanical bond has broken, the interface shear is transferred by friction $q_{frc}$ along D-E, where the magnitude of the frictional branch D-E relative to O-A is dependent on the concrete strength and volume of fibres.

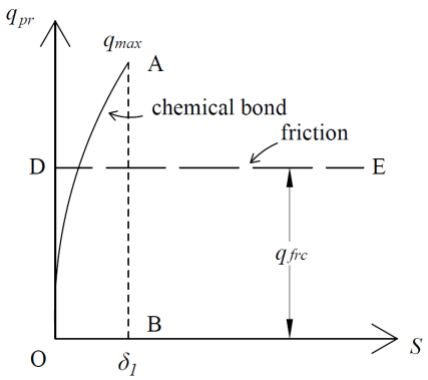


**Fig. 2.** Idealised profiled bond behaviour

The shear flow strength of the tension reinforcing bars in the profiled slab can also be determined from similar tests as in Fig. 2 or taken from existing bond/slip properties (Yoo et al. 2014; Marchand et al. 2016; Sturm and Visintin 2018). If $P_{emb}$ is the force applied to a bar to cause a slip $S_{emb}$, then the shear flow strength of that individual bar $q_{bar}$ is $P_{emb}/L_{emb}$ for that specific slip $S_{emb}$ and dumming the shear flow strengths of all the individual tension bars is the shear flow strength $q_{rb}$ for all the tension reinforcing bars.

Fibres bridging a crack also pull out, that is slip. The individual fibre bond-slip can be measured (Naaman et al. 1991; DiFrancia et al. 1996) and used to quantify the overall bond-slip relationship. Alternatively the fibre stress $\sigma_f$ crack width $W$ relationship can be determined directly from dog-bone tests (Hassan et al. 2012; Yu et al. 2020) or approximated using generic material models (Wille et al. 2014).

## Profiled slab behaviour governing mechanisms

A half span of length $L$ of a simply supported profiled slab of depth $h_{ps}$ is shown in Fig. 3(a). Prior to any interface slip of the profiled sheet or of the reinforcing bars and prior to flexural cracking (that is the flexural crack shown forming), the behaviour is governed by elementary full-interaction (FI) mechanics.

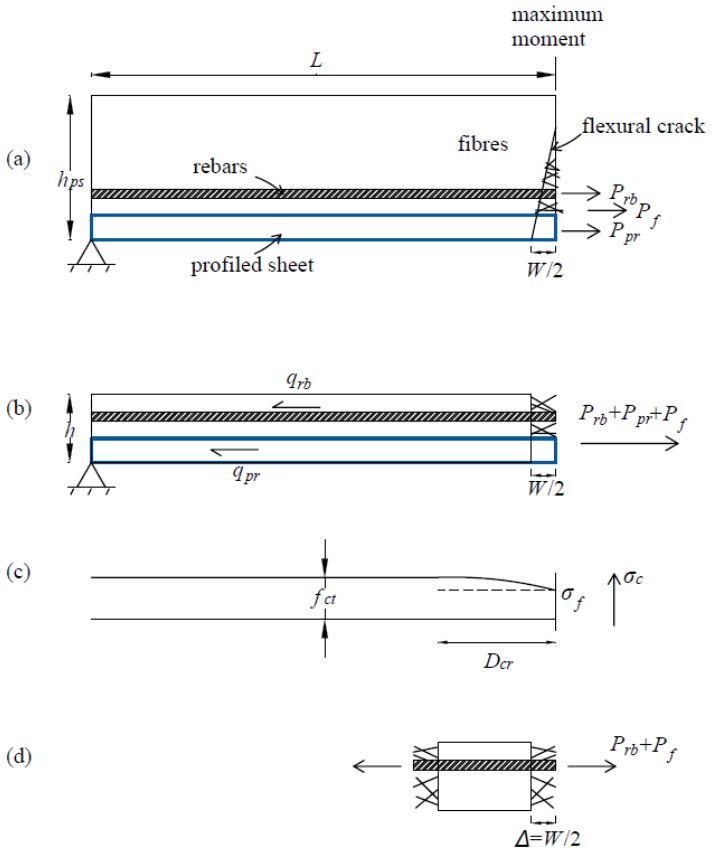


**Fig. 3.** Tension chord crack analyses: (a) initial crack; (b) tension chord; (c) crack spacing; and (d) P-$\Delta$

As the applied load on the profiled slab in Fig. 3(a) is increased, a flexural crack will eventually form at the position of maximum moment where the half crack width at the soffit is $W/2$. The widening of this crack causes slip between the fibres and the adjacent concrete and similarly between both the reinforcing bars and profiled sheet and their adjacent concrete. Because of this slip, there is now partial-interaction (PI) mechanical behaviour such that the total force in the fibres spanning the crack $P_f$ depends on the crack width and similarly for the reinforcing bars $P_{rb}$ and for the profiled sheet $P_{pr}$.

It is common practice to determine the forces at the crack in Fig. 3(a) from a tension-chord analysis as illustrated in Fig. 3(b) which consists of a concentrically loaded prism of depth $h$. The axial force in the reinforcing bars $P_{rb}$ depends on the crack width $W$ and shear flow strength of the reinforcing bars $q_{rb}$, the axial force in the profile $P_{pr}$ depends on $W$ and the shear flow strength of the profile $q_{pr}$, and the axial force in the fibres $P_f$ depends on the crack width as this controls the fibre stress $\sigma_f$. This analysis can also be used to determine the axial stress in the concrete that is $\sigma_c$ in Fig. 3(c) and where this tends to the tensile strength of the concrete $f_{ct}$,

the crack spacing $D_{cr}$. It can be seen that $D_{cr}$ depends on both $q_{pr}$ and $q_{rb}$ as well as on the fibre stress $\sigma_f$. This tension chord analysis can directly cope with time effects such as creep and shrinkage (Sturm et al. 2018).

A tension-chord analysis can also be used to quantify reinforcement debonding (Oehlers 2006; Oehlers et al. 2016) which can also directly cope with creep and shrinkage. Debonding of the profiled sheet is illustrated in Fig. 4(a) where the axial force now only includes the force in the profiled sheet $P_{pr}$ and the fibre force $P_f$. When the axial force is sufficient to cause the chemical bond in Fig. 2 to be fully developed as in Fig. 4(b), then this is the force to start debonding and is referred to as the IC (intermediate crack) debonding resistance $P_{IC}$ (Oehlers et al. 2016). Any further increase in the force $P$ is resisted by the frictional component $P_{frc}$ over the debonded length $L_{dbd}$ as in Fig. 4(c). This mechanism has been used to quantify debonding of externally bonded plates (Oehlers 2006; Oehlers et al. 2016). Debonding of the reinforcing bars follows exactly the same mechanism but because reinforcing bars have very strong bond this is very unlikely to occur. Debonding of the fibres also follows exactly the same mechanism but because of the random orientation and anchorage of the fibres across cracks this is quantified experimentally.

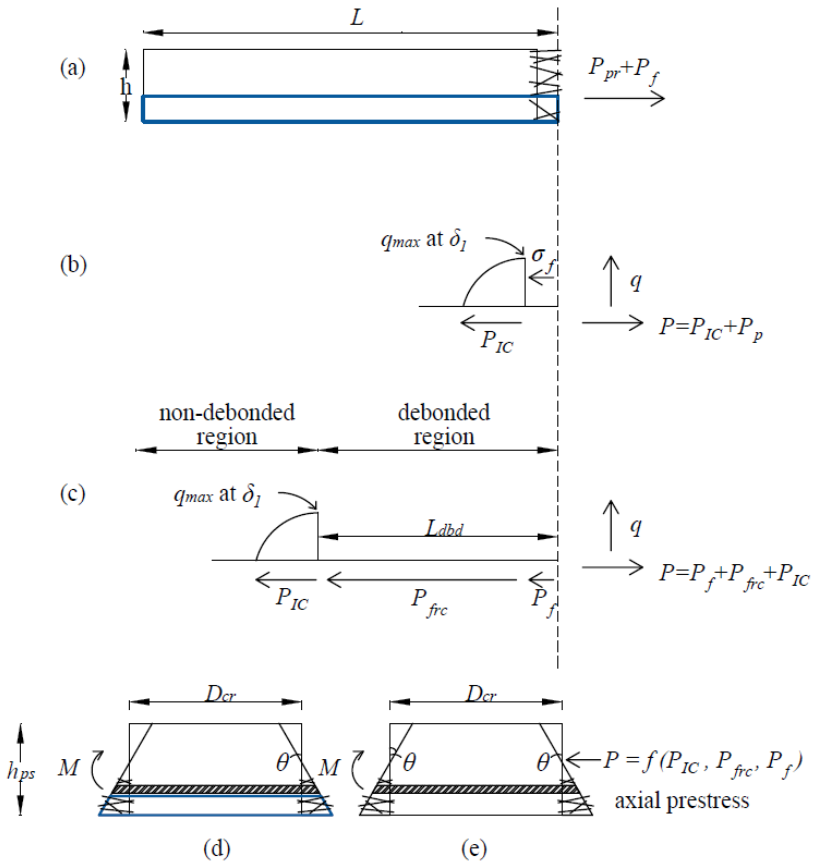


**Fig. 4.** Tension chord debonding analysis: (a) tension chord; (b) start of debonding; (c) debonding; (d) non-debonded region; and (e) debonded region

Within the non-debonded region of the profiled slab in Fig. 4(c), a longitudinal segment of the slab between cracks at a spacing $D_{cr}$ is shown in Fig. 4(d). In this segment, the profiled sheet, the reinforcing bars and the fibres act directly as tension reinforcement. A segmental analysis of a reinforced concrete beam (Visintin et al. 2013; Sturm et al. 2020) can be used to determine the moment/rotation ($M/\theta$) and consequently moment/curvature ($M/\chi$) properties for the non-debonded length of the profiled slab. Within the debonded region of the profiled slab in Fig. 4(c), a segment between cracks as shown in Fig. 4(e) consists of a concrete segment with reinforcing bars and fibres with an axial prestress that is equal to the axial force in the profiled sheet. It is important to emphasise that the only reinforcement within this segment is that of the reinforcing bars and fibres, that is the profiled sheet does not act as reinforcement within this segment. Instead, the profiled sheet acts to generate a prestressing force to the segment. In this case a segmental analysis of a prestressed reinforced concrete beam (Knight et al. 2013; Oehlers et al. 2016) is applicable. In summary, the difference between Figs. 4(d) and (e) is the difference in the flexural behaviours of the non-debonded and debonded regions.

The final mechanism that controls the behaviour of profiled sheets occurs when IC debonding is complete, that is when the debonded length $L_{dbd}$ in Fig. 4(c) equals $L$ in which case the maximum axial force in the profile is now $L$ times $q_{frc}$. This mechanism will be explained in full in the following analysis where it will also be shown that this fully debonded analysis can be used directly for the partially debonded analysis in Fig. 4(c).

### PI fully debonded composite member global analysis

The mechanics of the global member behaviour is first described using a unique approach that requires the local relationship between the moment, curvature and longitudinal strain ($M/\chi/\varepsilon$). It is then shown how these local relationships, which allow for the effects of fibres on micro and macrocracking and also such time effects as shrinkage can be determined directly from a displacement based segmental analysis. The member fully debonded global analysis is first illustrated in full for a simply supported composite profiled slab under sagging moments. It is then shown how the approach can also be applied to partially debonded slabs and for slabs in hogging regions.

The half span of a simply supported composite profiled slab that is symmetrically loaded about mid-span is shown in Fig. 5(a) where $L$ is the half span length, $d_{slb}$ is the depth of the slab and $d_{pr}$ that of the profiled sheet.

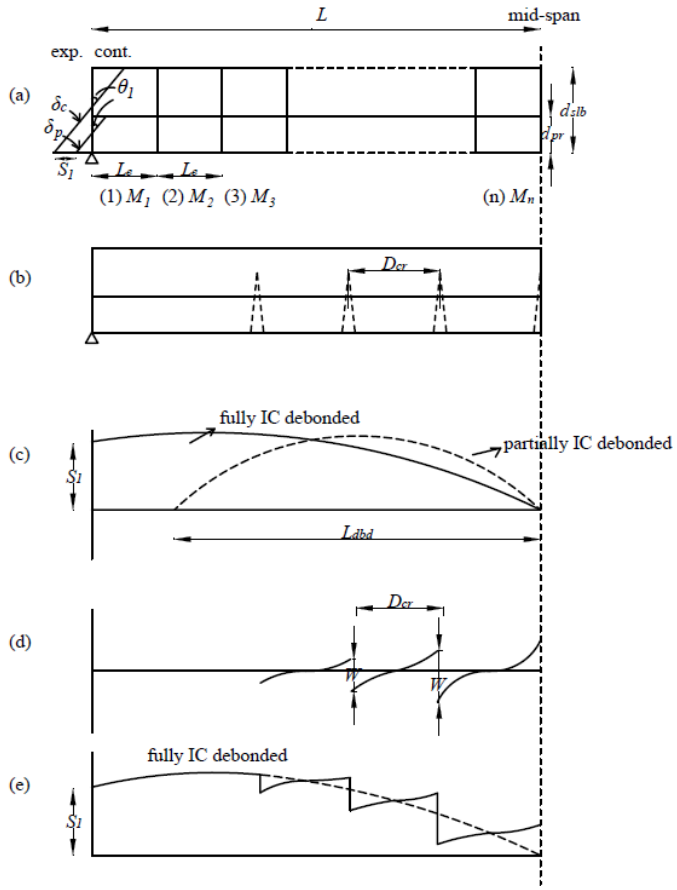


**Fig. 5.** Simply supported profiled slab in sagging: (a) rotational bending; (b) crack spacing; (c) global slip $f(q_{pr})$; (d) local slip $f(q_{pr}+q_{rb})$; and (e) total slip

The deformation $\delta$ of the profiled slab in Fig. 5(a) is shown over the left-hand side (LHS) support where movement to the right signifies contraction and that to the left expansion. The Euler–Bernoulli deformation of the reinforced concrete (RC) component of the composite profiled slab is labelled $\delta_c$ and that of the profiled sheet $\delta_p$. As profiled sheets are designed to prevent vertical separation from the RC component, the rotations of both components is the same ($\theta_1$). The longitudinal discontinuity of these deformations at the support is the interface slip $S_1$ between the RC component and the profiled component for the fully IC debonded case being considered here. It can be seen that this interface slip $S_1$ is constant over the height of the slab. This slip at the support $S_1$ is the accumulation of the interface slip along the slab such as that shown in Fig. 5(c) for the 'fully IC debonded' case, which is governed by the interface frictional shear flow between the RC component and the profiled component that is $q_{frc}$ in Fig. 2. It can also be seen in Fig. 5(c) that when the slab is symmetrically loaded then by symmetry the slip at mid-span is zero.

A shooting method of analysis is used to determine the mechanical behaviour of the beam in Fig. 5(a). This approach is used as it can visually illustrate the mechanics and importantly can cope with any material properties and include concrete shrinkage and creep. The beam is divided into very small elements of length $L_e$ such at $L_e << L$ and where the applied moments within each element are labelled $M_1$ to $M_n$. Let us consider the first element adjacent to the support which is shown in Fig. 6.

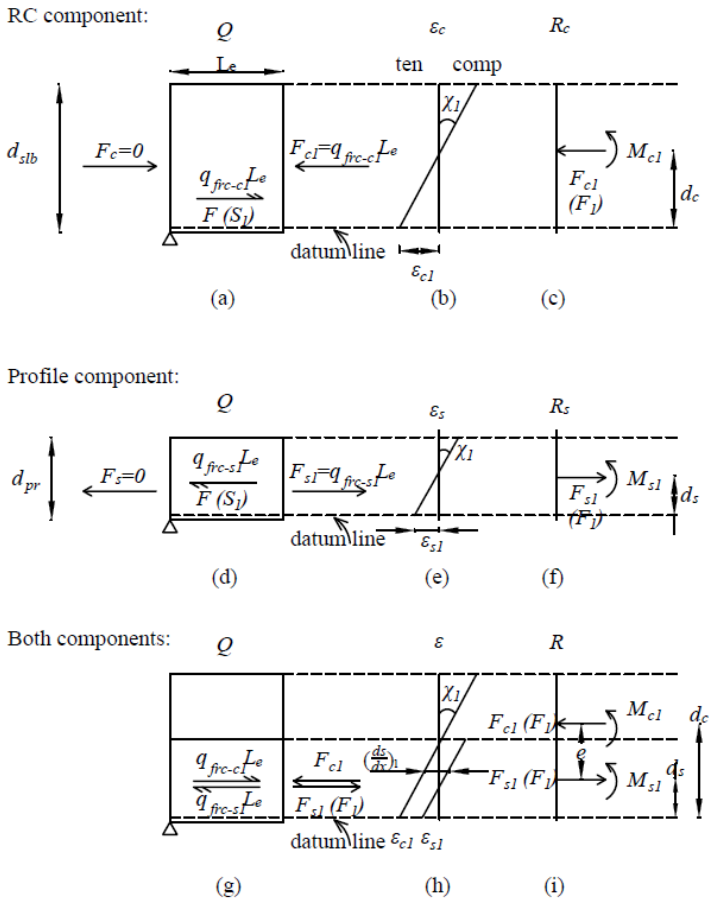


**Fig. 6.** Analysis of Element 1

The RC component is shown in Fig. 6(a). At this stage, the interface slip $S_1$ is not known so a guess will have to be made of its value. The value of the guess will be iterated until a known boundary condition is achieved which in this case is $S = 0$ at mid-span. On the LHS of Fig. 6(a), the axial force $F_c$ is zero as this is the free surface of the slab. The interface slip $S_1$ will induce a shear force $q_{frc}L_e$ that induces overall compression in the component and has been labelled $q_{frc\text{-}c1}L_e$. Hence the compressive axial force on the RHS $F_{c1}$, of magnitude $F_1$, is equal to $q_{frc\text{-}c1}L_e$ plus the force on the LHS which is zero. The profile component is shown in Fig. 6(d). It can be seen that the same shear force acts on this element but in the opposite direction

to induce an overall tensile force $F_{s1}$, also magnitude $F_1$, which has the same magnitude as $F_{c1}$. The shear forces on both components is shown in Fig. 6(g). They are equal and opposite and of magnitude $F_1$.

The stress resultants in the RC component of Element 1 are shown in Fig. 6(c). At some arbitrary level $d_c$ from any fixed datum level the axial compressive force is $F_{c1}$ which is in this case $q_{frc\text{-}c1}L_e$ of magnitude $F_1$ and there is also a moment within the RC component at this datum level of $M_{c1}$. Similarly in the profile component in Fig. 6(f). At some arbitrary level $d_s$, the axial tensile force is $F_{s1}$ which has a magnitude $F_1$ and there is a moment $M_{s1}$ at this arbitrary level. The combined stress resultants are shown in Fig. 6(i) where it can be seen that the total moment has three components: that is the RC component $M_{c1}$; the profiled component $M_{s1}$; and the longitudinal shear component $F_1e$ where $e$ is the distance between the arbitrary levels that is $d_c$-$d_s$. Hence for equilibrium, the applied moment $M_1$ must equal the sum of these three components that is

$$M_n = M_{cn} + M_{sn} + F_n e \tag{1}$$

in which the components in Eq. (1) will vary with the arbitrary levels chosen, that is with $d_c$ and $d_s$ in Fig. 4, but the sum will always remain constant.

The strain distribution in the RC component is shown in Fig. 6(b) and that in the profile component in Fig. 6(e). It is necessary to determine the curvature $\chi_1$ in both components which results in an axial force of known magnitude $F_1$ in both components and in which Eq. (1) applies. To find a solution, the mechanical properties of the components are required. These can be derived from a moment/curvature ($M/\chi$) analysis and are shown in an idealised form for the RC component in Fig. 7 where $\varepsilon_c$ is the strain at the level of an arbitrary datum line as shown in Fig. 6(b). The flexural rigidity of the uncracked section at serviceability is often assumed to be constant at $(EI)_c$ in Fig. 7. Flexural cracking causes a drop in the flexural rigidity but the change depends on the crack spacing, the PI behaviour of the fibres bridging the crack, the magnitude of the axial loads and other non-linearities such as shrinkage. It is worth bearing in mind that $F_c$ in Fig. 7 is the axial prestress in Fig. 4(e).

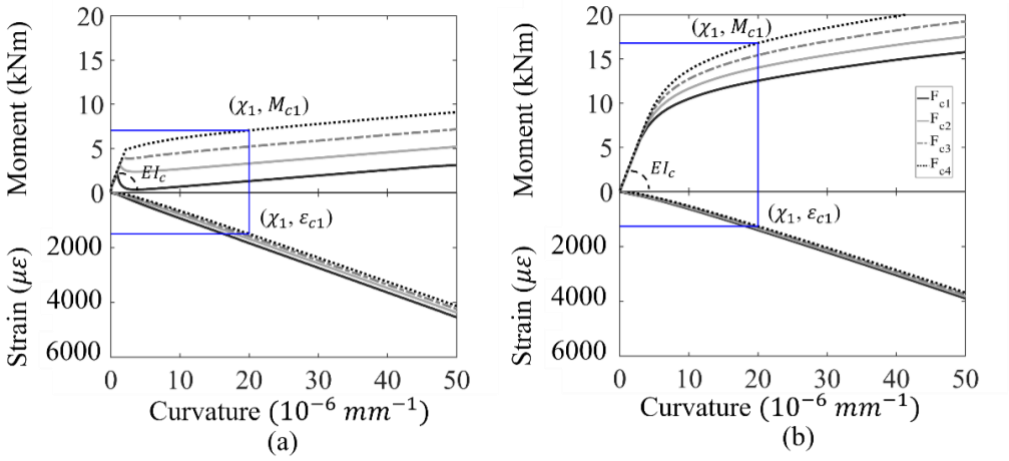


**Fig. 7.** RC component mechanical properties: (a) UHPC; and (b) UHPFRC

The results of a $M/\chi$ analysis of the profiled component are also idealised in Fig. 8. In this case there is no cracking and therefore no PI and hence any non-linearity is due to that in the material properties.

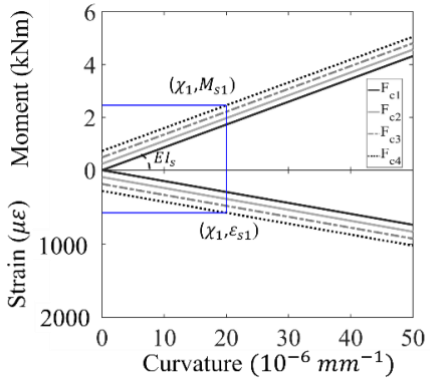


**Fig. 8.** Profile component mechanical properties

Once the mechanical properties are determined as in Figs. 7 and 8, it is a question of determining the curvature $\chi_1$ when a known axial load $F_1$ is acting which satisfies Eq. (1). When equilibrium is satisfied, the strains at the datum level $\varepsilon_{c1}$ and $\varepsilon_{s1}$ can also be determined from the graphs. These are shown in the combined strain profiles in Fig. 6(h). The difference in strain that is $\varepsilon_{c1}$ minus $\varepsilon_{s1}$ is referred to as the slip-strain $ds/dx$ and can be seen to be constant over the depth of the member. Integration of this slip-strain over the length of the element, that is $(ds/dx)L_e$, is the change in slip over the element. Hence

$$S_n = S_{n-1} - \left(\frac{dx}{ds}\right)_{n-1} L_e \tag{2}$$

The analysis of the next element in the beam in Fig. 5(a) is shown in Fig. 9. The slip has now reduced as given by Eq. (2). The shear force at this element due to the slip $S_2$ is shown as $q_{frc\text{-}c2}L_e$ and hence the axial force increases by this amount as shown. The analysis follows the same procedure as for Element 1. The analysis continues to the mid-span element in Fig. 5(a). For this symmetrically loaded beam, the boundary condition at mid-span is $S$ is zero. If this does not occur then the initial guess of the slip $S_1$ is changed or iterated until it does.

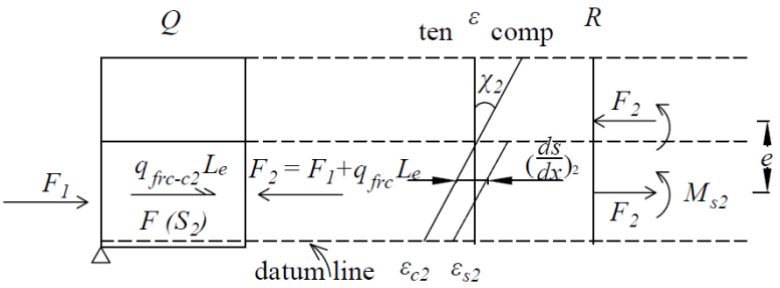


**Fig. 9.** Analysis of Element 2

## PI segmental local properties

The mechanical properties in the RC segment in Fig. 4(e) shown in Fig. 7, that are required for the above member analysis, depend on PI material properties and hence cannot be obtained directly from a conventional FI $M/\chi$ analyses; instead a moment-rotation ($M/\theta$) analysis has to be used (Knight et al. 2013). A segment of the RC component of the profiled slab is shown in Fig. 10(a). The segment length in Fig. 10(a) is equal to the flexural crack spacing $D_{cr}$ which can be obtained from a tension chord analysis as depicted in Fig. 3. The analysis in Fig. 10(a) allows for the bond strength of the reinforcing bars $q_{rb}$, for the fibre stresses $\sigma_f$ and also for the concrete shrinkage strain $\varepsilon_{sh}$ and creep if necessary; full details of this tension chord analysis are given elsewhere (Sturm et al. 2018).

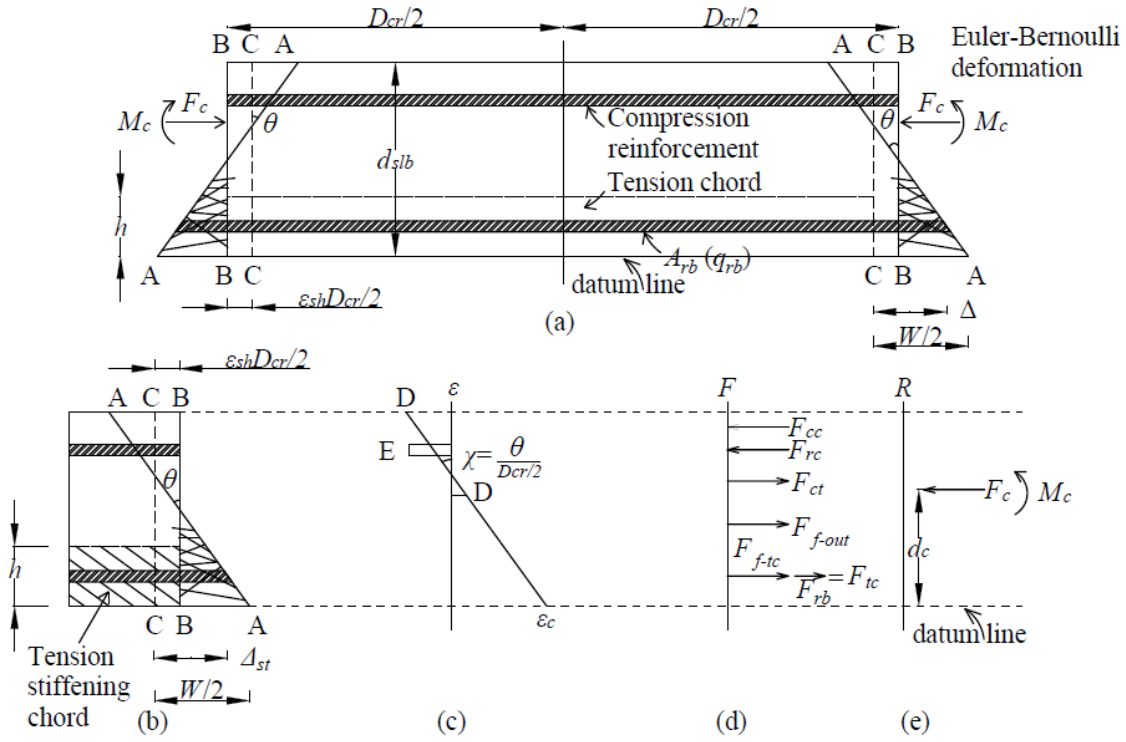


**Fig. 10.** Segmental analysis of RC component

The segment in Fig. 10(a) is subjected to an axial force $F_c$, which is the prestressing force in Fig. 4(e), and constant sagging moment $M_c$. The concrete has a shrinkage strain $\varepsilon_{sh}$ which if unrestrained would move the concrete end face *B-B* by $\varepsilon_{sh}D_{cr}/2$ to *C-C*. The RC slab has compression reinforcement at the top and fibres bridge the flexural cracks shown either side. The axial force in the tension chord of depth $h$ in Fig. 10(a) can be derived from a tension chord analysis as in Fig. 3(d) where there are only reinforcing bars, that is there is no profiled sheet, and which can cope with time effects such as creep and shrinkage (Sturm et al. 2020; Visintin et al. 2018). The analysis of this chord between cracks gives the relationship between the axial force $P_f$ plus $P_{rb}$ and $\Delta$ for use in the analysis in Fig. 10.

An Euler-Bernoulli deformation A-A is applied to both end faces in Fig. 10(a) which causes a rotation $\theta$. As the rotation is gradually increased, a flexural crack will occur with a half crack width $W/2$ at the base. This has been shown measured from the shrinkage face C-C when the concrete is fully unrestrained. The width of the crack at the level of the tension reinforcement is shown as $\Delta$.

The displacement on the RHS of Fig. 10(a) is shown in Fig. 10(b). The deformation in the concrete in compression between C-C and A-A divided by $D_{cr}/2$ gives the compressive strain in the concrete D-D in Fig. 10(c); from the concrete material moduli, the compressive distribution of stress and consequently the resulting compressive force $F_{cc}$ in Fig. 10(d) can be determined. Similarly for the concrete in tension where the resulting force is shown as $F_{ct}$. As there is no shrinkage in the compression reinforcement, the strain in the compression reinforcement is due to the deformation between A-A in Fig. 10(b) and B-B; divided by its length $D_{cr}/2$ gives the strain E in Fig. 10(c) and from the modulus the force $F_{rc}$ in Fig. 10(d). The remaining forces occur in the cracked region and so are controlled by PI behaviour and cannot be determined from their moduli. Within the tension chord in Fig. 10(b), the reinforcement and the fibres slip relative to the crack face by $\Delta$. The total force in the tension chord, which is shown as $F_{tc}$ in Fig. 10(d), is a tension stiffening property which depends on $P/\Delta$ as in Fig. 3(d). Within the cracked region in Fig. 10(b) and outside the bounds of the tension chord, the force in the fibres depends on the width of the crack which varies from zero to $W/2$.

For a given rotation $\theta$ in Fig. 10(b) and consequently curvature in Fig. 10(c), it is a question of varying $\varepsilon_c$ until the resultant force is $F_c$. After which, moments of the forces in Fig. 10(d) can be taken about any arbitrary level $d_c$ in Fig. 10(e) to get $M_c$. This approach can be used to derive the RC mechanical properties in Fig. 7. The same approach could be used to derive the mechanical properties of the profiled component in Fig. 8. However in this case as there is no partial-interaction, consequently the PI displacement component of the analysis in Fig. 10(b) are not required and the analysis can start from Fig. 10(c) which is a standard $M/\chi$ analysis.

## PI partially debonded composite member global analysis

The fully debonded sagging member analysis described above applies to a member that is fully IC debonded as in Fig. 5(c) 'fully IC debonded'. This is a safe and usually conservative analysis of the profiled slab as non-debonded regions can only increase the strength and stiffness. It may be worth noting, that for the profiled slabs used to validate this numerical model in Section '*Beneficial effects of fibres*', $P_{IC}$ is 20% of the yield capacity of the profiled sheet that is IC debonding will occur well before yield and at serviceability loads. However, the fully debonded analysis can be used to quantify the extent of debonding as in Fig. 5 'partially IC debonded' and the behaviour of the slab for this extent of debonding.

In this case, the analysis depicted in Fig. 5(a) has to start at mid-span where the global slip is zero and it is a question of finding the debonded length $L_{dbd}$, that is where the slip is also zero towards the other end of the slab as in Fig. 5(c). This can be done by ensuring longitudinal compatibility between the profiled sheet and the RC member over the debonded length $L_{dbd}$. That is, at any convenient datum level such as that shown in Fig. 6(a) and for a given distribution of applied moment, the longitudinal extension of the RC member over the debonded region in Fig. 5(c) has to be equal to the longitudinal extension of the profiled member over the debonded region. Details of the analysis are given elsewhere for fibre reinforced polymer plates bonded to the soffit of RC beams (Oehlers 2006; Oehlers et al. 2016).

## Hogging regions

The above approach for the member analysis of beams under sagging moments can be applied directly to beams under hogging moments. For the hogging region, the displacements on the LHS of Fig. 5(a) can be swivelled around a vertical axis such that the top of the deformation shows expansion and the bottom contraction. In the analysis in Fig. 6, the RC concrete component now goes into overall tension and the profile sheet into overall compression. The interface shear flow is still $q_{frc}$. The mechanical properties required in the member analysis for hogging regions can also be determined from the segmental analysis illustrated in Fig. 10(a) for a sagging slab. For the hogging region, the top reinforcement now goes into tension such that it now comprises the tension cord.

## Beneficial effects of fibres

It has been shown directly from tests that the two major effects of fibres are to enhance the bond-slip ($q_{pr}$) between the profiled sheet and the adjacent concrete and to transfer tensile stresses across cracks ($\sigma_f$) (Chen et al. 2022a). These major material benefits due to the inclusion of fibres affects the local behaviour of composite profiled slabs such as the crack spacing and crack widths and the global behaviour such as the profiled sheet slip and composite slab stiffness. In order to illustrate these benefits, the above numerical model is used to analyse tests of composite profiled slabs in both sagging (*+ve*) and hogging (*-ve*) regions (Chen et al. 2022b).

These test results (Chen et al. 2022b) give full details of all the geometric and material properties such as shrinkage strains which were used in the numerical analyses, and as this

paper is on serviceability, the test results are compared only up to the onset of reinforcing bar yield. Three profiled slabs were tested in sagging: one slab SS0 had 0% fibres; another SS1 had 1% fibres; and the third SS2 had 2% fibres. Three profiled slabs were also tested in hogging: one slab SH0 had 0% fibres; another SH1 had 1% fibres; and the third SH2 had 2% fibres.

### *Crack spacing*

The theoretical model crack spacing can be determined from the tension chord analysis depicted in Figs. 3(b) and (c); it is worth bearing in mind that crack spacing is a semirandom phenomenon (Visintin et al. 2013) and that these analyses give the minimum crack spacing. The experimental and model primary crack spacings are compared in Table 1 where Row 1 is the fibre content in the profiled slabs that were tested which ranged from 0%, that is no fibres, to 2% of fibres. To allow for the scatter of the material properties in the model analysis, the model has been run using the upper bound (UB) to the material properties as well as the lower bound (LB) and also average values (AVG) and the results listed under these headings in Row 2.

**Table 1.** Primary crack spacing

| (1) Fibre contents | | 0% | | | 1% | | | 2% | | |
|---|---|---|---|---|---|---|---|---|---|---|
| (2) Model material properties | | UB | AVE | LB | UB | AVE | LB | UB | AVE | LB |
| Sagging crack spacing (mm) | (3) Exp | | 249 | | | 192 | | | 165 | |
| | (4) Model | 175 | 182 | 210 | 149 | 150 | 187 | 129 | 130 | 133 |
| Hogging crack spacing (mm) | (5) Exp | | 113 | | | 160 | | | 89 | |
| | (6) Model | 105 | 110 | 129 | 84 | 88 | 89 | 71 | 73 | 76 |

The experimental crack spacings for the sagging beam tests are listed in Row 3 of Table 1. It can be seen that they range from 249 mm for members without fibres to 165 mm for members with 2% fibres. Those for the model analysis are listed in Row 4. They too reduce with increasing fibre content. Importantly they are a lower bound to the experimental results as would be expected, as the theoretical model gives the minimum crack spacing, and also, importantly, they reduce with fibre content.

The experimental crack spacing for the hogging beam tests are listed in Row 5 of Table 1 and those for the model in Row 6. The results from the model in Row 6 follow the expected trends of reducing with fibre content and being a lower bound to the experimental results. In the experimental results, the increase in crack spacing from 113 mm to 160 mm with an increasing fibre content is an anomaly that can be accounted for by the random nature of this mechanism. On further increasing the fibre content the spacing reduces from 160 mm to 89 mm that is they fall back into the expected trend.

The parameters that affect crack spacing are illustrated from the results of the model analysis in Fig. 11. The parameters that affect the crack spacing are: the shear flow strength between the profiled sheet and the adjacent concrete where $q_{pr\text{-}0}$ is the shear flow strength for concrete without fibres and $q_{pr\text{-}2}$ that for concrete with 2% fibres; similarly for the reinforcing bars where $q_{rb\text{-}0}$ is the shear flow strength for concrete without fibres and $q_{rb\text{-}2}$ that for concrete with 2% fibres; the remaining parameter is the fibre stress across a crack where $\sigma_{f\text{-}0}$ signifies zero fibre stress that is the stress without fibres and $\sigma_{f\text{-}2}$ that for 2% fibres.

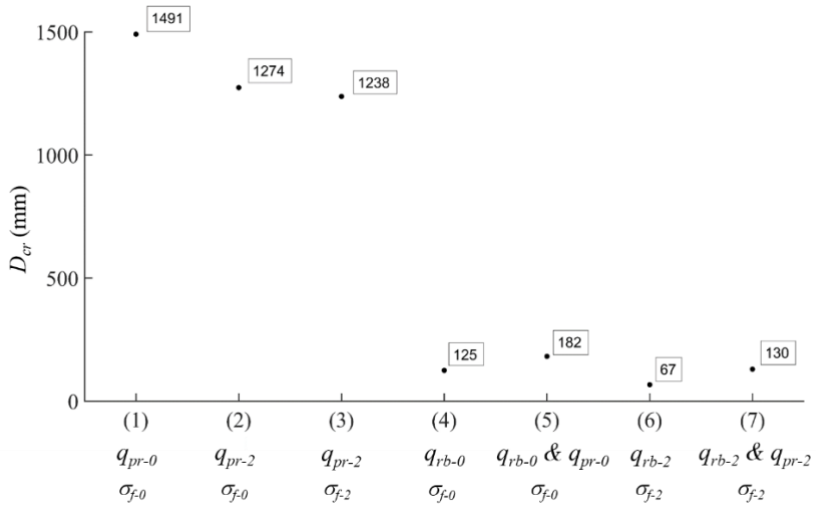


**Fig. 11.** Parameters that affect crack spacing

From the tension chord analysis in Fig. 3 with just the profiled sheet and in concrete without fibres, the crack spacing was 1491 mm which would suggest that one very wide crack occurs. This is shown in Column 1 in Fig. 11 where $q_{pr\text{-}0}$ signifies the shear flow strength with concrete without fibres and $\sigma_{f\text{-}0}$ signifies no fibres across the cracks. In Column 2, $q_{pr\text{-}0}$ was increased to that of concrete with fibres that is $q_{pr\text{-}2}$ but $\sigma_{f\text{-}0}$ remained at zero to determine the effect of changing the shear flow strength by itself. This increase in shear flow strength by itself reduced

the crack spacing to 1274 mm. Fibre stresses $\sigma_{f\text{-}2}$ were now added in Column 3 which further reduced the crack spacing to 1238 mm.

Repeating the above analyses just with the reinforcing bars gave a crack spacing of 125 mm for concrete without fibres in Column 4 in Fig. 11. Comparing this with 1491 mm in Column 1 shows that the much greater bond strength of the reinforcing bars compared to that of the profiled sheet reduces the crack spacing by an order of magnitude which would suggest that some reinforcing bars are essential in controlling the crack spacing and consequentially the crack widths. Adding the profiled sheet to the analysis in Column 5 increased the crack spacing slightly from 125 mm to 182 mm. This was unexpected as increasing the bond strength reduces the crack spacing but in this case the bond strength is increased by adding more reinforcement which affects the slip-strain. Adding fibres to the concrete in Column 6 further reduced the crack spacing from 125 mm to 67 mm. Similarly adding fibres in Column 7 reduces the crack spacing from 182 mm to 130 mm

### *Crack widths*

Having derived the crack spacing from Figs. 3(b) and 3(c), the crack widths can be derived from Fig. 3(d). The theoretical results, shown as unbroken lines, are compared with the experimental results for the sagging slabs (Chen et al. 2022b), shown as a crosses, in Figs. 12(a) to (b). Bearing in mind the random nature of crack spacing and crack widths there would appear to be good correlation between the model results and the experimental results. It can be seen that adding fibres from Figs. 12(a) to (c) can reduce the crack width by an order of magnitude, the consequences of which is an improved member durability. Similar results appear for the hogging slabs in Figs. 12(d) to (f).

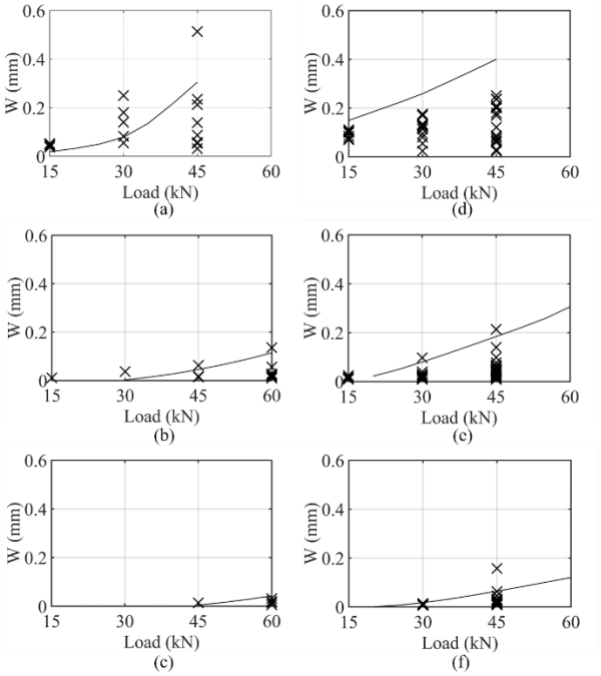


**Fig. 12.** Crack widths: (a) 0%-Sagging; (b) 1%-Sagging; (c) 2%-Sagging; (d) 0%-Hogging; (e) 1%-Hogging; and (f) 2%-Hogging

### *Fibre tensile force*

The forces acting across a flexural crack can be determined from the segmental analysis in Fig. 10. The tensile force in the uncracked concrete is shown as $F_{ct}$, that in the tension reinforcing bars as $F_{rb}$ and the total fibre force $F_f$ is the sum of the component within the tension chord $F_{f\text{-}tc}$ and that outside the tension chord $F_{f\text{-}out}$. These forces are plotted in Fig. 13(a) with increasing curvature; in the subscripts, 0, 1 and 2 refer to the % fibre in the concrete.

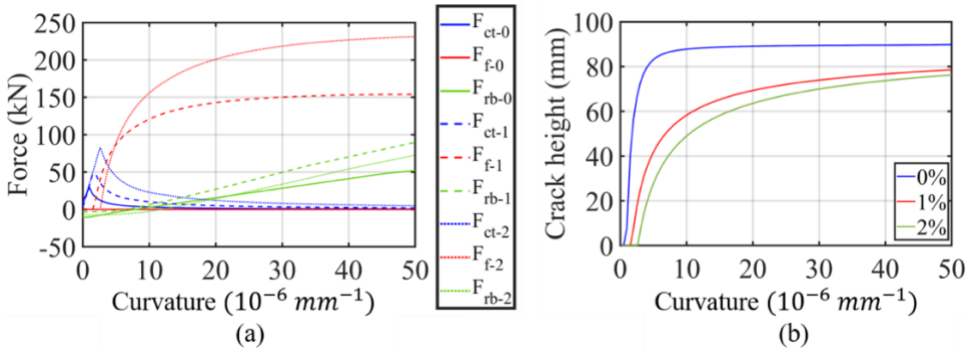


**Fig. 13.** Maintenance of fibre forces: (a) force contribution; and (b) crack height

As can be seen in Fig. 13(a), the tensile forces $F_{ct}$ rapidly asymptote towards zero as the curvature increases and consequently has negligible contribution. The tensile force in the

reinforcing bar $F_{rb}$ gradually increases with curvature and with fibre content. However, the fibre force $F_f$ first rapidly increases with curvature and then is maintained and, furthermore, is much larger than that in the tensile reinforcement $F_{rb}$ and as would be expected increases with fibre content. Hence the fibre tensile stress makes a major contribution to the flexural resistance.

Material tensile tests on fibre concrete (Chen et al. 2022b) with straight fibres, as used in these tests, clearly show that the tensile strength $\sigma_f$ is at a maximum when the flexural crack first forms, that is at zero crack width, after which $\sigma_f$ reduces as the fibres pull out. So it is surprising that the fibre force $F_f$ is maintained as in Fig. 13(a). The reason for this is explained in Fig. 13(b) where it can be seen that for concrete without fibres, 0%, the height of the flexural crack remains fairly constant with increased curvature. However on adding fibres, the height of the crack is reduced and gradually increases with curvature. Hence as the curvature increases, the height of the crack increases allowing more fibres to go into tension thereby adding to $F_f$ to offset the reduction to $F_f$ due to pull out. Hence at serviceability the fibre forces can be relied upon.

### *Profiled sheet end slip*

The experimental slips at the ends of the profiled sheets, such as $S_1$ in Fig. 5(c), are plotted in Fig. 14; one side is labelled Exp-SW and the other Exp-NW. When testing a symmetrically loaded beam, it is the weaker of the two sides which fails. The results from the numerical model are also plotted and as can be seen and expected they follow the weaker of the two sides.

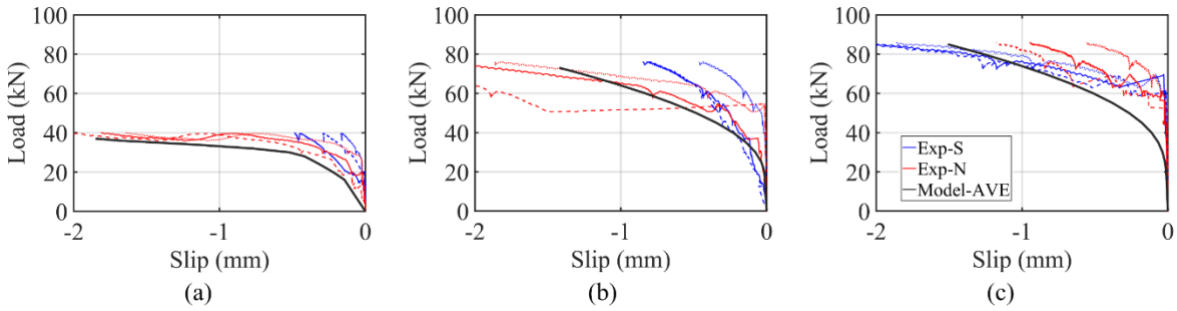


**Fig. 14.** Profile end slip: (a) 0%; (b) 1%; and (c) 2%

### *Composite slab load/deflections*

The experimental load/deflection plots, EXP, of the sagging members are shown in Fig. 15(a) with the numerical model results (M) from the member analysis in Fig. 5. It can be seen that there is good correlation throughout. The addition of fibres significantly increases the stiffness. The same can be said for the hogging members in Fig. 15(b).

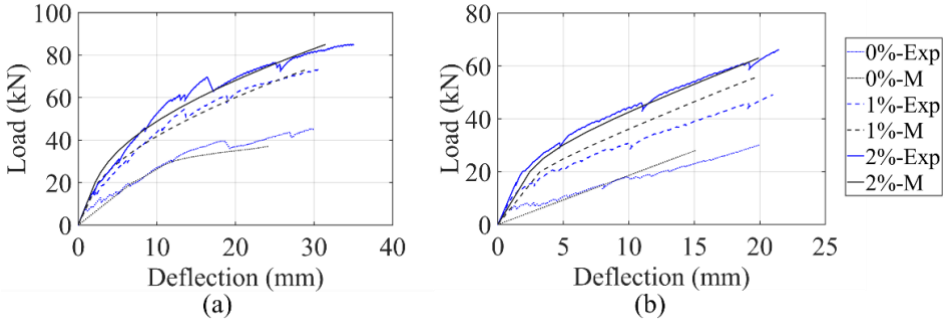


**Fig. 15.** Deflection of profile member: (a) Sagging; and (b) Hogging

## Conclusions

A rational partial-interaction mechanics model has been developed that can quantify the serviceability benefits of using UHPFRC in profiled slabs. The model can be used for any type of profiled sheet and for any type and quantity of fibres and hence will help in the development of new systems. The model can be used to quantify regions of the slab in which the profiled sheet has debonded. It is shown in the debonded region that the axial forces in the profiled sheet act as prestressing forces to the RC component. Whereas in the non-debonded region the profiled sheet acts as tension reinforcement. And the model results in terms of crack spacing, crack width, load-deflection performance all showed good correlation with experimental results for both sagging and hogging slab tests.

From tension chord mechanics, the shear flow strength of the profile and that of the reinforcing bars act together in the development of flexural cracks. As fibres also enhance the shear flow strength in the profiled sheet and reinforcing bars, this further reduces the crack spacings and crack widths. Furthermore, as fibres bridge cracks, this further reduces the crack spacing and crack widths. Hence it can be seen that there are three mechanical reasons why fibres and profiled slabs reduce crack widths which will lead to higher stiffness, flexural resistance and durability.

It has been shown that fibres provide a substantial amount of the tensile force which can be much bigger than that provided by the tension reinforcement. Unexpectedly, it was found that this force is maintained as the crack widens because the depth of the crack increases with curvature hence increasing the fibre force which offsets the loss associated with crack widening. Hence fibres contribute significantly to the serviceability of steel UHPC composite slabs.

## Data Availability Statement

Some or all data, models, or code that support for the findings of this study are available from the corresponding author upon reasonable request.

## Acknowledgements

This material is based upon work supported by the Australian Research Council Discovery Project 190102650. The authors acknowledge the financial support from Australian Government Research Training Program Scholarship awarded for the first author.

## Notation

The following symbols are used in this paper:

$A_{pr}$ total cross-sectional area of profiled sheet within $w_{slab}$
AVG average material properties
comp compressive stresses
cont. contraction
$D_{cr}$ longitudinal spacing of flexural cracks
$d_b$ reinforcing bar diameter
$d_c$ arbitrary depth in concrete component from arbitrary datum line and at which moments are taken
$d_{pr}$ depth of profiled sheet
$d_s$ arbitrary depth in profile sheet component measured from datum line and at which moments are taken

$d_{slb}$ depth of profiled slab

$ds/dx$ slip-strain; $\varepsilon_c$ - $\varepsilon_s$

exp. expansion; experimental

$(EI)_c$ elastic flexural rigidity of RC component

$(EI)_s$ elastic flexural rigidity of profile component

$e$ eccentricity of axial loads; $d_c$ - $d_s$

$F$ axial or longitudinal force acting on profiled slab

$F_c$ Force acting on concrete component

$F_{cc}$ Force of concrete in compression

$F_{ct}$ Force of concrete in tension

$F_{ct\text{-}x}$ $F_{ct}$ in concrete with x% fibres

$F_f$ $F$ of fibres; total fibre force

$F_{f\text{-}x}$ $F_f$ in concrete with x% fibres

$F_{f\text{-}out}$ force in fibres outside tension chord

$F_{f\text{-}tc}$ force in fibres in tension chord

$F_{tc}$ total force in tension chord

FI full interaction

$F_{rb}$ force in tension reinforcing bar

$F_{rb\text{-}x}$ $F_{rb}$ in concrete with x% fibres

$F_{rc}$ $F$ of reinforcement in compression

$F_s$ $F$ acting on profiled sheet component

$f_{ct}$ tensile strength of concrete

$h$ depth of tension chord

$h_{ps}$ depth of profiled slab

IC intermediate crack

$L$ half span length of profiled slab

$L_{dbd}$ debonded length

$L_e$ element length

$L_{emb}$ embedment length

LB lower bound material properties

LHS left hand side

$M$ moment; model

$M_c$ moment acting on concrete component

$M_s$ moment acting on profiled sheet component

$n$ element number

$P$ axial force

$P_{emb}$ force to cause slip $S_{emb}$ of embedded reinforcement

$P_f$ tensile force in fibres

$P_{frc}$ frictional force

$P_{pr}$ tensile force in profiled sheet

$P_{IC}$ IC debonding resistance

$P_{pr\text{-}yld}$ yield strength of profiled sheet

$P_{rb}$ tensile force in reinforcing bars

PI partial-interaction; slip across an interface

$Q$ longitudinal force component

$q$ shear flow force

$q_{bar}$ shear flow strength of an individual reinforcing bar; $\pi d_b \tau$

$q_{frc}$ frictional component of $q_{pr}$

$q_{frc\text{-}c}$ $q_{pr}$ acting on concrete component

$q_{frc\text{-}s}$ $q_{pr}$ acting on steel profiled sheet component

$q_{max}$ maximum $q_{pr}$ of chemical bond

$q_{pr}$ shear flow strength of profiled sheet of area $A_{pr}$; $P_{emb}/L_{emb}$ of $A_{pr}$

$q_{pr\text{-}x}$ $q_{pr}$ in concrete with x% fibres

$q_{rb}$ shear flow strength of all tension reinforcing bars within $w_{slab}$; sum of all $q_{bar}$

$q_{rb\text{-}x}$ $q_{rb}$ in concrete with x% fibre

$R$ stress resultants; stress resultant profile

RC reinforced concrete

RHS right hand side

$S$ interface slip

$S_{emb}$ $S$ of embedded reinforcement in bond test

$S_1$ slip at end of profiled sheet

ten tensile stresses

UB upper bound material properties

UHPFRC ultra high performance fibre reinforced concrete

$W$ crack width

$w_{slab}$ width of profiled slab being analysed

| | |
|---|---|
| X% | X% fibre concrete |
| $\chi$ | curvature |
| $\varepsilon$ | strain; strain profile |
| $\varepsilon_c$ | strain in concrete component at arbitrary level |
| $\varepsilon_s$ | strain in profiled sheet component at arbitrary level |
| $\varepsilon_{sh}$ | shrinkage strain |
| $\Delta$ | reinforcement slip at crack face; half crack width |
| $\delta$ | displacement; displacement profile |
| $\delta_c$ | Euler-Bernoulli displacement of reinforced concrete component |
| $\delta_p$ | Euler-Bernoulli displacement of profiled sheet component |
| $\delta_1$ | slip at $q_{max}$ |
| $\theta$ | Euler-Bernoulli rotation |
| $\sigma_c$ | concrete stress |
| $\sigma_f$ | fibre stress |
| $\sigma_{f\text{-}x}$ | $\sigma_f$ in concrete with x% fibres |
| $\tau$ | interface bond stress or strength |

## References


Abas, F. M., M. A. Bradford, S. J. Foster, and R. I. Gilbert. 2016. "Shear-Bond Behaviour of Steel-Fibre Reinforced Concrete (SFRC) Composite Slabs with Deep Trapezoidal Decking: Experimental Study." *Compos. Constr. Steel Concr. VII*. 561-580. https://doi.org/10.1061/9780784479735.043

Abas, F. M., R. I. Gilbert, S. J. Foster, and M. A. Bradford. 2013. "Strength and serviceability of continuous composite slabs with deep trapezoidal steel decking and steel fibre reinforced concrete." *Eng. Struct*. 49: 866-875. https://doi.org/10.1016/j.engstruct.2012.12.043

Ackermann, F. P., and J. Schnell. 2011. "Steel Fibre Reinforced Continuous Composite Slabs." *Compos. Constr. Steel Concr. VI*. 125-137. https://doi.org/10.1061/41142(396)11

Akhnoukh, A. K., and C. Buckhalter. 2021. "Ultra-high-performance concrete: Constituents, mechanical properties, applications and current challenges." *Case Stud. Constr. Mater*. 15: e00559. https://doi.org/10.1016/j.cscm.2021.e00559

Chen, S., P. Visintin, and D. J. Oehlers. 2022a. "Bond between very-high and ultra-high performance fibre reinforced concrete and profiled deck sheeting." *J. Build. Eng*. 52: 104426. https://doi.org/10.1016/j.jobe.2022.104426

Chen, S., P. Visintin, and D. J. Oehlers. 2022b. “Experimental investigation of the influence of fibre content on the flexural performance of simply supported and continuous steel/UHPC composite slabs.” Submitted to *Steel Compos. Struct.*

DiFrancia, C., T. C. Ward, and R. O. Claus. 1996. “The single-fibre pull-out test. 1: Review and interpretation.” *Compos. Part A Appl.* 27 (8): 597-612. https://doi.org/10.1016/1359-835X(95)00069-E

Gholamhoseini, A., A. Khanlou, G. MacRae, S. Hicks, A. Scott, and C. Clifton. 2018. “Short-term behaviour of reinforced and steel fibre–reinforced concrete composite slabs with steel decking under negative bending moment.” *Adv. Struct. Eng*. 21 (9)1288-1301. https://doi.org/10.1177/1369433217739710

Gholamhoseini, A., A. Khanlou, G. MacRae, A. Scott, S. Hicks, and R. Leon. 2016. “An experimental study on strength and serviceability of reinforced and steel fibre reinforced concrete (SFRC) continuous composite slabs.” *Eng. Struct*. 114: 171-180. https://doi.org/10.1016/j.engstruct.2016.02.010

Hadigheh, S., R. Gravina, and S. Setunge. 2015. “Identification of the interfacial fracture mechanism in the FRP laminated substrates using a modified single lap shear test set-up.” *Eng. Fract. Mech.* 134: 317-329. https://doi.org/10.1016/j.engfracmech.2014.12.001

Hamoda, A., K. Hossain, K. Sennah, M. Shoukry, and Z. Mahmoud. 2017. “Behaviour of composite high performance concrete slab on steel I-beams subjected to static hogging moment.” *Eng. Struct.* 140: 51-65. https://doi.org/10.1016/j.engstruct.2017.02.030

Hassan, A., S. Jones, and G. Mahmud. 2012. “Experimental test methods to determine the uniaxial tensile and compressive behaviour of ultra high performance fibre reinforced concrete (UHPFRC).” *Constr. Build. Mater*. 37: 874-882. https://doi.org/10.1016/j.conbuildmat.2012.04.030

Knight, D., P. Visintin, D. J. Oehlers, and M. Jumaat. 2013. “Incorporating residual strains in the flexural rigidity of RC members with varying degrees of prestress and cracking.” *Adv. Struct. Eng.* 16 (10): 1701-1718. https://doi.org/10.1260/1369-4332.16.10.1701

Lin, W., T. Yoda, and N. Taniguchi. 2014. “Application of SFRC in steel–concrete composite beams subjected to hogging moment.” *J Constr. Steel Res*. 101: 175-183. https://doi.org/10.1016/j.jcsr.2014.05.008

Marchand, P., F. Baby, A. Khadour, T. Battesti, P. Rivillon, M. Quiertant, H. H. Nguyen, G. Généreux, J. P. Deveaud, and A. Simon. 2016. “Bond behaviour of reinforcing bars in UHPFRC: Experimental investigation.” *Mater. Struct*. 49: 1979-1995. https://doi.org/10.1617/s11527-015-0628-0

Marimuthu, V., S. Seetharaman, S. A. Jayachandran, A. Chellappan, T. Bandyopadhyay, and D. Dutta. 2007. “Experimental studies on composite deck slabs to determine the shear-bond characteristic (m–k) values of the embossed profiled sheet.” *J. Constr. Steel Res*. 63 (6): 791-803. https://doi.org/10.1016/j.jcsr.2006.07.009

Naaman, A. E., G. G. Namur, J. M. Alwan, and H. S. Najm. 1991. “Fiber pullout and bond slip. I: Analytical study.” *J. Struct. Eng*. 117 (9): 2769-2790. https://doi.org/10.1061/(ASCE)0733-9445(1991)117:9(2769)

Nguyen, C. L., and C. K. Lee. 2021. “Flexural behaviours of Engineered Cementitious Composites–High strength steel composite beams.” *Eng. Struct*. 249: 113324. https://doi.org/10.1016/j.engstruct.2021.113324

Oehlers, D. J. 2006. “FRP plates adhesively bonded to reinforced concrete beams: Generic debonding mechanisms.” *Adv. Struct. Eng*. 9 (6): 737-750. DOI: 10.1260/136943306779369482.

Oehlers, D. J., P. Visintin, and W. Lucas. 2016. “Fundamental mechanics governing FRP-retrofitted RC beams with anchored and prestressed FRP plates.” *J. Compos. Constr*. 20 (6): 04016047. https://doi.org/10.1061/(ASCE)CC.1943-5614.0000710

Oehlers, D. J., P. Visintin, and W. Lucas. 2016. “Flexural strength and ductility of FRP-plated RC beams: Fundamental mechanics incorporating local and global IC debonding.” *J. Compos. Constr*. 20 (2): 04015046. https://doi.org/10.1061/(ASCE)CC.1943-5614.0000610

Petkevičius, M., and J. Valivonis. 2010. “Analysis of bending capacity of composite steel-concrete slabs with steel fiber reinforced concrete.”

Qi, J., Z. Cheng, J. Wang, and Y. Tang. 2020. “Flexural behavior of steel-UHPFRC composite beams under negative moment.” *Structures.* 24: 640-649. https://doi.org/10.1016/j.istruc.2020.01.022

Shafieifar, M., M. Farzad, and A. Azizinamini. 2017. “Experimental and numerical study on mechanical properties of Ultra High Performance Concrete (UHPC).” *Constr. Build. Mater*. 156: 402-411. https://doi.org/10.1016/j.conbuildmat.2017.08.170

Sturm, A. B., P. Visintin, D. J. Oehlers, and R. Seracino. 2018. “Time-dependent tension-stiffening mechanics of fiber-reinforced and ultra-high-performance fiber-reinforced concrete.” *J. Struct. Eng.* 144 (8): 04018122. https://doi.org/10.1061/(ASCE)ST.1943-541X.0002107

Sturm, A. B., and P. Visintin. 2018. “Local bond slip behavior of steel reinforcing bars embedded in ultra high performance fibre reinforced concrete.” *Struct. Concr*. 20 (1): 108-122. http://doi.org/10.1002/suco.201700149.

Sturm, A. B., P. Visintin, and D. J. Oehlers. 2020. “Blending fibres to enhance the flexural properties of UHPFRC beams.” *Constr. Build. Mater*. 244 :118328. https://doi.org/10.1016/j.conbuildmat.2020.118328

Visintin, P., D. J. Oehlers, and M. Haskett. 2013. “Partial-interaction time dependent behaviour of reinforced concrete beams,” *Eng. Struct.* 49: 408-420. https://doi.org/10.1016/j.engstruct.2012.11.025

Visintin, P., A. B. Sturm, M. S. Mohamed Ali, and D. J. Oehlers. 2018. “Blending macro-and micro-fibres to enhance the serviceability behaviour of UHPFRC.” *Aust. J. Civ. Eng.* 16 (2): 106-121. https://doi.org/10.1080/14488353.2018.1463608.

Visintin, P., M. S. Mohamad Ali, T. Xie, and A. B. Sturm. 2018. “Experimental investigation of moment redistribution in ultra-high performance fibre reinforced concrete beams.” *Constr. Build. Mater.* (166): 433-444. https://doi.org/10.1016/j.conbuildmat.2018.01.156

Wang, Z., J. Yan, Y. Lin, F. Fan, and Y. Yang. 2020. “Mechanical properties of steel-UHPC-steel slabs under concentrated loads considering composite action.” *Eng. Struct.* 222: 111095. https://doi.org/10.1016/j.engstruct.2020.111095

Wille, K., S. El-Tawil, and A. E. Naaman. 2014. “Properties of strain hardening ultra high performance fiber reinforced concrete (UHP-FRC) under direct tensile loading.” *Cem. Concr. Compos.* 48: 53-66. https://doi.org/10.1016/j.cemconcomp.2013.12.015

Xiao, J. L., M. Zhou, J. G. Nie, T. Y. Yang, and J. S. Fan. 2021. “Flexural behavior of steel-UHPC composite slabs with perfobond rib shear connectors.” *Eng. Struct.* 245: 112912. https://doi.org/10.1016/j.engstruct.2021.112912

Yoo, D. Y., H. O. Shin, J. M. Yang, and Y. S. Yoon. 2014. “Material and bond properties of ultra high performance fiber reinforced concrete with micro steel fibers.” *Compos. B. Eng.* 58: 122-133. https://doi.org/10.1016/j.compositesb.2013.10.081

Yu, J., B. Zhang, W. Chen, and J. He. 2020. “Experimental and multi-scale numerical investigation of ultra-high performance fiber reinforced concrete (UHPFRC) with different coarse aggregate content and fiber volume fraction.” *Constr. Build. Mater.* 260: 120444. https://doi.org/10.1016/j.conbuildmat.2020.120444

Zhang, P., R. Hu, X. Zou, Y. Liu, Q. Li, G. Wu, and S. A. Sheikh. 2021. “Experimental study of a novel continuous FRP-UHPC hybrid beam.” *Compos. Struct.* 261: 113329. https://doi.org/10.1016/j.compstruct.2020.113329

# CHAPTER 5 – Analytical Solutions

## 5.1 Introduction

In this chapter, a mechanics-based analytical solution is developed to determine a general expression for the curvature of each segment and then define the load-deflection behaviour of a composite slab under the serviceability behaviour. It is developed from the previously developed numerical analysis (Chapter 4) following the same assumptions and approach. The process of numerical analysis includes determining the local behaviour $M/\chi$ of reinforced concrete and profiled deck firstly and then iterating the curvature guess to reach moment equilibrium, it is a time-consuming process and the accuracy of the results is dependent on the mesh size. Hence, a simpler and quicker way is required for composite slab design which can skip repeated moment-curvature determination and elemental iteration. The significance of this approach lies in its ability to directly obtain the curvature of each segment and then deflection through analytical solution which enable the development of the design guidance of composite slab in service limit state with considering non-uniform shrinkage strain. Hence, the current study will consider ultra-high-performance fibre-reinforced concrete (UHPFRC) as one component of composite slabs with considering concrete strain-based stress into the analysis while crack-opening based stress (macro-cracking) will not be considered in the scope. Throughout the entire process, full interaction (FI) between concrete and reinforced bar and partial interaction (PI) between concrete and profiled deck will be applied into the analysis.

## 5.2 Literature review

In the following section, a summary of current analytical solutions for the design of steel concrete composite is presented.

### *5.2.1 Composite slab*

Gholamhoseini et al. used the transformed section of reinforced concrete to represent that of whole composites, it also considered long-term effect (shrinkage and creep strain) to generate long-term deflection results [1]. Similar processes were presented in other studies which categorised concrete uncracking and concrete cracking conditions. For each condition, a corresponding moment of intertia of the entire composite slab was determined by an empirical process. The analytical solution for uncracking and for cracking were compared with test results separately to figure out which one can better fit with experimental results [2].

Besides the aforementioned second moment inertia approaches, there is another method that assumes the concrete compressive strain reach to the crushing strain and then achieves a force equilibrium comprising of concrete compression, concrete in tension, profiled deck in tension and reinforced bar in tension, all of which are dependent on the composite slab design. After determining the magnitude of each force component, moments are taken at the centroid of the composite section to determine the moment capacity of composite slab [3-6]. Theoretically, the flexural rigidity can be determined from this extreme condition, and then a linear relationship between curvature and moment can be used to calculate the deflection of composite slab.

The principle of virtual work is applied for studies to determine the stress, strain, internal force and then deflection relationship of composite slab, taking into account shrinkage and creep strain while considering full interaction between the concrete and steel deck which means there no slip occurred between contact surface [7-9].

#### *5.2.2 Composite beam:*

Nguyen et al. present the development of an analytical approach for composite beams comprising ultra-high-performance fibre-reinforced concrete (UHPFRC). This approach involves determining a unique curvature value which enables the concrete top strain to reach the maximum compressive strain and bottom of 'I' shape beam to reach yield strain, from which the corresponding moment and effective stiffness are derived arithmetically. With the effective flexural stiffness, a linear relationship between curvature and moment is also established, allowing for the empirical derivation of the deflection of the composite beam [10]. This approach was also applied in composite beam with lightweight aggregate concrete, and the model results were validated [11]. To develop design guidelines, Wu et al. introduced a method with application of partial interaction between concrete and steel components which allow for slip and axial force to be applied at each individual component separately [12]. In addition, there has been development in studying the relative slip between concrete and steel components, giving the expression for the slip distribution along the slab and imposing the boundary conditions to figure out the applicable solutions for slip results at each section [13, 14].

#### *5.2.3 Time-dependent behaviour:*

The application of impervious profiled deck in concrete steel composite structures makes a great impact on time-dependent performance of composite slab where the shrinkage strain is non-uniform distributed along the depth of composite slab. It is because the steel deck prevents egress of water at the bottom soffit of composite slabs which leads to shrinkage-induced tensile stress in concrete component of composite slabs resulting in reduction in cracking moment. Several researches focused on the studying impact of impervious profiled deck in composites and brought out bi-linear and parabolic shrinkage profiles which are derived from realistic experimental results by dividing individual element to equilibrium layers through the thickness of the profiled slab. These strain profiles have been validated and show more accurate results than uniform shrinkage profile [9, 15]. The parabolic shrinkage profiled with modification for estimating shrinkage and creep coefficient and then estimate deflection caused by time-dependent effect [16].

## 5.3 Research gap:

Learning from the previous research, there are limitations that should be addressed. The first limitation is that there is a lack of sufficient attention to investigation of analytical solutions for applications of ultra-high-performance fibre-reinforced concrete (UHPFRC) in composite slabs. The performance of composite slabs comprising of UHPFRC have been experimentally and numerically studied as exhibited in Chapter 3 and Chapter 4, respectively. While in the investigation of analytical solutions derivation, most studies focus on normal strength concrete. There are few studies focusing on analytical study of composite slab comprising of UHPFRC. Consequently, considering UHPFRC in the design of composite slabs is a favourable and advantageous alternative to conventional concrete. Another limitation is that some studies used the moment of inertia of reinforced concrete to represent that of composite slab which underestimate the stiffness and loading capacity of composite slabs. In addition, some investigations have disregarded the long-term effects in slab analysis [12] while shrinkage strain has been studied and shown to dominate the long-term flexural performance of composite slabs [16-18]. Furthermore, there are studies for composite slabs with assuming no relative slip occurs at the contact surfaces in serviceability limit state. This assumption implies the absence of bond force interaction with full-interaction at the contact surface and consequently ignores the axial force acting on concrete and steel deck components [12, 14, 18].

This chapter aims to propose an approach to derive analytical solutions for quickly estimating the flexural performance of composite slab in serviceability limit state. These analytical solutions can be used to assist in the future development guidelines for composite slab design. The proposed analytical approach provides a generic and comprehensive study for composite slabs which consider UHPFRC strain-hardening behaviour, the impact of non-uniform shrinkage and partial interaction (PI) behaviour between concrete and profiled deck. Furthermore, the accuracy of the analytical solutions will be validated by comparing with numerical results introduced in Chapter 4 for two loading configurations of central-concentrated point load and uniform distributed load (UDL).

**5.4 Methodology:**

This analytical approach for composite slabs proposed here is based on the same theory as numerical analysis presented in Chapter 4. It considers the modification of sectional moment-curvature analyses for both reinforced concrete and steel deck and accounts for non-uniform shrinkage strain and interfacial bond interaction in the analysis. Followed by achieving equilibriums for each segment then the curvature results can be determined. It aims to avoid iteration for neutral axis and curvatures and achieve the force equilibrium, the moment equilibrium and boundary conditions to connect these three components (concrete, internal reinforcement and steel deck) which are considered as an efficient approach to response the deflection results. This approach is not limited to specific types of profiled deck instead it can be applicable for any types of profiled deck, since the material properties of decking are pre-known ($d_s$, $I_s$, $A_s$, $E_s$). In the following sections, analytical solutions for composite slabs under central point load or uniform distributed load (UDL) will be derived.

Herein, concrete compressive strain-stress ($\varepsilon$-$\sigma$) relationship, steel components strain-stress relationship and bond shear connection between concrete and steel deck are all assumed linear-elastic. For concrete tensile properties, Sturm et al. [19] applied a piecewise linear tensile properties model for UHPFRC slabs analysis, consisting of (1) a linear-elastic region and (2) a strain-hardening region, as depicted in Fig. 1 for strain-based stress relationship. In this study, concrete macro-cracking is not under consideration because significant macro-cracking is generally not observed in the serviceability region. However, there is a clear limitation can be predicted that due to the concrete tensile strain is not linear-elastic when concrete reach to strain to cause micro-cracking, the neutral axis is not able to be determined using a closed form

solution and hence an iterative process is required to determine it. Hence, this is not the final solutions which means more work is required to simplify the analysis.

The following analysis is based on the uncracked and micro-cracked stages only, to allow for an investigation of whether there are any convenient forms of expressions that will allow for this analytical solution without empirical components still be possible to evaluate flexural performance of composite slabs. The current analysis is to achieve both force equilibrium and moment equilibrium to connect with three components.

Therefore, based on the tensile material properties of concrete, individual segmental analysis will be categorized into two conditions: uncracked and micro-cracked. The procedures about application of these two types of segmental analysis into slab analysis are, when a small loading is applied, the whole slab (all of the segments) experiencing uncracked status while the loading increasing, part of the segments which undertaking smaller moment remain uncracked but the remaining parts start to experience micro-cracking. In order to explain slab analysis more specifically, the following section will be divided into two parts consisting of slab uncracking stage analysis and slab micro-cracking stage analysis, respectively. At each stage, the procedures for determining the load-deflection results under the central point loading and UDL configurations will be demonstrated separately.

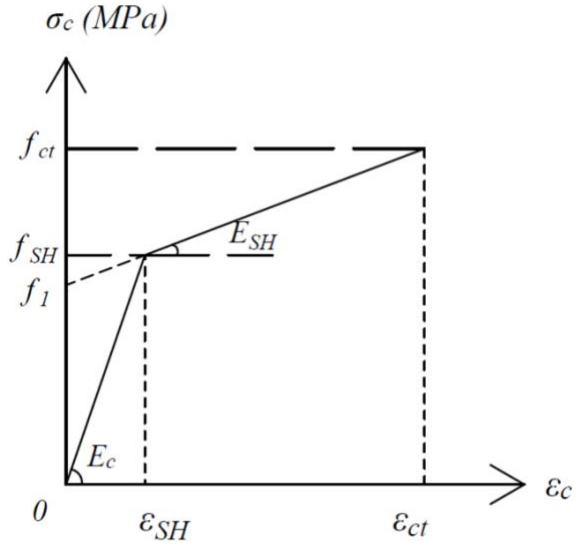


**Fig. 1.** UHPFRC tensile strain-stress relationship

As shown in **Fig. 1**, the UHPFRC tensile strain-stress relationship and the corresponding expressions for this bi-linear relationship

$$\sigma_c = \begin{cases} E_c(\varepsilon_c - \varepsilon_{sh}); \varepsilon_c < \varepsilon_{SH} \\ f_1 + E_{SH}(\varepsilon_c - \varepsilon_{sh}); \varepsilon_{SH} < \varepsilon_c < \varepsilon_{ct} \end{cases} \quad (1)$$

Where

$$f_1 = f_{SH} - E_{SH}\varepsilon_{SH} \quad (2)$$

$E_c$ is elastic modulus of concrete, $E_{SH}$ is strain-hardening modulus, $f_1$ is the stress intercepts, $f_{SH}$ stress causing micro-cracking. $\varepsilon_{sh}$ is the shrinkage strain, $\varepsilon_{SH}$ is the micro-crack strain, $\varepsilon_{ct}$ is macro-crack strain.

#### *5.4.1 Uncracking stage*

The cross-section of the composite slab is shown in **Fig. 2**, this figure can help to explain the following evaluation intuitively. As shown in **Fig. 2**, it shows the geometric property of composite slabs, the cross-section area of each components ($A_c$, $A_r$, $A_s$) and the centroid for concrete, internal reinforcement and steel decking ($d_c$, $d_r$, $d_s$) are consistently measured from the top fibre of composite slab.

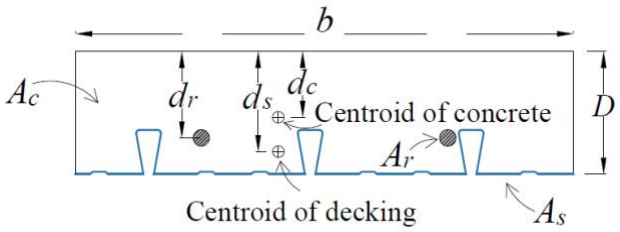


**Fig. 2.** Cross-section area for composite slab analysis

As we are considering the serviceability behaviour, internal reinforcement and steel deck are linear elastic. Hence, the stresses are given by

$$\sigma_s = E_s\varepsilon_s \quad (3)$$

$$\sigma_r = E_r\varepsilon_r \quad (4)$$

where $E$ is the elastic modulus and $\varepsilon$ is the strain. The subscripts are $s$ for steel deck and $r$ for the internal reinforcement.

Note that as the steel decking prevents drying from the bottom face of the section the shrinkage strain is non-uniform. This will be approximated by a linear distribution where

$$\varepsilon_{sh} = \varepsilon_{sh0} + \chi_{sh}y \quad (5)$$

where $\varepsilon_{sh0}$ is the shrinkage at the top surface of the concrete and $\chi_{sh}$ is the shrinkage curvature. ($\varepsilon_{sh0}$ is negative value input and $\chi_{sh}$ is positive value input)

Linear strain profiles are imposed in the concrete and steel where

$$\varepsilon_c = \varepsilon_r = \varepsilon_0 + \chi y \tag{6}$$

and $\varepsilon_0$ is the strain at the top surface of the concrete, $\chi$ is the curvature, $y$ is the depth measured from top surface.

The slip strain is the difference between the strain in the deck and the concrete and it can be expressed as

$$\frac{ds}{dx} = \varepsilon_s - \varepsilon_c \tag{7}$$

Rearranging Eq. (7) gets

$$\varepsilon_s = \varepsilon_c + \frac{ds}{dx} \tag{8}$$

The force in the concrete, steel and reinforcement is now given by Eq. (9, 11-12) as follows

$$N_c = \int^{A_c} \sigma_c \, dA = EA_c(\varepsilon_0 + \chi d_c - \varepsilon_{sh0} - \chi_{sh} d_c) = EA_c\left(\varepsilon_0 + \chi d_c - \bar{\varepsilon}_{sh_c}\right) \tag{9}$$

where

$$\bar{\varepsilon}_{sh_c} = \varepsilon_{sh0} + \chi_{sh} d_c \tag{10}$$

where $\bar{\varepsilon}_{sh_c}$ is the average shrinkage strain in the concrete section and $d_c$ is the centroid of concrete component

Similarly,

$$N_s = \int^{A_s} \sigma_s \, dA = E_s A_s \left(\varepsilon_0 + \chi d_s + \frac{ds}{dx}\right) \tag{11}$$

Where $d_s$ is the centroid measured from concrete top fibre to the centroid of profiled deck

$$N_r = \int^{A_r} \sigma_r \, dA = E_r A_r(\varepsilon_0 + \chi d_r) \tag{12}$$

Hence from force equilibrium

$$0 = N_s + N_c + N_r = EA_1(\varepsilon_0 + \chi d_1) + E_s A_s \frac{ds}{dx} - E_c A_c \bar{\varepsilon}_{sh_c} \tag{13}$$

where

$$EA_1 = E_cA_c + E_sA_s + E_rA_r \tag{14}$$

$$d_1 = \frac{E_cA_cd_c + E_sA_sd_s + E_rA_rd_r}{EA_1} \tag{15}$$

From force equilibrium and rearranging Eq. (13) gives the strain at the top fibre as

$$\varepsilon_0 = -\chi d_1 - \frac{E_sA_s}{EA_1}\frac{ds}{dx} + \frac{E_cA_c}{EA_1}\bar{\varepsilon}_{sh_c} \tag{16}$$

Next taking moments at the centroid of each component

$$M_c = \int^{A_c} \sigma_c(y - d_c)\, dA = E_cI_c(\chi - \chi_{sh}) \tag{17}$$

$$M_s = \int^{A_s} \sigma_s(y - d_s)\, dA = E_sI_s\chi \tag{18}$$

The moments for the reinforcement are taken at the centroid of the concrete section

$$M_r = \int^{A_r} \sigma_r(y - d_r)\, dA = [E_rI_r + E_rA_rd_r(d_r - d_c)]\chi + E_rA_r(d_r - d_c)\varepsilon_0 \tag{19}$$

$$M_{shear} = Q\Delta\bar{y} = N_s(d_s - d_c) \tag{20}$$

Where $M_{shear}$ is the moment from shear force $Q$ which is also the accumulated axial force having same magnitude as $N_s$ and $\Delta\bar{y} = d_s - d_c$ centroid difference between concrete and steel deck

Summing these moments gives

$$M = M_s + M_c + M_r + M_{shear} \tag{21}$$

Hence, the moment equilibrium can be simplified to

$$= \chi[E_sI_s + E_cI_c + E_rI_r + E_sA_sd_s(d_s - d_c) + E_rA_rd_r(d_r - d_c)] + \varepsilon_0[E_sA_s(d_s - d_c) + E_rA_r(d_r - d_c)] + E_sA_s(d_s - d_c)\frac{ds}{dx} - E_cI_c\chi_{sh} \tag{22}$$

Now substituting in $\varepsilon_0$

$$M = EI_1\chi - E_cI_c\chi_{sh} + E_sA_sC_1\frac{ds}{dx} + F_1 \tag{23}$$

where

$$EI_1 = E_sI_s + E_cI_c + E_rI_r + E_rA_r(d_r - d_1)(d_r - d_c) + E_sA_s(d_s - d_1)(d_s - d_c) \tag{24}$$

$$B_1 = \frac{1}{EA_1}[E_r A_r(d_r - d_c) + E_s A_s(d_s - d_c)] \tag{25}$$

$$C_1 = (d_s - d_c) - \frac{E_s A_s(d_s - d_c) + E_r A_r(d_r - d_c)}{EA_1} = d_s - d_c - B_1 \tag{26}$$

$$F_1 = \frac{E_c A_c}{EA_1}[E_s A_s(d_s - d_c) + E_r A_r(d_r - d_c)]\bar{\varepsilon}_{sh_c} = E_c A_c B_1 \bar{\varepsilon}_{sh_c} \tag{27}$$

Hence rearranging Eq. (23) gives the curvature as

$$\chi = \frac{M}{EI_1} + \frac{E_c I_c}{EI_1}\chi_{sh} - \frac{E_s A_s C_1}{EI_1}\frac{ds}{dx} - \frac{F_1}{EI_1} \tag{28}$$

As shown in **Fig. 3**, it is clearly showed the strain-stress-reaction profiles used for segmental analysis of composite slab with considering shrinkage effect. It shows the segmental analysis for reinforced concrete in **Fig. 3**(a)-(d) and for profiled deck in **Fig. 3**(e)-(h). Both steel components will follow strain profile in blue and concrete will follow that in black.

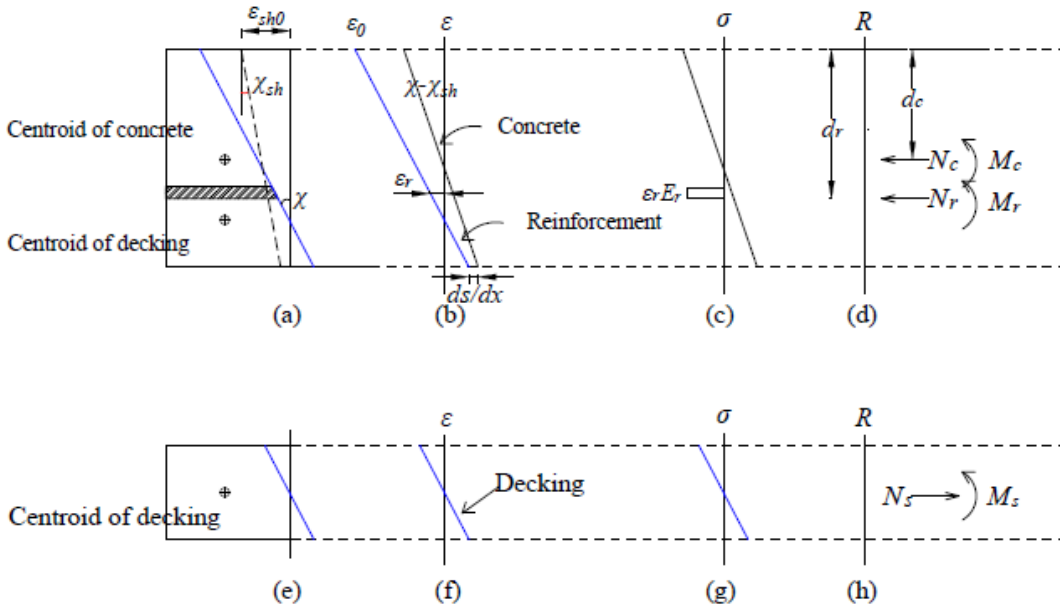


**Fig. 3.** Segmental analysis for composite slab uncracking condition

Note that the curvature is a function of the slip strain, to find this relationship, consider that the change in the force in the steel along the length of the member is a function of the shear flow $q$ between the steel and concrete section, that is

$$\frac{dN_s}{dx} = q \tag{29}$$

Enable to do this differentiation, now substituting Eq. (16) into Eq. (11), the expression of $N_s$ can be updated to

$$N_s = E_s A_s \left[\chi(d_s - d_1) + \left(1 - \frac{E_s A_s}{E A_1}\right)\frac{ds}{dx} + \frac{E_c A_c}{E A_1}\bar{\varepsilon}_{sh_c}\right] \tag{30}$$

Hence differentiating Eq. (30) gives

$$q = E_s A_s (d_s - d_1)\frac{d\chi}{dx} + E_s A_s \left(1 - \frac{E_s A_s}{E A_1}\right)\frac{d^2 s}{dx^2} \tag{31}$$

Differentiating Eq. (28) gives

$$\frac{d\chi}{dx} = \frac{V}{E I_1} - \frac{E_s A_s C_1}{E I_1}\frac{d^2 s}{dx^2} \tag{32}$$

Where $V$ is the shear force, substituting Eq. (32) into Eq. (31) gives

$$q = \frac{E_s A_s (d_s - d_1)}{E I_1} V + E_s A_s G_1 \frac{d^2 s}{dx^2} \tag{33}$$

where

$$G_1 = -\frac{E_s A_s (d_s - d_1) C_1}{E I_1} + 1 - \frac{E_s A_s}{E A_1} \tag{34}$$

Rearranging gives the following second order differential equation

$$\frac{d^2 s}{dx^2} = \frac{q}{E_s A_s G_1} - \frac{(d_s - d_1)}{E I_1 \, G_1} V \tag{35}$$

To solve Eq. (35) consider the shear flow is given as a function of the slip as

$$q = K_{pr} s \tag{36}$$

where $K_{pr}$ is the stiffness of the shear flow relationship, $s$ is the slip

Hence Eq. (35) becomes

$$\frac{d^2 s}{dx^2} = \frac{K_{pr}}{E_s A_s G_1} s - \frac{(d_s - d_1)}{E I_1 \, G_1} V \tag{37}$$

From the method for non-homogenous linear second order differential equations, the process can be found in textbook, it has solutions of the form

$$s = c_1 \sinh(\lambda_1 x) + c_2 \cosh(\lambda_1 x) + \frac{V}{K_{pr}} \frac{E_s A_s (d_s - d_1)}{E I_1} \tag{38}$$

where

$$\lambda_1 = \sqrt{\frac{K_{pr}}{E_s A_s G_1}} \tag{39}$$

Where *x* is the horizontal distance along the member from the left-hand support.

The slip strain corresponding to Eq. (38) is

$$\frac{ds}{dx} = \lambda_1 c_1 \cosh(\lambda_1 x) + \lambda_1 c_2 \sinh(\lambda_1 x) \tag{40}$$

#### *5.4.1.1 Application of boundary conditions*

The expression of parameters used for individual segmental analysis have been derived, the next step is to now combine these equations with the boundary conditions in slab analysis to determine a final expression of curvature which can resolve the uncertainty of slip strain as shown in Eq. (28). There are two boundary conditions can be applied to simplify analysis and enable it to evaluate curvature directly. As shown in **Fig. 4**, the boundary conditions are as follows: (i) the accumulated axial force in steel deck is zero at the support and (ii) slip should be zero at the mid span [13].

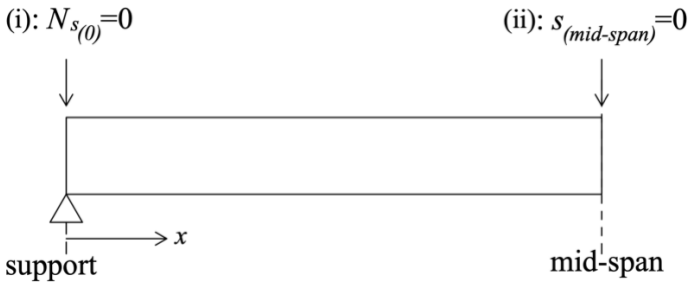


**Fig. 4.** Boundary conditions for slab uncracking analysis

Firstly, zero accumulated axial force occurred at the support ($x = 0$) is applied into the analysis. Then, the moment is zero, hence Eq. (28) can be simplified into

$$\chi = \frac{E_c I_c}{EI_1}\chi_{sh} - \frac{E_s A_s C_1}{EI_1}\frac{ds}{dx} - \frac{F_1}{EI_1} \tag{41}$$

Substituting Eq. (41) into Eq. (30) gives

$$N_s = E_s A_s \left\{\left[\frac{E_c I_c}{EI_1}\chi_{sh} - \frac{E_s A_s C_1}{EI_1}\frac{ds}{dx} - \frac{F_1}{EI_1}\right](d_s - d_1) + \left(1 - \frac{E_s A_s}{EA_1}\right)\frac{ds}{dx} + \frac{E_c A_c}{EA_1}\bar{\varepsilon}_{sh_c}\right\} \tag{42}$$

Now at the support, the axial force is zero ($N_s$=0), hence Eq. (42) can be updated as

$$0 = \left[-\frac{E_s A_s C_1 (d_s - d_1)}{EI_1} + 1 - \frac{E_s A_s}{EA_1}\right]\frac{ds}{dx} + \frac{E_c I_c (d_s - d_1)}{EI_1}\chi_{sh} + \frac{E_c A_c}{EA_1}\bar{\varepsilon}_{sh_c} - \frac{F_1 (d_s - d_1)}{EI_1} \tag{43}$$

Rearranging it and the slip strain ($\frac{ds}{dx}$) at the support can be expressed as

$$\left(\frac{ds}{dx}\right)_0 = -\frac{E_c I_c (d_s - d_1)}{EI_1\, G_1}\chi_{sh} - \frac{E_c A_c}{EA_1 G_1}\bar{\varepsilon}_{sh_c} + \frac{F_1 (d_s - d_1)}{EI_1 G_1} \tag{44}$$

It can be observed that the value of slip strain at the support $\left(\frac{ds}{dx}\right)_0$ is only dependent on the composite slab material properties that means Eq. (44) is applicable for both central point load and UDL configurations. Due to in these two different loading configurations, the expressions of slip and slip strain are not same but the value of slip strain at the support is same, hence $\left(\frac{ds}{dx}\right)_0$ can be used to express the coefficients $(c_1, c_2)$ in slip and slip strain expressions. As shown in Eq. (28), the current curvature expression is expressed by material properties and slip strain while the expression of slip will be varied for central point loading and UDL. Hence, the following procedures will determine the final expression of curvature for central point load and UDL separately where these final expressions for curvature can be only related to material properties.

#### 5.4.1.1.1 Central Point load

The shear force (*V*) is a function of the assumed loading. For a central point load, the shear force is

$$V = \frac{pl}{2} \tag{45}$$

Where *pl* is the total central applied load

Bring $x = 0$ into Eq. (40), now the slip strain at the support is

$$\frac{ds}{dx} = \lambda_1 c_1 = \left(\frac{ds}{dx}\right)_0 \tag{46}$$

Hence

$$c_1 = \frac{\left(\frac{ds}{dx}\right)_0}{\lambda_1} \tag{47}$$

Another boundary condition is that slip is zero at the mid-span, hence bring $x = \frac{L}{2}$ into Eq. (38), it becomes

$$0 = c_1 \sinh\left(\frac{\lambda_1 L}{2}\right) + c_2 \cosh\left(\frac{\lambda_1 L}{2}\right) + \frac{V}{K_{pr}} \frac{E_s A_s (d_s - d_1)}{EI_1} \tag{48}$$

Rearranging it get

$$c_2 = -\frac{\left(\frac{ds}{dx}\right)_0}{\lambda_1}\tanh\left(\frac{\lambda_1 L}{2}\right) - \frac{V}{K_{pr}}\frac{E_S A_S (d_S - d_1)}{EI_1\cosh\left(\frac{\lambda_1 L}{2}\right)} \quad (49)$$

Since the coefficients used in expression of slip strain has been determined, bring Eq. (47) and Eq. (49) into Eq. (40), the slip strain at a distance *x* from the support in central point loading is now given by

$$\frac{ds}{dx} = \left(\frac{ds}{dx}\right)_0 \frac{\cosh\left[\lambda_1\left(x-\frac{L}{2}\right)\right]}{\cosh\left(\frac{\lambda_1 L}{2}\right)} - \lambda_1 \frac{V}{K_{pr}}\frac{E_S A_S (d_S - d_1)}{EI_1}\frac{\sinh(\lambda_1 x)}{\cosh\left(\frac{\lambda_1 L}{2}\right)} \quad (50)$$

Where we have used the identity

$$\cosh(\lambda_1 x) - \tanh\left(\frac{\lambda_1 L}{2}\right)\sinh(\lambda_1 x) = \frac{\cosh\left[\lambda_1\left(x-\frac{L}{2}\right)\right]}{\cosh\left(\frac{\lambda_1 L}{2}\right)} \quad (51)$$

Therefore the curvature at a distance *x* from the support in central point loading is given by

$$\chi = \frac{M}{EI_1} + \frac{E_c I_c}{EI_1}\chi_{sh} - \frac{E_S A_S C_1}{EI_1}\left(\frac{ds}{dx}\right)_0 \frac{\cosh\left[\lambda_1\left(x-\frac{L}{2}\right)\right]}{\cosh\left(\frac{\lambda_1 L}{2}\right)} + \frac{V\lambda_1}{K_{pr}}\frac{(E_S A_S)^2 C_1 (d_S - d_1)}{(EI_1)^2}\frac{\sinh(\lambda_1 x)}{\cosh\left(\frac{\lambda_1 L}{2}\right)} - \frac{F_1}{EI_1} \quad (52)$$

#### 5.4.1.1.2 UDL

For a simply supported beam with a UDL the boundary conditions are the same and the shear force changes to

$$V = w\left(\frac{L}{2} - x\right) \quad (53)$$

Eq. (37) can be updated into

$$\frac{d^2 s}{dx^2} = \frac{K_{pr}}{E_S A_S G_1}s - \frac{(d_S - d_1)}{EI_1\, G_1}w\left(\frac{L}{2} - x\right) \quad (54)$$

The solution of slip in this UDL case is

$$s = c_1\sinh(\lambda_1 x) + c_2\cosh(\lambda_1 x) + \frac{w}{K_{pr}}\frac{E_S A_S (d_S - d_1)}{EI_1}\left(\frac{L}{2} - x\right) \quad (55)$$

Differentiating the distribution of slip gives the distribution of slip strain

$$\frac{ds}{dx} = \lambda_1[c_1\cosh(\lambda_1 x) + c_2\sinh(\lambda_1 x)] - \frac{w}{K_{pr}}\frac{E_S A_S (d_S - d_1)}{EI_1} \quad (56)$$

And at the support, bring $x = 0$ into the slip strain is

$$\left(\frac{ds}{dx}\right)_0 = \lambda_1 c_1 - \frac{w}{K_{pr}} \frac{E_s A_s (d_s - d_1)}{EI_1} \tag{57}$$

Hence using the pre-know slip strain at the support $\left(\frac{ds}{dx}\right)_0$ to express the coefficient used in expression of slip strain, it gets

$$c_1 = \frac{\left(\frac{ds}{dx}\right)_0}{\lambda_1} + \frac{w}{K_{pr}} \frac{E_s A_s (d_s - d_1)}{EI_1 \lambda_1} \tag{58}$$

And the slip at the mid-span is zero, bring $x = \frac{L}{2}$ into Eq. (55), rearranging it get

$$c_2 = -c_1 \frac{\sinh\left(\lambda_1 \frac{L}{2}\right)}{\cosh\left(\lambda_1 \frac{L}{2}\right)} \tag{59}$$

Hence the slip strain at a distance *x* from the support in UDL is now given by

$$\frac{ds}{dx} = \left(\frac{ds}{dx}\right)_0 \frac{\cosh\left[\lambda_1\left(x - \frac{L}{2}\right)\right]}{\cosh\left(\frac{\lambda_1 L}{2}\right)} + \frac{w}{K_{pr}} \frac{E_s A_s (d_s - d_1)}{EI_1} \left[\frac{\cosh\left[\lambda_1\left(x - \frac{L}{2}\right)\right]}{\cosh\left(\frac{\lambda_1 L}{2}\right)} - 1\right] \tag{60}$$

Therefore the curvature at a distance *x* from the support in UDL is given by

$$\chi = \frac{M}{EI_1} + \frac{E_c I_c}{EI_1} \chi_{sh} - \frac{E_s A_s C_1}{EI_1} \left\{\left(\frac{ds}{dx}\right)_0 \frac{\cosh\left[\lambda_1\left(\frac{L}{2} - x\right)\right]}{\cosh\left(\frac{\lambda_1 L}{2}\right)} + \frac{w}{K_{pr}} \frac{E_s A_s (d_s - d_1)}{EI_1} \left[\frac{\cosh\left[\lambda_1\left(\frac{L}{2} - x\right)\right]}{\cosh\left(\frac{\lambda_1 L}{2}\right)} - 1\right]\right\} - \frac{F_1}{EI_1} \tag{61}$$

#### *5.4.1.2 Procedures for determining slab deflection*

The half span of a simply supported composite slab is symmetrically loaded about the mid-span with the length of *L/2* which is divided into very small elements equally of length of $L_e$ as shown in Fig. 5.

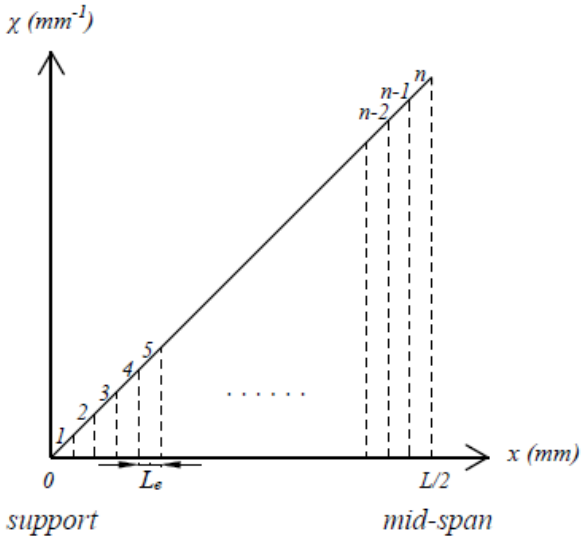


**Fig. 5.** Curvature variation along distance (Uncracking analysis)

Therefore, for the slab uncracking analysis, it will follow the procedures demonstrated in **Fig. 6** to determine the curvature value for each segment and then determine slab mid-span deflection.

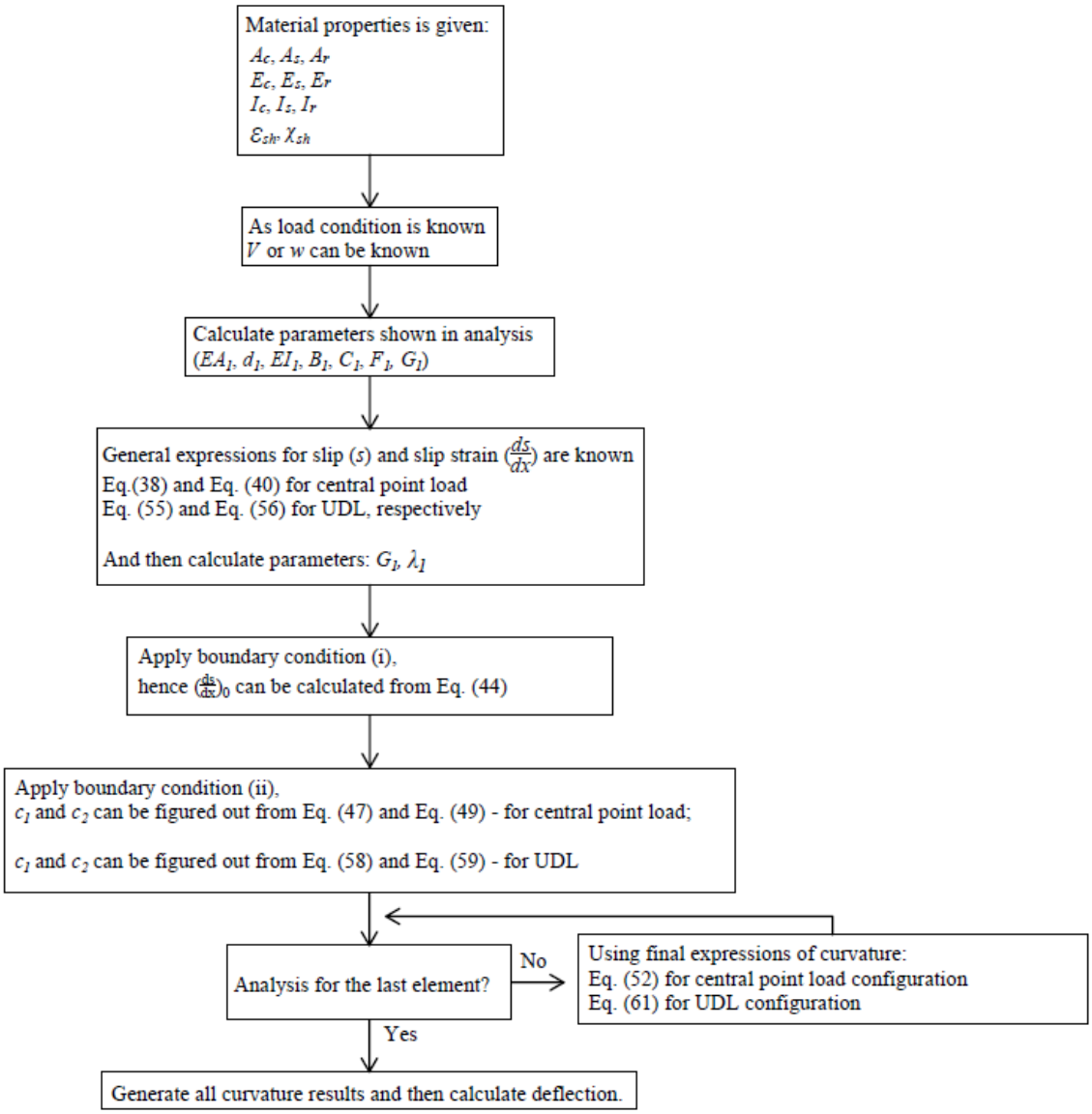


**Fig. 6.** Procedure for generating curvature in slab uncracking analysis

### *5.4.2 Micro-cracking stage*

With the loading increasing, for part of the slab, concrete will experience 'micro-cracking'. In the following section, the general expressions for segmental analysis in micro-cracking conditions will be figured out and then the process for combining both uncracking and micro-cracking analysis into one slab analysis will be explained.

Due to concrete micro-cracking, the axial force in concrete component is updated to

$$N_c = N_{c1} + N_{c2} \tag{62}$$

Where $N_{c1}$ is for uncracked component and $N_{c2}$ is for micro-cracked component as shown in **Fig. 7**(d)

$$N_{c1} = \int^{A_{c1}} \sigma_c \, dA = E_c \int^{A_{c1}} (\varepsilon_c - \varepsilon_{sh}) \, dA = E_c A_{c1} (\varepsilon_0 + \chi d_{c1} - \bar{\varepsilon}_{sh1}) \tag{63}$$

Where

$$A_{c1} = bD_{c1} \tag{64}$$

$A_{c1}$ is the area of uncracked concrete component and $d_{c1}$ is the depth to the centroid of the uncracked concrete, $\bar{\varepsilon}_{sh1} = \varepsilon_{sh0} + \chi_{sh} d_{c1}$ is the average shrinkage strain for the concrete uncracked concrete and the total depth of the uncracked concrete is

$$D_{c1} = d_{NA} + d_t = \frac{\varepsilon_{SH} - \varepsilon_0 + \varepsilon_{sh0}}{\chi - \chi_{sh}} \tag{65}$$

in which

$$d_{NA} = \frac{-\varepsilon_0 + \varepsilon_{sh0}}{\chi - \chi_{sh}} \tag{66}$$

And

$$d_t = \frac{\varepsilon_{SH}}{\chi - \chi_{sh}} \tag{67}$$

And then the axial force in concrete micro-cracked component is

$$N_{c2} = \int^{A_{c2}} \sigma_c \, dA = f_1 A_{c2} + E_{SH} \int^{A_{c2}} (\varepsilon_c - \varepsilon_{sh}) \, dA$$

$$= f_1 A_{c2} + E_{SH} A_{c2} (\varepsilon_0 + \chi d_{c2} - \bar{\varepsilon}_{sh2}) \tag{68}$$

Where

$$A_{c2} = b(D - D_{c1}) \tag{69}$$

$A_{c2}$ is the area of concrete micro-cracked component and $d_{c2}$ is the depth to the centroid of the concrete micro-cracked component and $\bar{\varepsilon}_{sh2} = \varepsilon_{sh0} + \chi_{sh} d_{c2}$ is the average shrinkage strain for the micro-cracked component.

Hence, bring Eq. (63) and Eq. (68) into Eq. (62), the expression of $N_c$ can be updated as

$$N_c = \varepsilon_0(E_cA_{c1} + E_{SH}A_{c2}) + \chi(E_cA_{c1}d_{c1} + E_{SH}A_{c2}d_{c2}) - E_cA_{c1}\bar{\varepsilon}_{sh1} - E_{SH}A_{c2}\bar{\varepsilon}_{sh2} + f_1A_{c2} \quad (70)$$

$N_s$ and $N_r$ follow the same expression in uncracking analysis as Eq. (11) and Eq. (12), hence from force equilibrium, we can get

$$0 = N_s + N_c + N_r = EA_2(\varepsilon_0 + \chi d_2) - \overline{\overline{EA\varepsilon_{sh}}} + E_sA_s\frac{ds}{dx} + f_1A_{c2} \quad (71)$$

Rearranging it, we can get

$$\varepsilon_0 = -\chi d_2 - \frac{E_sA_s}{EA_2}\frac{ds}{dx} + \frac{\overline{\overline{EA\varepsilon_{sh}}}}{EA_2} - \frac{f_1A_{c2}}{EA_2} \quad (72)$$

Where

$$EA_2 = E_cA_{c1} + E_{SH}A_{c2} + E_sA_s + E_rA_r \quad (73)$$

$$d_2 = \frac{E_cA_{c1}d_{c_1} + E_{SH}A_{c2}d_{c2} + E_sA_sd_s + E_rA_rd_r}{EA_2} \quad (74)$$

$$\overline{\overline{EA\varepsilon_{sh}}} = E_cA_{c1}\bar{\varepsilon}_{sh1} + E_{SH}A_{c2}\bar{\varepsilon}_{sh2} \quad (75)$$

In segmental analysis microcracking condition, the moment in concrete comprised of two components where the moment in concrete uncracked component is

$$M_{c1} = (\chi - \chi_{sh})E_cI_{cr} \quad (76)$$

Where

$$I_{cr} = b\left[\frac{D_{c1}^3}{12} + (d_t - d_{NA})D_{c1}\left(\frac{D_{c1}}{4} - \frac{d_c}{2}\right)\right] \quad (77)$$

And the moment in concrete micro-cracked component is

$$M_{c_2} = E_{SH}\overline{Ay}\varepsilon_0 + DE_{SH}\overline{Ay}\chi - E_{SH}\overline{Ay}\bar{\varepsilon}_{sh_{boc}} + \overline{Ay}f_1 + b(D - D_{c1})\left(\frac{D}{6} - \frac{d_c}{2} + \frac{D_{c1}}{3}\right)f_{SH} \quad (78)$$

Where

$$\overline{Ay} = b(D - D_{c1})\left(\frac{D}{3} - \frac{d_c}{2} + \frac{D_{c1}}{6}\right) \quad (79)$$

The moment of steel deck, reinforcement and shear force still followed the same equation as Eq. (18-20).

Therefore, summing these moments and bring the expression of $N_s$ (Eq. (11)) and $\varepsilon_0$ (Eq. (72)) to simplify the equation, when concrete cracked, moment equilibrium is

$$M = EI_2\chi - E_cI_{cr}\chi_{sh} + E_sA_sC_2\frac{ds}{dx} + F_2 \quad (80)$$

Where

$$EI_2 = E_sI_s + E_cI_{cr} + E_{SH}\overline{Ay}(D - d_2) + E_rI_r + E_rA_r(d_r - d_c)(d_r - d_2) + E_sA_s\Delta\bar{y}(d_s - d_2) \quad (81)$$

$$B_2 = \frac{1}{EA_2}\left[E_{SH}\overline{Ay} + E_rA_r(d_r - d_c) + E_sA_s\Delta\bar{y}\right] \quad (82)$$

$$C_2 = \Delta\bar{y} - B_2 \quad (83)$$

$$F_2 = B_2\left(\overline{\overline{EA\varepsilon_{sh}}} - f_1A_{c2}\right) - E_{SH}\overline{Ay}\bar{\varepsilon}_{sh_{boc}} + \overline{Ay}f_1 + b(D - D_{c1})\left(\frac{D}{6} - \frac{d_c}{2} + \frac{D_{c1}}{3}\right)f_{SH} \quad (84)$$

Hence rearranging Eq. (80) gives the curvature as

$$\chi = \frac{M}{EI_2} + \frac{E_cI_{cr}}{EI_2}\chi_{sh} - \frac{E_sA_sC_2}{EI_2}\frac{ds}{dx} - \frac{F_2}{EI_2} \quad (85)$$

As shown in **Fig. 7**, it depicted the strain-stress-reaction profiles for reinforced concrete micro-cracking condition with shrinkage effect, and that for profiled deck are same as in **Fig. 3**(e)-(h). In the figure, it outlined the concrete uncracked component and micro-cracked component which evaluate force components and moment components separately that is different from uncracking analysis.

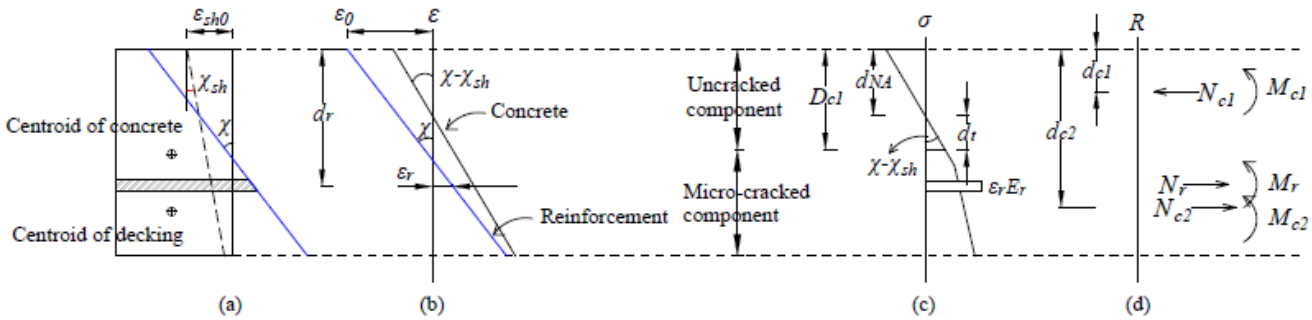


**Fig. 7.** Segmental analysis for composite slab micro-cracking condition

The similar processes as Eq. (29-40) will be repeated to determine coefficient in the common expressions of slip strain and slip.

Now, substituting Eq. (72) into Eq. (11)

$$N_s = E_s A_s \left[\chi(d_s - d_2) + \left(1 - \frac{E_s A_s}{E A_2}\right)\frac{ds}{dx} + \frac{\overline{\overline{EA\varepsilon_{sh}}} - f_1 A_{c2}}{E A_2}\right] \tag{86}$$

Hence differentiating gives

$$q = E_s A_s (d_s - d_2)\frac{d\chi}{dx} + E_s A_s \left(1 - \frac{E_s A_s}{E A_2}\right)\frac{d^2 s}{dx^2} \tag{87}$$

Differentiating Eq. (85) gives

$$\frac{d\chi}{dx} = \frac{V}{E I_2} - \frac{E_s A_s C_2}{E I_2}\frac{d^2 s}{dx^2} \tag{88}$$

Substituting Eq. (88) into Eq. (87) gives

$$q = \frac{E_s A_s (d_s - d_2)}{E I_2} V + E_s A_s G_2 \frac{d^2 s}{dx^2} \tag{89}$$

Where

$$G_2 = -\frac{E_s A_s (d_s - d_2) C_2}{E I_2} + 1 - \frac{E_s A_s}{E A_2} \tag{90}$$

Rearranging gives the following second order differential equation

$$\frac{d^2 s}{dx^2} = \frac{q}{E_s A_s G_2} - \frac{(d_s - d_2)}{E I_2\, G_2} V \tag{91}$$

Due to the bond stiffness between concrete and profiled deck won't change when concrete condition changing from uncracking to micro-cracking, the shear flow $q$ function expressed by slip is still applicable, hence bring Eq.(36) into Eq. (91),

$$\frac{d^2 s}{dx^2} = \frac{K_{pr}}{E_s A_s\, G_2} s - \frac{(d_s - d_2)}{E I_2\, G_2} V \tag{92}$$

This has solutions of the form

$$s = c_3 \sinh(\lambda_2 x) + c_4 \cosh(\lambda_2 x) + \frac{V}{K_{pr}}\frac{E_s A_s (d_s - d_2)}{E I_2} \tag{93}$$

where

$$\lambda_2 = \sqrt{\frac{K_{pr}}{E_s A_s G_2}} \tag{94}$$

The slip strain corresponding to Eq. (93) is

$$\frac{ds}{dx} = \lambda_2 c_3 \cosh(\lambda_2 x) + \lambda_2 c_4 \sinh(\lambda_2 x) \tag{95}$$

Similarly, for UDL, referred from section 5.4.1.1.2, the expression of slip strain and slip are

$$s = c_3 \sinh(\lambda_2 x) + c_4 \cosh(\lambda_2 x) + \frac{w}{K_{pr}} \frac{E_s A_s (d_s - d_2)}{E I_2} \left(\frac{L}{2} - x\right) \tag{96}$$

Differentiating the distribution of slip gives the distribution of slip strain

$$\frac{ds}{dx} = \lambda_2 [c_3 \cosh(\lambda_2 x) + c_4 \sinh(\lambda_2 x)] - \frac{w}{K_{pr}} \frac{E_s A_s (d_s - d_2)}{E I_2} \tag{97}$$

#### *5.4.2.1 Application of boundary conditions*

As the expressions for slip and slip strain are all known, the following part will show process to determine the slab uncracking part firstly, and then show process to determine the general expressions for coefficient $c_3$ and $c_4$ in slab micro-cracking part analysis.

Herein, due to concrete tensile bi-linear strain-stress relationship, there is no fixed value for $c_3$ and $c_4$. As referred from uncracking analysis, the coefficient $c_1$ and $c_2$ is related to $EI_1$, $d_1$ while in micro-cracking analysis, $EI_2$, $d_2$ will change with guess value for $d_{NA}$ that means the value for $c_3$ and $c_4$ will be varied in each segment experience micro-cracking. In the following, the general expression of $c_3$ and $c_4$ which can be applicable for each individual segments experiencing micro-cracking for both central point load and UDL configurations will be determined respectively. In slab micro-cracking analysis, the pre-mentioned two boundary conditions are still applicable. Besides, there is a transition point where the bottom of concrete strain is just equal to the strain to cause micro-cracking ($\varepsilon_{SH}$) which can be used as an additional boundary condition for slab analysis. Hence, as shown in **Fig. 8**, the part from support to transition point is categorised to uncracking part with length of $X_{(n)}$while the remaining is micro-cracking part with length of $\frac{L}{2} - X_{(n)}$.

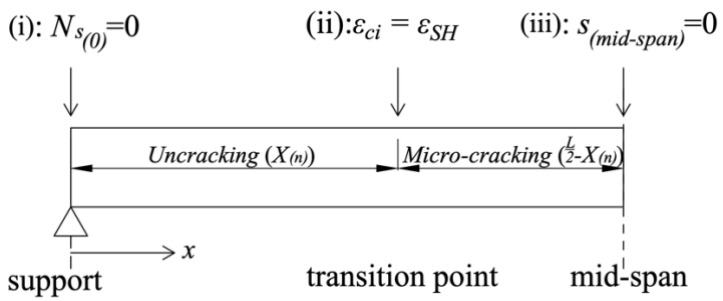

**Fig. 8.** Boundary conditions for slab micro-cracking analysis

For different loading scenarios, the procedures of applying boundary conditions will be evaluated separately.

5.4.2.1.1 Central Point load

**At the support**

At the support point, bring $x = 0$ into the expression for slip, rearranging Eq.(38) c2 can be expressed as

$$c_2 = s_1 - \frac{V}{K_{pr}} \frac{E_s A_s (d_s - d_1)}{E I_1} \tag{98}$$

And the slip strain at the support is still follow the Eq. (46), and then coefficient $c_1$ can be determined from Eq. (47)

**At transition point**

At transition point, concrete bottom strain ($\varepsilon_{ci}$) with shrinkage-induced strain should reach to strain to cause micro-cracking ($\varepsilon_{SH}$), then we can get expression:

$$\varepsilon_{ci_{(x=X_{(n)})}} = \varepsilon_{0_{(x=X_{(n)})}} + \chi_{(x=X_{(n)})} D - (\varepsilon_{sh0} + \chi_{sh} D) = \varepsilon_{SH} \tag{99}$$

Rearranging Eq. (99), and then the curvature at transition point $\chi_{(x=X_{(n)})}$ can be expressed as

$$\chi_{(x=X_{(n)})} = \frac{\varepsilon_{SH} - \varepsilon_{0_{(x=X_{(n)})}} + \varepsilon_{sh0}}{D} + \chi_{sh} \tag{100}$$

(Footnote: $x = X_{(n)}$ indicate the distance measured from support to the segment which just start to experience micro-cracking).

As shown in Eq. (16), expression of $\varepsilon_0$ is expressed by $\chi$, herein, bring Eq. (100) into Eq. (16), then we get

$$\varepsilon_{0_{(x=X_{(n)})}} = -\left[\frac{\varepsilon_{SH} - \varepsilon_{0_{(x=X_{(n)})}} + \varepsilon_{sh0}}{D} + \chi_{sh}\right] d_1 - \frac{E_s A_s}{E A_1} \frac{ds}{dx_{(x=X_{(n)})}} + \frac{E_c A_c}{E A_1} \bar{\varepsilon}_{sh_c} \tag{101}$$

Rearrange Eq. (101), the expression of $\varepsilon_0$ is related to material properties and slip strain.

$$\varepsilon_{0_{(x=X_{(n)})}} = -\frac{\varepsilon_{SH} d_1}{D - d_1} - \frac{d_1}{D - d_1} \varepsilon_{sh0} - \frac{D d_1}{D - d_1} \chi_{sh} - \frac{D}{D - d_1} \frac{E_s A_s}{E A_1} \frac{ds}{dx_{(x=X_{(n)})}} + \frac{D}{D - d_1} \frac{E_c A_c}{E A_1} \bar{\varepsilon}_{sh_c} \tag{102}$$

Enable general expression of curvature to be equal to this specific condition, hence Eq. (100) = Eq. (28), it is

$$\frac{\varepsilon_{SH}-\varepsilon_{0(x=X_{(n)})}+\varepsilon_{sh0}}{D}+\chi_{sh}=\frac{VX_{(n)}}{EI_1}+\frac{E_cI_c}{EI_1}\chi_{sh}-\frac{E_sA_sC_1}{EI_1}\frac{ds}{dx_{(x=X_{(n)})}}-\frac{F_1}{EI_1} \quad (103)$$

Where moment ($M$) is replaced by an expression about shear force ($V$), and $X_{(n)}$ is the distance measured from support to transition point which is also the length of slab uncracking part.

Bring Eq. (102) into Eq. (103), rearrange it and then get expression for $X_{(n)}$

$$X_{(n)}=\frac{EI_1}{V}\left(\frac{1}{D-d_1}\right)\varepsilon_{sh0}+\frac{EI_1}{V}\left(\frac{D}{D-d_1}-\frac{E_cI_c}{EI_1}\right)\chi_{sh}+\frac{EI_1}{V}\left(\frac{1}{D-d_1}\frac{E_sA_s}{EA_1}+\frac{E_sA_sC_1}{EI_1}\right)\frac{ds}{dx_{(x=n)}}-\frac{EI_1}{V}\frac{1}{D-d_1}\frac{E_cA_c}{EA_1}\bar{\varepsilon}_{sh_c}+\frac{F_1}{V}+\frac{EI_1}{V}\frac{\varepsilon_{SH}}{D-d_1} \quad (104)$$

This part illustrates the relationship between $\frac{ds}{dx_{(x=X_{(n)})}}$ and $X_{(n)}$. Firstly, guess a value for $X_{(n)}$, bring it into Eq. (40) and then bring the calculated $\frac{ds}{dx_{(x=X_{(n)})}}$ result into Eq. (104) to check if the numerical $X_{(n)}$ get the same results as the initial guess. And using iteration to finally find a unique result for $X_{(n)}$.

**General expression for $c_3$ and $c_4$**

A general relationship of $c_3$ and $c_4$ for individual segments which experience micro-cracking in segmental analysis, should be given.

To achieve this, bring Eq. (95) expression for slip strain into Eq. (86) expression for $N_s$, rearranging the equation, $c_3$ can be expressed as:

$$c_3=\frac{\left[\frac{N_s}{E_sA_s}-\chi(d_s-d_2)-\frac{\overline{\overline{EA\varepsilon_{sh}}}-f_1A_{c2}}{EA_2}\right]}{\lambda_2\cosh(\lambda_2x)(1-\frac{E_sA_s}{EA_2})}-c_4\tanh(\lambda_2x) \quad (105)$$

From Eq. (93), general expression for slip '$s$', then $c_4$ can be expressed as:

$$c_4=\frac{s-c_3\sinh(\lambda_2x)-\frac{V}{K_{pr}}\frac{E_sA_s(d_s-d_2)}{EI_2}}{\cosh(\lambda_2x)} \quad (106)$$

Bring Eq. (106) into Eq. (105), the simplified expression for $c_3$ is

$$c_3 = \frac{\left[\frac{N_S}{E_S A_S} - \chi(d_s - d_2) - \frac{\overline{\overline{EA\varepsilon_{sh}}} - f_1 A_{c2}}{EA_2}\right]}{\lambda_2\left(1 - \frac{E_S A_S}{EA_2}\right)} \cosh(\lambda_2 x) - \sinh(\lambda_2 x) s + \sinh(\lambda_2 x) \frac{V}{K_{pr}} \frac{E_S A_S (d_s - d_2)}{EI_2} \quad (107)$$

Where the following the identity is used

$$1 - tanh^2(\lambda_2 x) = \text{sech}^2(\lambda_2 x) = \frac{1}{\cosh(\lambda_2 x)^2} \quad (108)$$

5.4.2.1.2 UDL

**At the support**

At the support point, bring $x = 0$ into expression for slip, Eq. (55) can be updated to

$$c_2 = s_1 - \frac{w}{K_{pr}} \frac{E_S A_S (d_s - d_1)}{EI_1} \frac{L}{2} \quad (109)$$

And the slip strain at the support is still follow Eq. (57), and $c_1$ can be determined from Eq. (58).

**At the transition point**

At transition point, concrete bottom strain with shrinkage-induced strain should reach to strain to cause micro-cracking ($\varepsilon_{SH}$), and Eq. (99)-(102) are still applicable for UDL analysis.

As shown in Eq. (102), in UDL analysis, the shear force is not constant along the half span, in curvature expressions, bring Eq. (53) into Eq. (103) and get

$$\frac{\varepsilon_{SH} - \varepsilon_{0\left(x = X_{(n)}\right)} + \varepsilon_{sh0}}{D} + \chi_{sh} = \frac{w\left(\frac{L}{2} - X_{(n)}\right) X_{(n)}}{EI_1} + \frac{E_c I_c}{EI_1} \chi_{sh} - \frac{E_S A_S C_1}{EI_1} \frac{ds}{dx_{(x = X_{(n)})}} - \frac{F_1}{EI_1} \quad (110)$$

Bring Eq. (102) into Eq. (110), rearrange it and finally get expression for $X_{(n)}$

$$\left(\frac{L}{2} - X_{(n)}\right) X_{(n)} = \frac{EI_1}{w}\left(\frac{1}{D - d_1}\right) \varepsilon_{sh0} + \frac{EI_1}{w}\left(\frac{D}{D - d_1} - \frac{E_c I_c}{EI_1}\right) \chi_{sh} + \frac{EI_1}{w}\left(\frac{1}{D - d_1} \frac{E_S A_S}{EA_1} + \frac{E_S A_S C_1}{EI_1}\right) \frac{ds}{dx_{\left(x = X_{(n)}\right)}} - \frac{EI_1}{w} \frac{1}{D - d_1} \frac{E_c A_c}{EA_1} \bar{\varepsilon}_{sh_c} + \frac{F_1}{w} + \frac{EI_1}{w} \frac{\varepsilon_{SH}}{D - d_1} \quad (111)$$

Herein, using guessed $X_{(n)}$ in Eq. (56) and then bring the calculated $\frac{ds}{dx_{\left(x = X_{(n)}\right)}}$ into Eq. (111).

Same process conducted as central point loading analysis, using iteration to find the unique value for $X_{(n)}$.

**General expression for $c_3$ and $c_4$**

Similar process as shown in Eq. (105-108), bring Eq. (97) expression for slip strain into Eq. (86) expression for $N_s$, $c_3$ can be shown as:

$$c_3 = \frac{\left[\frac{N_S}{E_S A_S} - \chi(d_s - d_2) - \frac{\overline{\overline{EA\varepsilon_{sh}}} - f_1 A_{c2}}{EA_2}\right]}{\lambda_2 \cosh(\lambda_2 x)(1 - \frac{E_S A_S}{EA_2})} - c_4 \tanh(\lambda_2 x) + \frac{w}{K_{pr}} \frac{E_S A_S (d_s - d_2)}{EI_2 \lambda_2 \cosh(\lambda_2 x)} \quad (112)$$

From Eq. (96), general expression for slip '$s$', $c_4$ can be shown as:

$$c_4 = \frac{\left[s - c_3 \sinh(\lambda_2 x) - \frac{w}{K_{pr}} \frac{E_S A_S (d_S - d_2)}{EI_2} \left(\frac{L}{2} - x\right)\right]}{\cosh(\lambda_2 x)} \quad (113)$$

Bring Eq. (113) into Eq. (112), the simplified expression for $c_3$ is

$$c_3 = \frac{\left[\frac{N_S}{E_S A_S} - \chi(d_s - d_2) - \frac{\overline{\overline{EA\varepsilon_{sh}}} - f_1 A_{c2}}{EA_2}\right]}{\lambda_2 (1 - \frac{E_S A_S}{EA_2})} \cosh(\lambda_2 x) - \sinh(\lambda_2 x)\, s + \frac{w}{K_{pr}} \frac{E_S A_S (d_s - d_2)}{EI_2} \left[\left(\frac{L}{2} - x\right) \sinh(\lambda_2 x) + \frac{\cosh(\lambda_2 x)}{\lambda_2}\right] \quad (114)$$

### *5.4.2.2 Procedures for determining slab deflection*

With load increasing, it is a combination for segments experience uncracking and micro-cracking occurred in one slab analysis. For slab uncracking part, the same procedures as described in section 5.4.1.2 are applied. For the micro-cracking part, due to the micro-cracking analysis requiring iteration to determine the neutral axis and curvature, to efficiently calculate the results, the micro-cracking part was divided into 10 elements and the length of each segment will be

$$L'_e = \frac{\frac{L}{2} - X_{(n)}}{10} \quad (115)$$

As shown in **Fig. 9**, it plots the curvature variation along the half-span and it also outlined the slab uncracking part and micro-cracking part as well as its corresponding individual segment length.

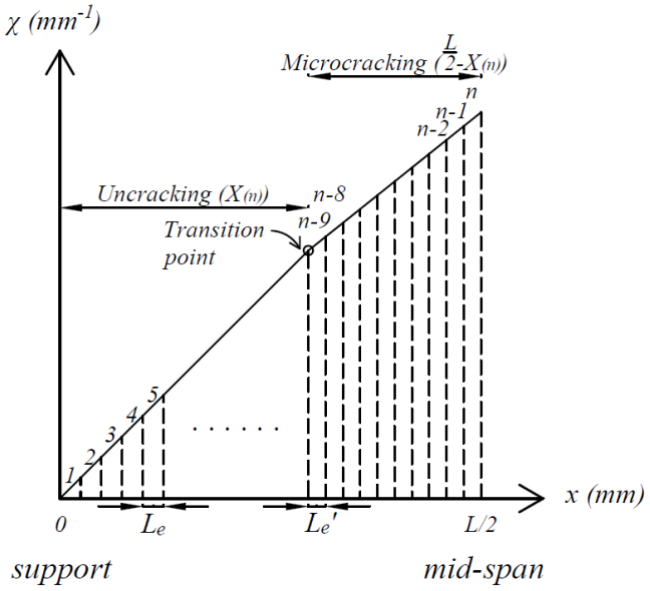


**Fig. 9.** Curvature variation along distance (micro-cracking analysis)

Therefore, as shown in **Fig. 10**, the procedures for generating curvature in slab micro-cracking part are illustrated.

In the micro-cracking analysis, due to the initial guess for $s_1$ is varied than means the value of *Ns*, *s* and *ds/dx* also varied at the transition point. Hence, the slab segmental analysis in micro-cracking requires the manually calculate axial force in each segment which follows

$$N_{s\left(x=X_n+L'_e i\right)} = N_{s\left(x=X_n+L'_e(i-1)\right)} + K_{pr} s_{\left(x=X_n+L'_e(i-1)\right)} \tag{116}$$

Where *i* indicates the number of segment in slab micro-cracking part.

For slab micro-cracking load-deflection analysis, it requires iteration for $s_1$, $d_{NA}$ and curvature, this analysis was implemented in a spreadsheet.

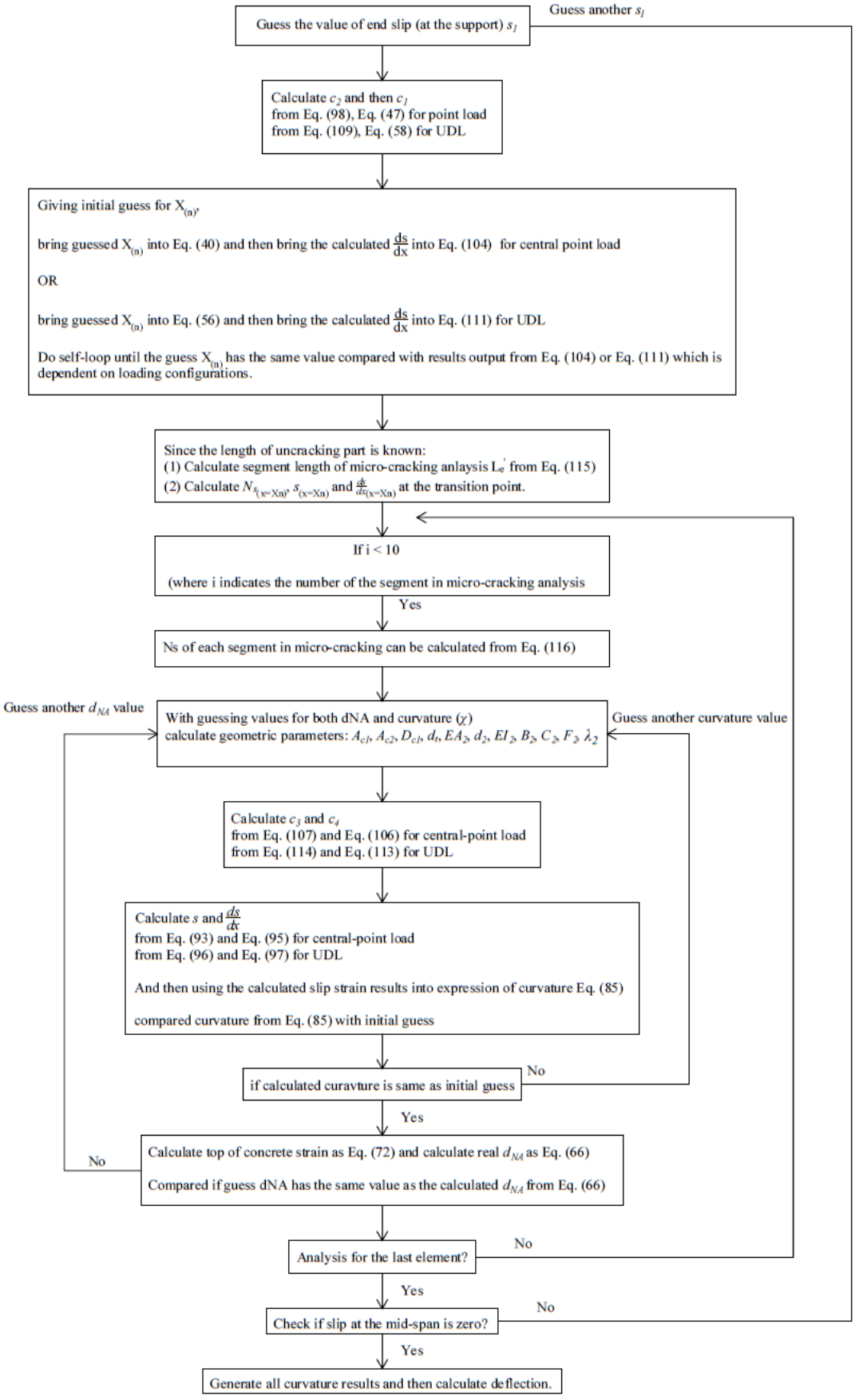


**Fig. 10.** Procedures for generating curvature in slab micro-cracking analysis

**Limit of Micro-Cracking analysis:**

Even though the relationship between moment and curvature has been determined for concrete with micro-cracks, the curvature cannot be calculated in as straightforward a way as for the uncracked analysis. This analytical solution for concrete micro-cracking still has a pre-requisite that a guessed neutral axis value and curvature should be given firstly, in order to find the final pair of curvature and $d_{NA}$ results for each segments experience micro-cracking. Therefore, this procedure for analytical analysis for concrete micro-cracking stage is same as numerical analysis as shown in Chapter 4 which is not an efficient approach. Hence, a further investigation should be given to avoid this iteration and can simplify the process to get curvature value directly.

## 5.5 Validation:

The curvature expression for each segment under central-pointed load or UDL have been determined. Herein, these analytical solutions will be validated by comparing with results from numerical model with using the same inputs.

In this comparison, the span length is 3 m, the cross-section area of concrete block is rectangular with 618 mm width and 100 mm depth. And concrete is reinforced with 2 steel bars with diameter of 10mm at the cover of 20 mm with applying a uniform shrinkage strain. Concrete material properties are shown in **Table 1**.

**Table 1.** Concrete material properties

| | |
|---|---|
| $\varepsilon_{SH}$ | 8.1e-5 |
| $f_{SH}$ (MPa) | 2.5 |
| $\varepsilon_{ct}$ | 2e-4 |
| $f_{ct}$ (MPa) | 4 |
| $E_c$ (MPa) | 30826 |
| $\varepsilon_{sh0}$ | 100 |
| $\chi_{sh}$ | 0 |

For profiled deck, the depth of steel deck is 55 mm and the second moment of inertia is 187172 $mm^4$. In this approach, analytical solutions are related to depth and moment of inertia of steel deck which is not limited to the shape and the type of the steel deck. The young's modulus of profiled deck and reinforcement can be found in **Table 2**, and for steel components, strain-stress relationship are all linear-elastic. In this analysis, there is full-interaction between concrete and reinforced bar and partial-interaction between concrete and profiled deck and the bond stiffness is 125 $N/mm^2$.

**Table 2.** Steel components material properties

| | $E_r$ (MPa) | Bond stiffness (K) ($N/mm^2$) |
|---|---|---|
| Profiled deck | 207000 | 125 |
| Steel bar | 200000 | - (Full Interaction) |

In numeircal study, the segment length will keep as 1 mm whlie in analytical study, $L_e$ is keep for 1 mm and $L_e{}'$ were calculated as **Eq. (115)**.

As shown in **Fig. 11**, the load - midspan deflection results deriving from numerical model and analytical solutions were compared. To check the validation of analytical solutions, the load-deflection results for central-point load and UDL were shown in **Fig. 11**(a) and (b) respectively. To account for long-term effect, **Fig. 11** also shows the results without shrinkage strain and with 100 $\mu\varepsilon$ shrinkage strain effect. The green dots indicate that slabs start to experience micro-cracking condition.

Due to the analytical solutions following the same theory as numerical analysis, the load-deflection results are identical for uncracking stage. In micro-cracking stage, the length of individual segment in numerical simulation is 1mm while in analytical solutions $L_e'$ is related to length of uncracking region which is greater than 1 mm which leads to deflection results in analytical solution that is a little smaller than that from simulation that is ignorable difference and efficiency can be improved with increasing number of analysed segments. Hence, this analytical approach is reliable to be used for composite slab design.

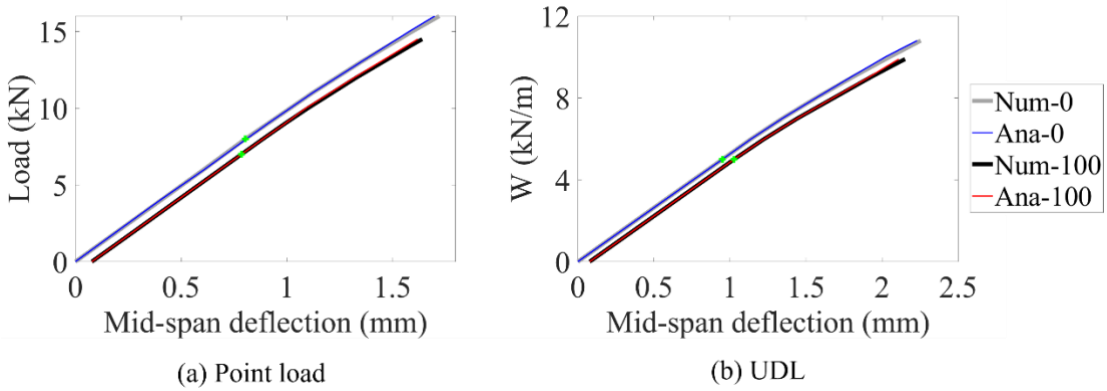


**Fig. 11.** Comparison of analytical solution and numerical solutions of load - deflection comparison

### 5.6 Conclusion

In this chapter, the long-term behaviour of a composite slab under central point load and uniform distributed load (UDL) was studied with allowing for non-uniform shrinkage strain. A new analytical approach studied the mechanics of composite slab which is developed from previous numerical model. This approach has no empirical parameters beyond the material properties and it is applicable for any types of profiled deck as that of basic geometric properties are given. It is also validated against numerical model with utilising same material properties that analytical solutions matched well with results from numerical model. Therefore, this analytical procedure is reliable as a guideline for composite slab in-service design. Furthermore, for micro-cracking analysis, further study is required to address the limitations of iteration involved in analysis.

### 5.7 Notation

$A_c, A_r, A_s$: cross-section area of the concrete, the internal reinforcement and steel sheeting, respectively

$A_{c1}$: area of concrete uncracked component

$A_{c2}$: area for concrete micro-cracked component

$B_1, B_2$: parameter used in moment-curvature expression (1 for uncracking and 2 for micro-cracking)

$b$: width of concrete block

$C_1; C_2$: coefficients used in slip strain component in moment-curvature expression (1 for uncracking analysis and 2 for micro-cracking analysis)

$c_1, c_2;\ c_3, c_4$: coefficient in slip distribution expression (1, 2 for uncracking analysis and 3, 4 for micro-cracking analysis)

$D$: depth of concrete block

$D_{c1}$: total depth of concrete uncrack component

$d_c$: the centroid of concrete component

$d_{c1}$: depth to the centroid of concrete uncracked component

$d_{c2}$: depth to centroid of concrete micro-cracked component

$d_{NA}$: neutral axis of composite slab with considering shrinkage strain

$d_r$: the distance from concrete top fibre to reinforcement

$d_s$: the distance from concrete top fibre to the centroid of profiled deck

$d_t$: depth of concrete in tension uncracked component

$d_1$: centroid of composite slab for uncracking

$d_2$: centroid of composite slab for micro-cracking

$EA_1;\ EA_2$: axial young's modulus of composite slab (1 for uncracking and 2 for micro-cracking)

$\overline{\overline{EA\varepsilon_{sh}}}$: average axial young's modulus for micro-cracking with considering shrinkage strain

$E_c$: elastic modulus of concrete

$E_r$: elastic modulus of internal reinforcement

$E_s$: elastic modulus of steel sheet

$E_{SH}$: strain-hardening modulus

$EI_1; EI_2$: flexural rigidity of composite slab (1 for uncracking and 2 for micro-cracking analysis)

$f_{SH}$: stress causing micro-cracking

$F_1, F_2$: constant value in moment-curvature expression (1 for uncracking and 2 for micro-cracking analysis)

$f_1$: the stress intercepts

$G_1$: parameter for second order differential equation

$I_c, I_r, I_s$: moment of inertia of the concrete, the internal reinforcement and steel sheeting, respectively

$I_{cr}$: moment of inertia of concrete uncracked component for micro-cracking

$i$: indicates the number of segment in slab micro-cracking part which should count from 1 to 10

$K_{pr}$: stiffness of shear flow relationship

$L$: length of slab span

$M$: the total applied moment

$M_c$: moment of concrete for uncracking

$M_{c1}$: moment in concrete uncracked component for micro-cracking

$M_{c2}$: moment in concrete micro-cracked component for micro-cracking

$M_r$: moment due to the reinforcement about the centroid of the concrete

$M_s$: moment about the centroid for steel sheet

$M_{shear}$: moment due to accumulated axial force

$N_c, N_r, N_s$: the force in concrete; the force in reinforcement; the force in steel deck

$pl$: magnitude of central applied point load

$Q$: shear flow between the steel and concrete sections

$q$: the accumulated axial force

$s$: relative slip between concrete and steel deck

$V$: shear force

$w$: magnitude of uniformed distributed load (UDL) (unit: kN/m)

$x$: is the horizontal distance along the member from the left hand support.

$y$: depth measured from concrete top surface

$\Delta\bar{y}$: the distance between concrete and steel sheet centroid

$\varepsilon_0$: the strain at the top fibre of the concrete

$\varepsilon_c, \varepsilon_r, \varepsilon_s$: strain in the concrete, the internal reinforcement and steel sheeting, respectively

$\varepsilon_{ci}$: concrete bottom strain with time-dependent effect

$\varepsilon_{ct}$: strain to cause macro-cracking

$\varepsilon_{sh}$: shrinkage strain ($\varepsilon_{sh} = \varepsilon_{sh0} + \chi_{sh} y$)

$\varepsilon_{sh0}$: shrinkage at the top surface of the concrete (negative value input)

$\bar{\varepsilon}_{sh_c}$: average shrinkage strain in the concrete section ($\varepsilon_{sh0} + \chi_{sh} d_c$)

$\varepsilon_{SH}$: strain to cause micro-cracking

$\bar{\varepsilon}_{sh1}$: average shrinkage strain for concrete uncracked component ($\varepsilon_{sh0} + \chi_{sh} d_{c1}$)

$\bar{\varepsilon}_{sh2}$: average shrinkage strain for concrete micro-cracked component ($\varepsilon_{sh0} + \chi_{sh} d_{c2}$)

$\sigma_c, \sigma_r, \sigma_s$: stress in the concrete, the internal reinforcement and steel sheeting, respectively

$\chi$: curvature of concrete/steel deck

$\chi_{sh}$: curvature of shrinkage strain profile

$\frac{ds}{dx}$: relative slip strain

$\left(\frac{ds}{dx}\right)_0$: slip strain at the support

$\frac{d^2s}{dx^2}$: second order differential equation between slip and distance

$\lambda_1$: parameter used in slip-distance expression

## 5.8 Reference


[1] A. Gholamhoseini, I. Gilbert, and M. Bradford, "Calculation of time-dependent deflection of composite concrete slabs: simplified design approach," *Practice Periodical on Structural Design and Construction,* vol. 20, no. 1, p. 04014024, 2015.

[2] R. S. Costa, A. C. C. Lavall, R. G. L. da Silva, H. F. Viana, F. C. Rodrigues, and E. L. Andrade, "New equations to establish the effective moment of inertia of composite slabs with profiled steel sheeting for deflection calculation," *Journal of Building Engineering,* vol. 37, p. 102135, 2021.

[3] D.-H. Son, B.-I. Bae, M.-S. Lee, M.-S. Lee, and C.-S. Choi, "Flexural strength of composite deck slab with macro synthetic fiber reinforced concrete," *Applied Sciences,* vol. 11, no. 4, p. 1662, 2021.

[4] F. P. Ackermann and J. Schnell, "Steel Fibre Reinforced Continuous Composite Slabs," in *Composite Construction in Steel and Concrete VI*, 2011, pp. 125-137.

[5] P. Vainiūnas, J. Valivonis, G. Marčiukaitis, and B. Jonaitis, "Analysis of longitudinal shear behaviour for composite steel and concrete slabs," *Journal of Constructional Steel Research,* vol. 62, no. 12, pp. 1264-1269, 2006.

[6] S. M. Ahmed *et al.*, "Prediction of longitudinal shear resistance of steel-concrete composite slabs," *Engineering Structures,* vol. 193, pp. 295-300, 2019.

[7] M. A. Bradford, "Generic modelling of composite steel–concrete slabs subjected to shrinkage, creep and thermal strains including partial interaction," *Engineering structures,* vol. 32, no. 5, pp. 1459-1465, 2010, doi: 10.1016/j.engstruct.2010.01.024.

[8] M. Bradford, "On the interaction of partial interaction and shrinkage in composite steel-concrete T-beams," *Procedia Engineering,* vol. 14, pp. 396-401, 2011.

[9] R. I. Gilbert, M. A. Bradford, A. Gholamhoseini, and Z. T. Chang, "Effects of shrinkage on the long-term stresses and deformations of composite concrete slabs," *Engineering Structures,* vol. 40, pp. 9-19, 2012, doi: 10.1016/j.engstruct.2012.02.016.

[10] H. Nguyen, H. Mutsuyoshi, and W. Zatar, "Flexural behavior of hybrid composite beams," *Transportation research record,* vol. 2332, no. 1, pp. 53-63, 2013.

[11] J. Lv *et al.*, "A new composite slab using crushed waste tires as fine aggregate in self-compacting lightweight aggregate concrete," *Materials,* vol. 13, no. 11, p. 2551, 2020.

[12] Y. Wu, D. Oehlers, and M. Griffith, "Partial-interaction analysis of composite beam/column members," *Mechanics of Structures and Machines,* 2007.

[13] Q. Gao, Z. Dong, K. Cui, C. Liu, and Y. Liu, "Fatigue performance of profiled steel sheeting–concrete bridge decks subjected to vehicular loads," *Engineering Structures,* vol. 213, p. 110558, 2020.

[14] Y. Zou, X. Zhou, J. Di, and F. Qin, "Partial interaction shear flow forces in simply supported composite steel-concrete beams," *Advanced Steel Construction,* vol. 14, no. 4, pp. 634-650, 2018.

[15] R. I. Gilbert, "Time-dependent Stiffness of Cracked Reinforced and Composite Concrete Slabs," *Procedia Engineering,* vol. 57, no. C, pp. 19-34, 2013, doi: 10.1016/j.proeng.2013.04.006.

[16] A. Gholamhoseini, R. I. Gilbert, M. Bradford, and Z.-T. Chang, "Time-dependent deflection of composite concrete slabs," *ACI Structural Journal,* vol. 111, no. 4, p. 765, 2014.

[17] A. Gholamhoseini, R. Gilbert, M. Bradford, and Z. Chang, "Long-term deformation of composite concrete slabs under sustained loading," in *Proceedings of the From Materials to Structures: Advancement Through Innovation—Proceedings of the 22nd Australasian Conference on the Mechanics of Structures and Materials, ACMSM*, 2013, pp. 67-72.

[18] Q. Wang, J. Yang, Y. Zhang, Y. Fang, and Q. Ren, "Analysis and design of long-term responses of simply-supported steel–concrete composite slabs," *Journal of Building Engineering,* vol. 53, p. 104496, 2022.

[19] A. Sturm, P. Visintin, and D. Oehlers, "Rational design approach for the instantaneous and time-dependent serviceability deflections and crack widths of FRC and UHPFRC continuous and simply supported beams," *Journal of Structural Engineering,* vol. 145, no. 11, p. 04019138, 2019.

## CHAPTER 6 – Concluding Remarks

Steel concrete composite structures show sufficient benefits when applied in construction design. Additionally, ultra-high-performance fibre-reinforced concrete (UHPFRC) is a novel type of concrete which shows superior material property and it is widely utilised in infrastructure and bridge deign. In order to fully investigate the potential for application of UHPFRC with profiled deck as a composite slab, this thesis presents a comprehensive study on evaluating performance of UHPFRC and profiled deck composite slabs. It studied various aspects, starting from the longitudinal bond property to full-scale experimental slab tests. It then proposed numerical solutions to validate the experiment results and finally simplified the process to derive analytical approaches used to predict in-service behaviour of composite slabs. The main concept underlying these studies is to incorporate tested material properties including UHPFRC compressive and tensile strain-stress relationship, the relationship between crack opening and stress as well as strain-stress relationships of profiled deck and reinforcement by applying partial interaction (PI) theory between concrete and steel components in tension stiffening analysis and elemental segmental analysis to propose a generic design for composite slabs with various combination in UHPFRC and profiled deck. A numerical model and analytical solutions are specifically developed to evaluate performance of composite slabs at serviceability limit state taking into account time-dependent effects into analysis.

In the first paper, a new test apparatus was developed to study the local bond behaviour between concrete and profiled deck, the studied objectives included examining bonded length, fibre content, coarse aggregate content and different types of profiled decks. The conclusion drawn from this study is that the concrete strength and inclusion of coarse aggregate made limited impact on the bond performance. However, composite slab containing 2% fibre doubled the longitudinal shear strength and exhibited stronger shear stiffness and toughness compared to composites without fibre. Additionally, when UHPFRC incorporated with dove-tailed profiled deck, it demonstrated a better enhancement in bond behaviour compared to trapezoidal countertype.

In the second paper, experimental tests were conducted to evaluate the overall loading behaviours for simply-supported composite slabs and continuous slabs with varying fibre contents. Both simply-supported and continuous slab tests demonstrated that the member stiffness improved and crack widths were significantly reduced as the fibre content increased in terms of serviceability behaviour. In the case of the simply-supported slab, increasing the fibre content from 0% to 1% lead to an improvement in the ultimate load capacity. However,

with fibre content increasing to 2%, there was a slight enhancement can be observed in loading capacity. In continuous slab tests, moment redistribution showed a positive relationship with all fibre dosages.

In the third paper, a numerical model was developed for composite slab design, taking into account the partial interaction behaviour between concrete and reinforcement in tension stiffening analysis and also between concrete and profile deck in segmental analysis. The numerical model was validated by comparing with previous experimental test results. The simulated results demonstrated good agreement with the tested results in terms of flexural performance, longitudinal slip behaviour and cracking performance at the serviceability limit state. The simulation also highlighted the benefits of incorporating fibre in the composite slab design. It found out that the addition of fibre enhanced the flexural rigidity of the slab resulting in an improved load-deflection response. Furthermore, the inclusion of fibre in composite slabs reduced crack widths, thereby improving the serviceability behaviour of the composite slab.

Finally, analytical solutions were derived and simplified based on the numerical solutions and it aimed to be used for composite slab design guideline at serviceability limit state. These equations finally derived a general expression for estimating curvature value of each segment under central point loading and UDL configurations, respectively. These analytical solutions can be used for UHPFRC composite slabs serviceability design when the concrete is either uncracked or has micro-cracks, the model also has allowance for non-uniform shrinkage strains and partial-interaction behaviour occurred at contact surface.

The analytical methods proposed have been validated by comparing with numerical load-deflection results with and without shrinkage effect under central-point load or UDL, respectively. The results showed that the analytical solutions were identical to the numerical results which indicates this analytical solutions are reliable to be used for composite slab design.

In the analysis, for slab uncracked status, curvature results can determined from equations directly and then determine deflection results while in slab micro-cracked analysis, the analytical solutions requires iteration for end of slip ($s_1$), the curvature and neutral axis guesses for each micro-cracked segments. Therefore, the next step will include simplifying the current analysis and determining a simpler way for evaluating concrete micro-cracked load-deflection results more straightforward by avoiding iterative process. In addition, the future investigation can focus on studying entire floor systems which adding composite beam to slabs.